



N° d'ordre NNT : xxx

**THÈSE DE DOCTORAT DE L'UNIVERSITÉ DE LYON**  
opérée au sein de  
**l'Université Claude Bernard Lyon 1**

**École Doctorale ED52**  
**Physique et Astrophysique de Lyon**

**Spécialité de doctorat :**  
**Discipline : Physique médicale**

Soutenue publiquement à huis clos le jj/12/2018, par :  
**Mattia Fontana**

---

**Tests and characterization of gamma cameras for ion beam therapy monitoring and nuclear medicine applications**

---

Devant le jury composé de :

Nom Prénom, grade/qualité, établissement/entreprise	Président(e)
Thirolf Peter, grade/qualité, établissement/entreprise	Rapporteur
Llosá Gabriela, grade/qualité, établissement/entreprise	Rapporteure
Morel Christian, grade/qualité, établissement/entreprise	Examinateur
Rafecas Magdalena, grade/qualité, établissement/entreprise	Examinatrice
Testa Étienne, grade/qualité, établissement/entreprise	Directeur de thèse
Létang Jean Michel, grade/qualité, établissement/entreprise	Co-directeur de thèse
Dauvergne Denis, grade/qualité, établissement/entreprise	Invité

# ***Tests and characterization of gamma cameras for ion beam therapy monitoring and nuclear medicine applications***

PhD Candidate

---

MATTIA FONTANA

Thesis directors

---

ÉTIENNE TESTA and JEAN MICHEL LÉTANG

Université Claude Bernard  
Lyon 1  
Physics department  
Doctoral school ED52:  
Physics and Astrophysics



# Abstract

Ion beam therapy is a promising technique in cancer treatment because of the ion defined range and favorable dose delivery features. Strict and precise treatment planning and monitoring are now key points for the method developments and full exploitation. In particular, with the aim of optimizing the ion treatment effectiveness, the ion range monitoring is mandatory: different solutions have been explored, but an online treatment check is still a challenge. The ion beam treatment monitoring is mainly performed by means of secondary charged or neutral particles. In this context, the detection of the prompt-gammas (PG) emitted during treatments has proven its potential in the ion range control in real time. Since the first evidence of the existing correlation between the emitted gamma profile fall-off and the Bragg peak position, several groups are involved in research activities in order to develop and optimize instruments and methods with the aim of improving this monitoring technique. Among the others, collimated and Compton cameras are being studied and optimized for this application. The same detectors can also be employed in nuclear medicine for the detection of the radioactive elements decay products.

A collaboration of 5 institutions in France is involved in the parallel development of two composite detectors for ion beam monitoring and nuclear medicine application, and this thesis is carried out within this collaboration with the detectors clinical trial as final aim.

The project started a few years ago and is now at the final stage. The two cameras have been designed according to simulation studies, and the different components are now under tests. The collimated camera is composed by a multi-slit tungsten mechanical collimator, set in front of an absorber composed of 96 BGO blocks, for a total size of 380x380x30 mm<sup>3</sup>; each block presents a streaked surface with a 8x8 pixel matrix and the signal is read-out by 4 photomultipliers. A ~3 ns time resolution can be achieved for the prompt gamma detection. The same absorber is part of the Compton camera, in addition to a scatterer section composed by 7 Double-Sided Silicon Detectors 96x96x2 mm<sup>3</sup> each. With the collimated camera, the parallel emitted photons are selected by the collimator and a mono-dimensional emission profile can be reconstructed. The Compton camera has a more efficient detection technique, being absent a mechanical collimation system, and could potentially lead to 3D information thanks to the reconstruction of the Compton cone. In both cases an additional detector component is needed to temporally tag the incoming beam ions and help rejecting the relevant background (mostly due to neutrons) which strongly affects the prompt gamma yield. A scintillating fiber tagging hodoscope is then under development: it is composed by 128x2 perpendicular scintillating fibers, read-out from both sides by 8 64-channel silicon photomultipliers by Hamamatsu. The thesis work consists in the critical evaluation, characterization and tuning of the different components, together with the associated electronics, and of the complete detectors on beam. In parallel, simulation studies can improve the detection technique and optimize the detector structure, as well as pave the way for further applications.



# Contents

<b>Prologue</b>	<b>1</b>
<b>1 Introduction</b>	<b>3</b>
1.1 Ion beam therapy . . . . .	3
1.1.1 Physics . . . . .	3
1.1.2 Advantages and drawbacks . . . . .	3
1.1.3 Range verification . . . . .	3
1.1.4 Secondary radiations . . . . .	3
1.1.5 Prompt-gammas: physics and features . . . . .	3
1.1.6 State of the art of range verification . . . . .	3
1.2 Nuclear medicine . . . . .	3
1.2.1 PET and SPECT . . . . .	3
1.2.2 Comparison, advantages and drawbacks . . . . .	3
1.2.3 State of the art of SPECT . . . . .	3
1.3 Photons . . . . .	3
1.3.1 Photon interactions in matter . . . . .	3
1.3.2 Photon detection . . . . .	4
<b>2 Gamma cameras</b>	<b>5</b>
2.1 Working principle . . . . .	6
2.2 Applications in medicine . . . . .	6
2.2.1 Ion beam therapy . . . . .	6
2.2.2 Nuclear medicine . . . . .	6
2.3 State of the art . . . . .	6
<b>3 CLaRyS prototypes</b>	<b>7</b>
3.1 CLaRyS gamma camera components . . . . .	8
3.1.1 Scatterer . . . . .	9
3.1.1.1 Scatterer Front-End card . . . . .	11
3.1.1.2 Scatterer thermal regulated box . . . . .	12
3.1.2 Collimator . . . . .	12
3.1.3 Absorber . . . . .	13
3.1.3.1 Absorber Front-End and read-out cards . . . . .	16
3.1.3.2 Absorber mechanical support . . . . .	16
3.1.4 Beam tagging hodoscope . . . . .	17
3.1.4.1 Hodoscope Front-End card . . . . .	20
3.1.4.2 Hodoscope mechanical support . . . . .	20
3.1.4.3 Small hodoscope prototypes . . . . .	21
3.1.5 Camera electronics and acquisition system . . . . .	22
3.1.6 Camera slow control, acquisition and monitoring software . . . . .	23
3.1.7 Camera integration and mechanical support . . . . .	23
3.2 Camera component characterization and development status . . . . .	23
3.2.1 Hodoscope Photo-Multipliers (PMs) characterization . . . . .	23
3.2.2 Hodoscope fiber test with electron source . . . . .	26

3.2.3	Absorber Bismuth Germanium Oxide - Bi <sub>12</sub> GeO <sub>20</sub> (BGO) blocks characterization . . . . .	26
3.2.3.1	Space and energy calibration and characterization . . . . .	28
3.2.3.2	Pixel identification and energy calibration algorithm . . . . .	29
3.2.3.3	Time response characterization method . . . . .	29
3.2.3.4	Results: PM gain equalization . . . . .	30
3.2.3.5	Pixel identification . . . . .	32
3.2.3.6	Pixel energy calibration . . . . .	33
3.2.3.7	Time characterization . . . . .	36
3.2.3.8	Results for the 30 blocks . . . . .	36
3.3	Next steps and perspectives . . . . .	40
<b>4</b>	<b>Compton camera application for ion beam therapy monitoring</b>	<b>41</b>
<b>5</b>	<b>Compton camera application in nuclear medicine</b>	<b>43</b>
5.1	Material and methods . . . . .	45
5.1.1	Radioactive sources . . . . .	45
5.1.2	Compton camera simulation and data analysis . . . . .	45
5.1.2.1	Simulation settings . . . . .	45
5.1.2.2	Data collection and analysis . . . . .	47
5.1.2.3	Compton camera study for SPECT application . . . . .	48
5.1.3	Anger camera simulation and data analysis . . . . .	49
5.1.3.1	Simulation settings . . . . .	49
5.1.3.2	Data analysis . . . . .	50
5.1.4	Figures of merit for the comparison study . . . . .	53
5.2	Results: Compton camera study for SPECT application . . . . .	55
5.2.1	Influence of Compton camera scatterer detector energy resolution . . . . .	55
5.2.2	Compton camera coincidence study . . . . .	56
5.3	Results: Benchmark of Compton camera and Anger camera performance . . . . .	57
5.4	Discussion . . . . .	59
<b>6</b>	<b>Beam tests</b>	<b>63</b>
6.1	Hodoscope: december 2017 . . . . .	64
6.2	Hodoscope: may 2018 . . . . .	64
6.3	Collimated camera: august 2018 . . . . .	64
6.4	Collimated camera: september 2018 . . . . .	64
<b>7</b>	<b>Conclusions and discussion</b>	<b>65</b>
<b>A</b>	<b>Compton camera data format</b>	<b>67</b>
A.1	Introduction . . . . .	67
A.2	General features . . . . .	67
A.2.1	Common information . . . . .	67
A.2.1.1	Front End number . . . . .	67
A.2.1.2	Pre-trigger and trigger . . . . .	69
A.2.1.3	Mode number . . . . .	69
A.3	Physical data format . . . . .	71
A.3.1	Scatterer detector data format . . . . .	71
A.3.2	Absorber detector data format . . . . .	71
A.3.3	Beam hodoscope data format . . . . .	74

---

A.4 Slow control, trigger and monitoring data format . . . . .	74
A.4.1 Communication architecture . . . . .	74
A.4.2 Transport protocol and processor packets . . . . .	75
A.4.2.1 Definitions . . . . .	75
A.4.2.2 Data encoding . . . . .	76
A.4.2.3 Packets format . . . . .	76
A.4.2.4 Possible control symbols . . . . .	77
A.4.3 Transport layer . . . . .	77
A.4.3.1 Control packet . . . . .	77
A.4.3.2 Configuration packets . . . . .	78
A.4.3.3 Monitoring process (Front End cards → μ-TCA) . . . . .	79
A.4.3.4 Special command process (μ-TCA → Front End cards) . . . . .	81
A.4.4 Data packets (Front End card → μ-TCA) . . . . .	81
A.5 UDP packets format . . . . .	83
A.6 Data throughput expected in clinical conditions . . . . .	84
A.6.1 Clinical intensities . . . . .	84
A.6.1.1 Review: detector and target sizes . . . . .	84
A.6.2 Coincidence rate . . . . .	85
A.6.3 Data flow (Front End cards → μ-TCA) . . . . .	85
A.6.4 Acquisition data flow (μ-TCA → Acquisition PC) . . . . .	86
A.6.5 Conclusions . . . . .	87
<b>B Electronics specifications</b>	<b>89</b>
<b>Acronyms</b>	<b>93</b>
<b>Bibliography</b>	<b>95</b>



# List of Figures

3.1	Schematic view of the two CLaRyS gamma camera prototypes: the multi-collimated camera (top) and the Compton camera (bottom). . . . .	9
3.2	.....	11
3.3	Scheme of the scatterer stack thermal box and internal mechanical support. . . . .	13
3.4	.....	13
3.5	Absorber modules. . . . .	15
3.6	.....	16
3.7	Absorber front view with the BGO block lines arranged in the mechanical support (left). Scheme of the BGO absorber with its mechanical support (right). . . . .	17
3.8	Contrôle en Ligne de lâhadronthérapie par Rayonnements Secondaires - Online monitoring of ion beam therapy through secondary particles (CLaRyS) scintillating fiber hodoscope on its 2-dimensional moving table. . . . .	18
3.9	Details of the CLaRyS scintillating fiber hodoscope setup. . . . .	19
3.10	Hodoscope Front-End card developed at Institut de Physique Nucléaire de Lyon (IPNL). . . . .	20
3.11	Hodoscope small prototypes. . . . .	21
3.12	.....	22
3.13	Schematic view of the Compton camera acquisition system. For the multi-collimated camera, the trigger and pre-trigger signals are the same. . . . .	22
3.14	.....	23
3.15	.....	25
3.16	.....	26
3.17	.....	26
3.18	.....	28
3.19	PM signal amplitude spectra before (a) and after (b) the PM gain equalization. . . . .	31
3.20	1D integrated position distribution on the two transverse dimensions before (a) and after (b) the PM gain equalization. Blue curves: horizontal dimension. Green curves: vertical dimension. . . . .	31
3.21	Block energy spectrum before (a) and after (b) the PM gain equalization. . . . .	32
3.22	2D reconstructed position map before (a) and after (b) the PM gain equalization. . . . .	32
3.23	1D integrated position distributions on the two transverse dimensions with the retrieved position of the pseudo-pixel average center (a). Reconstructed 2D map with the identified pseudo-pixels positions and surfaces. . . . .	33
3.24	Auxiliary position map used for the assignment of the reconstructed events to a single pixel. The highlighted points represent the average distances between neighboring pixels on their separation borders. . . . .	34
3.25	Logic for the event assignment to a single pixel (left) and 2D map of the resulting interaction assignment (right): each event is colored according to the chosen pseudo-pixel. . . . .	35
3.26	Single pseudo-pixels (a) and whole block (b) energy spectra before (left) and after (right) the calibration process. The whole block spectra are reported in logarithmic scale. Three non calibrated spectra of pixels in reference positions (border, mid-center and center area) on the block are also reported with the non calibrated spectrum. . . . .	37

3.27	Relative number of entries for each pseudo-pixel as a function of the pixel relative position, represented by the row and column numbers (0 to 8 from left to right and bottom to top of the block surface). Figure (a) shows the entries in a selected energy window around 511 keV, figure (b) in an energy window around 1275 keV. All the entries are normalized to the maximum collected number of entries, corresponding to 511 keV events in the central section of the block.	38
3.28	Distribution of arrival time differences between reference scintillator and BGO block.	38
5.1	Sketch of the simulated geometry of the two systems: Anger camera (left) and Compton camera (right), in 3 dimensions (top line) and side projection (bottom line).	46
5.2	Radial event distribution normalized by the circular surface corresponding to each bin for 4 representative source energies, with the linear fit performed for background rejection. The total number of simulated primaries for each data set is $10^8$ .	52
5.3	Comparison between expected entries in the central collimator hole (blue dashed curve) calculated according to pure geometrical factors and detector interaction cross section and simulated detected entries after background rejection (red solid curve) with null spatial resolution (ideal detector) to avoid resolution effects and lower energy threshold set to 80 keV.	53
5.4	Normalized radial distribution with background rejection (red solid lines) compared to normalized radial distribution for infinite density collimator (blue dashed lines).	54
5.5	Reconstructed radial distribution standard deviation as a function of the source energy. Two energy resolution values are set to the silicon detectors ( $\sigma_E = 2\text{ keV}$ - red dots solid line - and $\sigma_E = 4\text{ keV}$ - blue dots dashed line), the Doppler broadening effect has been removed (green horizontal triangles dashed line) and the scatterer material has been changed with CdTe solid state detectors (black vertical triangles dashed line), for a fixed energy resolution of $\sigma_E = 2\text{ keV}$ .	55
5.6	(a): number of true (green) and random (red) coincidences as a function of the source activity in the range 1-500 MBq, for the reference energy of 555 keV. (b): Percentage of random coincidences as a function of the source energy, with a fixed source activity of 200 MBq. Compton camera parameters: time resolution FWHM of 20 ns for silicon detectors, 3 ns for BGO and a coincidence window of 40 ns. The source branching ratio has been set to 100% for all sources for simplicity in the comparison of results.	56
5.7	Overlap of the normalized radial distributions for 4 selected source energies.	57
5.8	Detection efficiency as a function of the source energy. Source activity = 200 MBq, Compton camera silicon detector $\sigma_E = 2\text{ keV}$ .	58
5.9	Standard deviation of the radial event distributions as a function of the source energy. Source activity = 200 MBq, Compton camera silicon detector $\sigma_E = 2\text{ keV}$ .	58
5.10	Signal-to-background ratio as a function of the source energy. Source activity = 200 MBq, Compton camera silicon detector $\sigma_E = 2\text{ keV}$ .	59
A.1	Data acquisition logic: pre-trigger and trigger generation and readout process.	70
A.2	Scatterer detector data format.	72
A.3	Absorber detector data format.	73
A.4	Beam hodoscope data format.	74

A.5 Architecture of communication between DAQ cards and $\mu$ -TCA. . . . .	75
---	----



# List of Tables

3.1 Comparison of the results obtained with the two pixel-assignment methods . . . . .	35
3.2 Calibration and characterization results for 10 tested BGO blocks. . . . .	39
5.1 Radioactive sources used in the comparison study. Decay mode list: EC for electron capture, $\beta^-$ for electron emission, $\beta^+$ for positron emission, IT for isomeric transition. Half-life expressed in days (d), hours (h) or minutes (m). Data extracted using the National Nuclear Data Center On-Line Data Service from the Evaluated Nuclear Structure Data File database, file revised as of (2017-05-17) ( <a href="#">Bhat 1992</a> ). . . . .	46
A.1 Front End number associated to each Front End card. . . . .	68
A.2 Packet with an even byte number cargo. . . . .	76
A.3 Packet with an odd byte number cargo. . . . .	76
A.4 Control symbol definition. . . . .	77
A.5 Control symbol definition. . . . .	78
A.6 Definition of the acknowledgement packet. . . . .	78
A.7 Writing register packet. . . . .	79
A.8 Reading register packet. . . . .	79
A.9 Two special registers( $\mu$ -TCA $\rightarrow$ Front End cards) . . . . .	80
A.10 Measurement packet (Front End cards $\rightarrow$ $\mu$ -TCA) . . . . .	80
A.11 Monitoring packet. . . . .	80
A.12 Monitoring messages. . . . .	81
A.13 Special command packets . . . . .	81
A.14 Special commands examples . . . . .	82
A.15 Control symbol for pre-trigger, trigger and physical data. . . . .	82
A.16 Pre-trigger packet . . . . .	83
A.17 Trigger packet . . . . .	83
A.18 Physical data packet . . . . .	83
A.19 Coincidence and single rate as a function of the beam intensity. The BGO single rate corresponds to the pre-trigger rate. . . . .	85
A.20 Data flux between FE cards and $\mu$ -TCA. . . . .	86
A.21 Data flow between $\mu$ -TCA and acquisition PC. . . . .	86



# Prologue



# 1

## Introduction

### 1.1 Ion beam therapy

#### 1.1.1 Physics

#### 1.1.2 Advantages and drawbacks

#### 1.1.3 Range verification

#### 1.1.4 Secondary radiations

#### 1.1.5 Prompt-gammas: physics and features

#### 1.1.6 State of the art of range verification

### 1.2 Nuclear medicine

#### 1.2.1 PET and SPECT

#### 1.2.2 Comparison, advantages and drawbacks

#### 1.2.3 State of the art of SPECT

### 1.3 Photons

#### 1.3.1 Photon interactions in matter

$$h\nu' = \frac{h\nu}{1 + \frac{h\nu}{m_0c^2}(1 - \cos(\theta))} \quad (1.1)$$

### **1.3.2 Photon detection**

# 2

## Gamma cameras

### Contents

<b>2.1 Working principle . . . . .</b>	<b>6</b>
<b>2.2 Applications in medicine . . . . .</b>	<b>6</b>
2.2.1 Ion beam therapy . . . . .	6
2.2.2 Nuclear medicine . . . . .	6
<b>2.3 State of the art . . . . .</b>	<b>6</b>

**2.1 Working principle**

**2.2 Applications in medicine**

**2.2.1 Ion beam therapy**

**2.2.2 Nuclear medicine**

**2.3 State of the art**

# 3

## CLaRyS prototypes

### Contents

<b>3.1 CLaRyS gamma camera components . . . . .</b>	<b>8</b>
3.1.1 Scatterer . . . . .	9
3.1.2 Collimator . . . . .	12
3.1.3 Absorber . . . . .	13
3.1.4 Beam tagging hodoscope . . . . .	17
3.1.5 Camera electronics and acquisition system . . . . .	22
3.1.6 Camera slow control, acquisition and monitoring software . . . . .	23
3.1.7 Camera integration and mechanical support . . . . .	23
<b>3.2 Camera component characterization and development status . . .</b>	<b>23</b>
3.2.1 Hodoscope PMs characterization . . . . .	23
3.2.2 Hodoscope fiber test with electron source . . . . .	26
3.2.3 Absorber BGO blocks characterization . . . . .	26
<b>3.3 Next steps and perspectives . . . . .</b>	<b>40</b>

Following the highlighted limits of ion beam therapy (see chapter 1), a collaboration of five French research institutions was established in 2008 (??) with the aim of exploring different experimental solutions for the ion range online monitoring. The research group originally involved the “Institut de Physique Nucléaire de Lyon (IPNL)”, the “Centre de Physique des Particules de Marseille (CPPM)”, the “Laboratoire de Physique Subatomique et Corpusculaire (LPSC)” in Grenoble, the “Laboratoire de Physique de Clermont (LPC)” and the “Centre de Recherche en Acquisition et Traitement de l’Image pour la Santé (CREATIS)” in Lyon. The collaboration focuses on the investigation of methods and detection solution for the online monitoring of ion beam range during ion beam therapy treatment, and is so called Contrôle en Ligne de l’hadronthérapie par Rayonnements Secondaires - Online monitoring of ion beam therapy through secondary particles (CLaRyS).

The main goal of the created collaboration is the parallel development of three gamma detection systems to be employed for ion range online monitoring purpose in the ion beam therapy field: a Positron Emission Tomography (PET) detector, a multi-collimated gamma camera and a Compton camera.

The design and development of the PET system is mainly managed by the LPC group, which left the collaboration in 2017, and the this detection system is not treated in this thesis work. In this chapter the two gamma cameras (multi-collimated and Compton) prototypes are described in details, and the present status of the instrumental development is presented. In the following, an entire chapter (chapter 6) is dedicated to the tests of the detectors performed on ion beams.

## 3.1 CLaRyS gamma camera components

The two gamma cameras under development by the CLaRyS collaboration are devoted to the detection of prompt-gamma rays emitted during ion beam treatments (see section ??). The design of the two cameras has been optimized by different Monte Carlo simulation studies for what concerns both the detector components and the geometrical setup.

As already mentioned, a Compton camera is usually composed of two detector sections, a scatterer and an absorber: the CLaRyS prototype respects the standard design. In the scatterer, described in section 3.1.1, the prompt-gamma incoming ray is deflected by Compton interaction and the interaction position and energy deposited are stored. The scattered photon reaches then the absorber section, where its energy is ideally totally deposited and stored, again with the interaction position. This configuration is used to provide what is usually defined as “electronic collimation”, but a mechanical collimation is still an option for photon detection and localization. The scatterer section can be replaced by a mechanical collimator, described in section 3.1.2, which selects the parallel incoming photons then absorbed by the same absorber detector (a geometrical setup adaptation is possible to optimize the detection performance and will be discussed in the following). The mechanically collimated system is called multi-collimated camera, due to the collimator multi-slit structure.

As underlined in section ??, the prompt-gamma measurements are affected by several sources of background: in particular, the signals detected by the two cameras can come from secondary particles other than prompt-gammas, like photons from positron annihilation, neutrons and protons (for beam of ions heavier than protons). One of the possible solution for background rejection is the use of Time-Of-Flight (TOF) information (see section ??), requiring a further detection section dedicated to the beam tagging. A beam tagging hodoscope is being developed in parallel and can be coupled to both the gamma cameras for TOF measurements; its

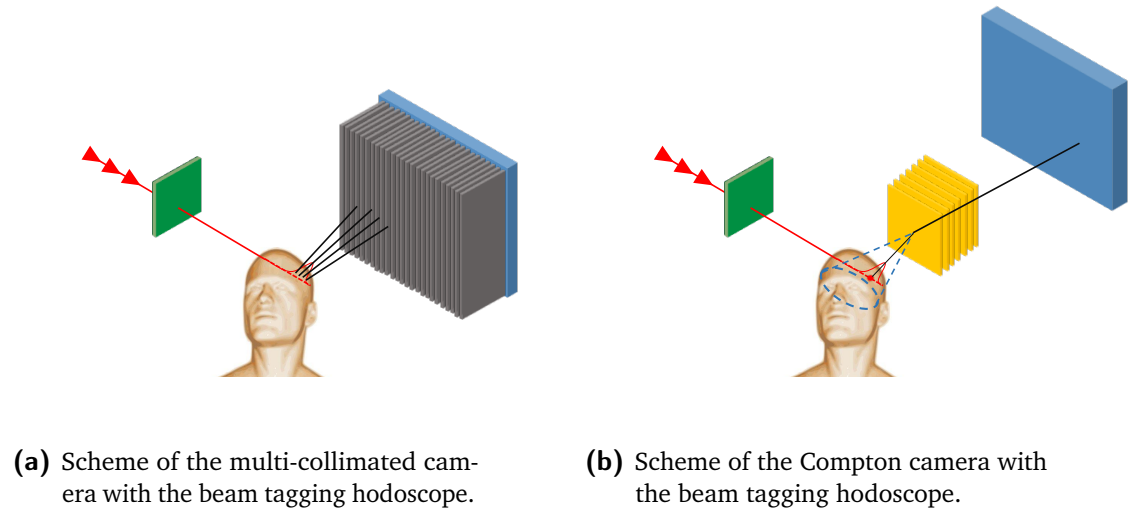


**Figure 3.1:** Schematic view of the two CLaRyS gamma camera prototypes: the multi-collimated camera (top) and the Compton camera (bottom).

description is presented in section 3.1.4.

A schematic view of the two prototypes is given in figure 3.1.

### 3.1.1 Scatterer

The scatterer stack is one of the components of the Compton camera prototype. Dedicated to the photon Compton scattering, its design has been studied to fulfill the camera requirements.

The Compton events reconstruction strongly relies on the measurement of the energy deposited by the photon in its Compton interaction, mandatory to properly calculate the Compton scattering angle, which is then the aperture of the resulting Compton cone. The camera accuracy is then strictly dependent on the scatterer energy resolution. At the same time, the camera efficiency is dominated by the balance between Compton interaction and photoelectric absorption probability in the scatterer detector.

Given the need of at least two interactions for a proper event reconstruction (a Compton scattering in the scatterer section and an ideally complete absorption in the absorber section, described in 3.1.3), the material choice and the geometrical configuration play a fundamental role in the camera operation. The setup must be tuned in order to define the better trade-off between Compton and photoelectric interaction probability and to optimize, as mentioned, the detector energy resolution.

Given the fact that the Compton interaction probability linearly increases with the material atomic number ( $Z$ ), while the photoelectric absorption depends on  $Z^n$  with  $n$  varying between 4 and 5 according to the photon primary energy (Knoll 2000), it is clear that a low  $Z$  material is preferred. Considering now the detector energy resolution, it must be noticed that the main parameter affecting the deposited energy detection is the so called “Doppler spread”. The Compton angle reconstruction formula in equation 1.1 neglects the initial recoil electron state, which is considered free or unbound. The Compton energy transfer continuum results

affected by the binding energy of the electron, with a relatively increasing effects for decreasing incident photon energy. This effect adds uncertainty on the reconstructed deposited energy, and so in the Compton angle calculation. Given its direct dependence on the recoil electron binding energy, the “Doppler spread” is reduced for low Z materials. Following the described theoretical considerations, silicon detectors are the most coherent choice. This choice has been verified in simulation, where a silicon scatterer has been compared to competitor materials; the result are included in the Monte Carlo study presented in chapter 5.

Dedicated Monte Carlo simulation studies have been performed in order to define the most suitable geometrical configuration for the Compton camera, including the scatterer stack ([Richard 2012](#)). As a trade-off between detection efficiency and total cost, 10 layers were included in the original scatterer design. Concerning the layer size, about  $10 \times 10 \text{ cm}^2$  of active area in the transverse plane have been identified as the most convenient choice, also considering the absorber size (see section 3.1.3) and the distances between the detection sections required by the TOF measurements and imposed by the detector rate acceptance in clinical conditions (see appendix A). Moving to the layer thickness, its choice is governed by the definition of the camera operation. The CLaRyS Compton camera does not aim to track the Compton recoil electron, which must be then absorbed inside the same scatterer layer where the Compton interaction took place. This requirement is necessary to well reconstruct the Compton interaction angle, which needs the whole transferred energy as parameter; in addition to this, a recoil electron escaping the involved detection layer can interact in a different layer causing false coincidences which affect the camera efficiency and imaging accuracy. In order to minimize the recoil electron escape probability, relatively thick detectors are needed.

The technological choice of the collaboration was oriented to silicon Double-sided Silicon Strip Detectors (DSSDs), provided by the Norwegian company SINTEF. A schematic view of the detector principle is given in figure 3.2a. The silicon crystal is doped with negative (n) and positive (p) charge carriers on the two opposite sides, creating diodes which are then reverse biased. A polarization voltage is applied to the two opposite sides of the crystal, and a depletion region with no free charges is created. A ionizing particle interacting in the depletion region generates electron-hole pairs in number proportional to the deposited energy. The generated charges drift towards anode (electrons) and cathode (holes) and are converted into electrical signals. The read-out is ensured by the implanted strips, which transfer the charges outside the detection region.

Each layer has an active volume of  $96 \times 96 \times 2 \text{ mm}^3$ , segmented with 64 strips per detection plane. The strip pitch is 1.41 mm, for a strip width of 1.31 mm. The applied polarization voltage is nominally -750 V, and it is uniformly shared on the whole surface to obtain a homogeneous depletion region. A guard ring, composed of 23 strips surrounding the read-out ones on the p side, ensures the desired voltage gradient. The more peripheral strip of the guard ring is connected to the high voltage, while the n side has a single strip for the guard ring, connected to the ground. The p and n read-out strips are then connected to the FE electronics via bonding cables.

The FE electronics card has been developed by the IPNL electronics group and is described in details in section 3.1.1.1. The silicon detector is directly plugged on the card, and the mechanical support for the scatterer stack has been studied according to the card size, as shown in figure 3.2b.

Among the 10 received DSSDs, only 7 fulfilled the requirements imposed by the Compton camera application, mainly in terms of noise level (leakage current); 3 layer have been

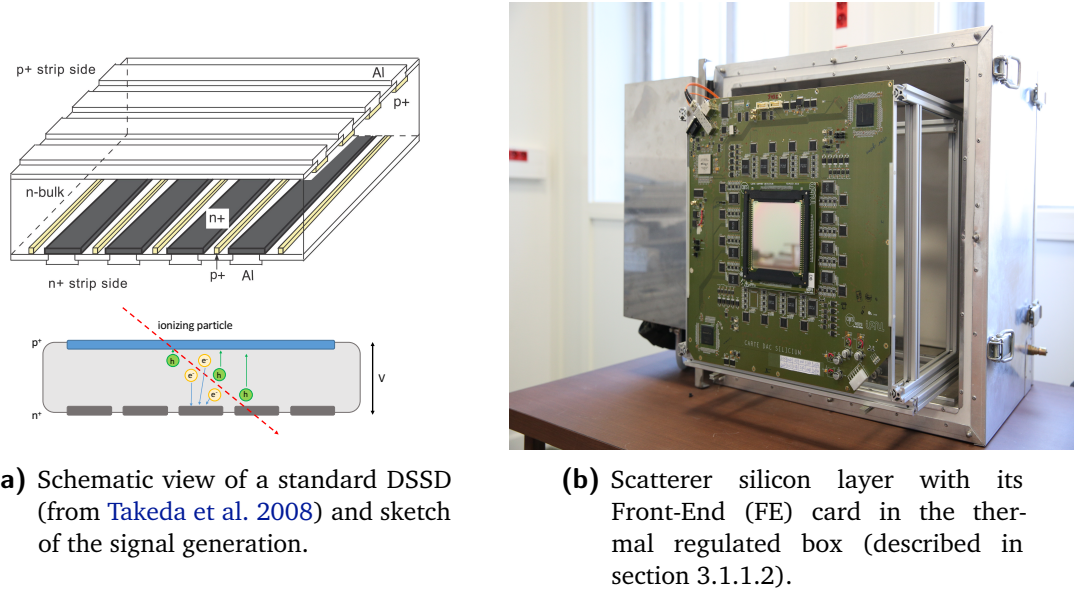


Figure 3.2

rejected, so that the final prototype scatterer is composed of 7 silicon planes. The 7 selected layers have been characterized with a temporary acquisition system in terms of leakage current at different temperatures. The results of these measurements can be found in Ley 2015. The measurements allowed to verify the producer specifications in terms of polarization voltage to be applied for a complete detector depletion, as well as to identify the noisy strips and create a complete characterization database. In addition to this, they highlighted the need to cool the detectors down with respect to the room temperature ( $25^{\circ}\text{C}$ ) in order to reduce the leakage current to acceptable levels, and so reducing the total noise level, affecting the detector performance. In order to accomplish the cooling task and respect, at the same time, the clinical restrictions, a thermal regulated box based on cold air pump has been designed and produced. It operates as the scatterer stack mechanical support, and it is described in section 3.1.1.2.

### 3.1.1.1 Scatterer Front-End card

As mentioned in the previous paragraph, the main requirement for the scatterer detector modules is a very good energy resolution. The desired working performance can be quantified as follows:

- 1 keV Full Width at Half Maximum (FWHM) energy resolution;
- 1.41 mm spatial resolution (corresponding to the strip pitch);
- 15 ns FWHM time resolution.

The scatterer FE card has been developed by the IPNL electronics group in order to achieve these performance. It is composed of two well separated sections, analog and digital, which

must be kept separated in the card layout in order to minimize the contribution of the digital noise on the treatment of the analog signals. The required energy resolution corresponds to an Equivalent Noise Charge (ENC) of 118 electrons Root Mean Square (RMS); a dedicated, custom Application-Specific Integrated Circuit (ASIC) represents the core of the FE card and has been developed to obtain this result ([Dahoumane et al. 2014](#)).

#### 3.1.1.2 Scatterer thermal regulated box

The results of the leakage current tests performed on the silicon detectors showed the need of cooling the detector down to achieve the required performance in terms of noise, which affects the spatial, time and energy resolutions. The leakage current has been studied in temperature cycles in the range -40 - +40 °C, and an overall consistent behavior has been observed both on N and P strips of the detector. The leakage current slightly increases in the range -40 - 0 °C, with values in the range 0 - 8 nA for the analyzed strips, and then drastically increases beyond 0 °C, with peaks of more than 80 nA at +40 °C. The complete description of the performed measurements and the detailed results can be found in [Ley 2015](#).

A cooling system is needed for the silicon detectors operations: it must be able to keep the temperature constant and below, at least, 0 °C, preferably around -20 °C where the leakage current is more stable in case of small temperature variations. The clinical environment limitations must be considered to design such a cooling system (portability, gas, noise level), as well as the material budget and the mechanical integration with the other camera components.

The implemented solution consists in the thermal regulated box shown in figure 3.2b, together with one of the silicon layers. The size of the box is 490×490×300 mm<sup>3</sup>, and the structure is composed of 2 mm of aluminum and three insulation layers of 10 mm of silica aerogel Spaceloft® ([AspenAerogels 2011](#)), for an equivalent thickness of 2 mm of silicon (0.7% of interaction probability for 1 MeV photons). The cooling is performed via an electric air pump, which is able to keep the temperature inside the box at -20 °C with a 400 W haet evacuation power. The heat power produced by the 7 silicon FE cards in operation must be verified, but the estimate confirms the effectiveness of the thermal box nominal performance. Once card and detector will be fully operational, a test will be performed to check the temperature stability inside the box.

The FE cards and the silicon layers are fixed inside the box via a mechanical support designed and produced by the IPNL mechanics group. The support, which ensures a millimeter position accuracy, is fixed on metal rails which allow to easily handle each detector layer. A scheme of the thermal box and the internal support is shown in figure 3.3.

#### 3.1.2 Collimator

The multi-collimated camera is equipped with a multi-slit collimator, with tungsten slabs. Its design has been extensively studied in Monte Carlo simulations ([Pinto et al. 2014](#)), and it can be easily adapted to different geometrical configurations of the absorber detector and to various monitoring requirements. In particular, the distance between neighboring slabs can be modified, as well as the number of total slabs, in order to find the best trade-off between detection efficiency and spatial resolution; this depends on the distance patient-collimator, on the required extension of the field of view and on the desired monitoring time. Two identical

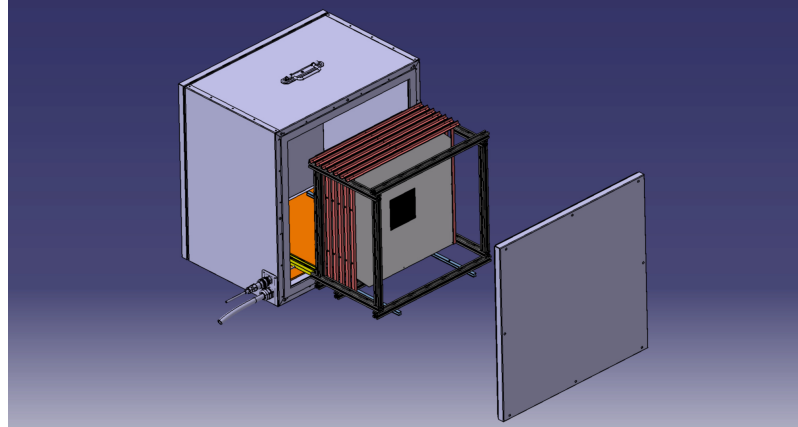
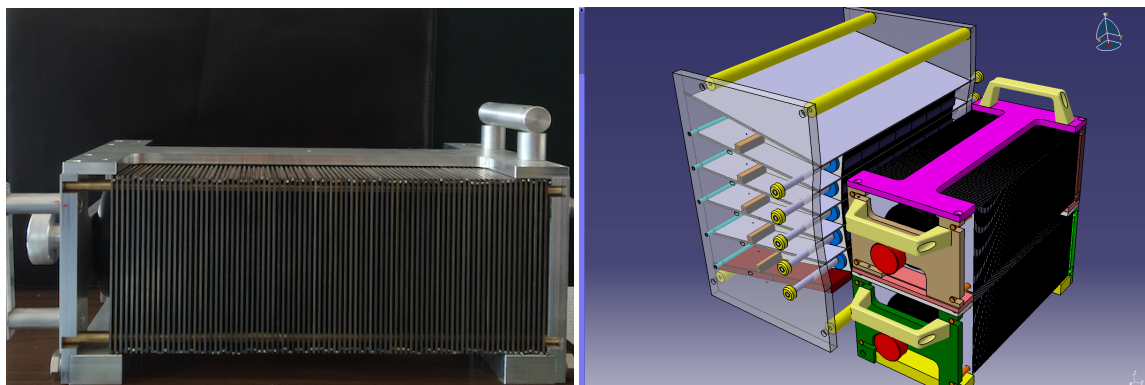


**Figure 3.3:** Scheme of the scatterer stack thermal box and internal mechanical support.



**(a)** Picture of the multi-slit tungsten collimator.

**(b)** Example of multi-collimated camera configuration: the two tungsten multi-slit collimators are placed in front of a  $6 \times 5$  Bismuth Germanium Oxide -  $\text{Bi}_{12}\text{GeO}_{20}$  (BGO) block absorber setup in its mechanical support (see section 3.1.3)

**Figure 3.4**

collimators of  $30 \times 14 \times 17 \text{ cm}^3$  have been produced, in order to be able to set several absorber configurations in the transverse direction (extended version along the beam axis or in the perpendicular direction). In figure 3.4a a picture of the tungsten collimator is presented, while in figure 3.4b we show a schematic view of a possible multi-collimated camera configuration.

### 3.1.3 Absorber

The Compton and multi-collimated camera absorber was initially conceived as a very large surface plane composed of 96 BGO blocks recovered from a dismantled PET system HR+ by SIEMENS, documented in (Adam et al. 1997; Brix et al. 1997).

BGO is one of the most used scintillators for gamma detection applications, thanks to a good energy resolution and a optimal gamma detection efficiency. Moreover, the absence of

internal radioactivity which characterizes other scintillator materials employed in the same field (i.e. Lutetium-Yttrium OxyorthoSilicate -  $\text{Lu}_{2(1-x)}\text{Y}_{2x}\text{SiO}_5$  (LYSO), ), makes it suitable for low noise detectors, required by a Compton camera to reduce the amount of random coincidences, one of the main sources of background for the application in ion beam therapy monitoring ([Ortega et al. 2015](#)). As highlighted in ([Hueso-González et al. 2015](#)), LYSO and show overall better performances with respect to BGO for what concerns energy, time and spatial resolution, due to an about 4 times higher light yield, but the gap is reduced for the detection of gamma rays in the prompt-gamma energy range (especially beyond 1 MeV). The limited cost of BGO with respect to and the comparable performances in the prompt-gamma energy range make it an optimal solution for prompt-gamma camera prototypes.

Each BGO block has a surface of  $3.5 \times 3.8 \text{ cm}^2$ , with a thickness of 3.0 cm. The mono-block BGO crystal is streaked in a  $8 \times 8$  pseudo-pixel matrix; a reflecting material is inserted between the pseudo-pixels to improve the light collection and optimize the spatial information accuracy via pixel separation. The read-out is achieved via four Photo-Multiplier (PM) tubes per block, composing a quartet, coupled to the block back surface. Thanks to the internal streaked structure of the block, the scintillation light is shared on the four PMs depending on the pseudo-pixel where the interaction takes place (in case of multiple interactions more than 1 pseudo-pixel can be involved). The reconstruction of the position of interaction is done via Anger logic, i.e. with a center of gravity calculation.

The whole set of recovered blocks was supposed to undergo a “reconditioning” process, including the PM removal, the crystal back surface polishing with diamond-based abrasive tool, the single PMs gain characterization and grouping in quartets with similar gains, the final re-coupling of the PMs and block shielding.

A set of “reconditioned” blocks have been tested with the method described in section 3.2 and their performance have been compared to a set of original blocks. An overall degradation of the detection performance has been verified on all the tested “reconditioned” blocks, which showed lower amplitude output signals probably link to a reduction of the collected scintillation light. Various correction methods have been tested, with unsatisfactory results. According to the outcome of these tests, summarized in [Sandjong et al. 2017](#), the collaboration finally opted to adapt the camera design for the use of original, “non-reconditioned” BGO blocks.

Thirty original blocks are now available to compose the absorber detector. In addition to the already presented features, it must be noticed that the lateral surfaces of the original blocks, as well as the half of the PM length, are covered by a reflecting material which ensures the complete collection of the scintillation light. This is probably a component which was not well reproduced during the reconditioning process. The whole structure is then protected by a 1 mm thick aluminum foil, which also isolates from external light contamination.

Figure 3.5a shows one BGO block before the coupling to the PM quartet: the streaked structure is clearly visible, as well as the white reflecting material separating the pseudo-pixels and the one surrounding the block lateral sides. As mentioned, the same material also covers part of the photo-multiplier tubes, as shown in picture 3.5b, where the four PMs are glued to the block back surface. The described aluminum cover is visible in figure 3.5c, while in figure 3.5d a scheme of a block together with the related PM quartet is given. The spatial reconstruction logic is also reported in the same figure. To be noticed that the streaked structure of the pseudo-pixels depends on their position in the block: the reflecting streak covers about three fourth of the block thickness for the for the lateral pseudo-pixels, while it is limited to half of the block thickness for the central ones.

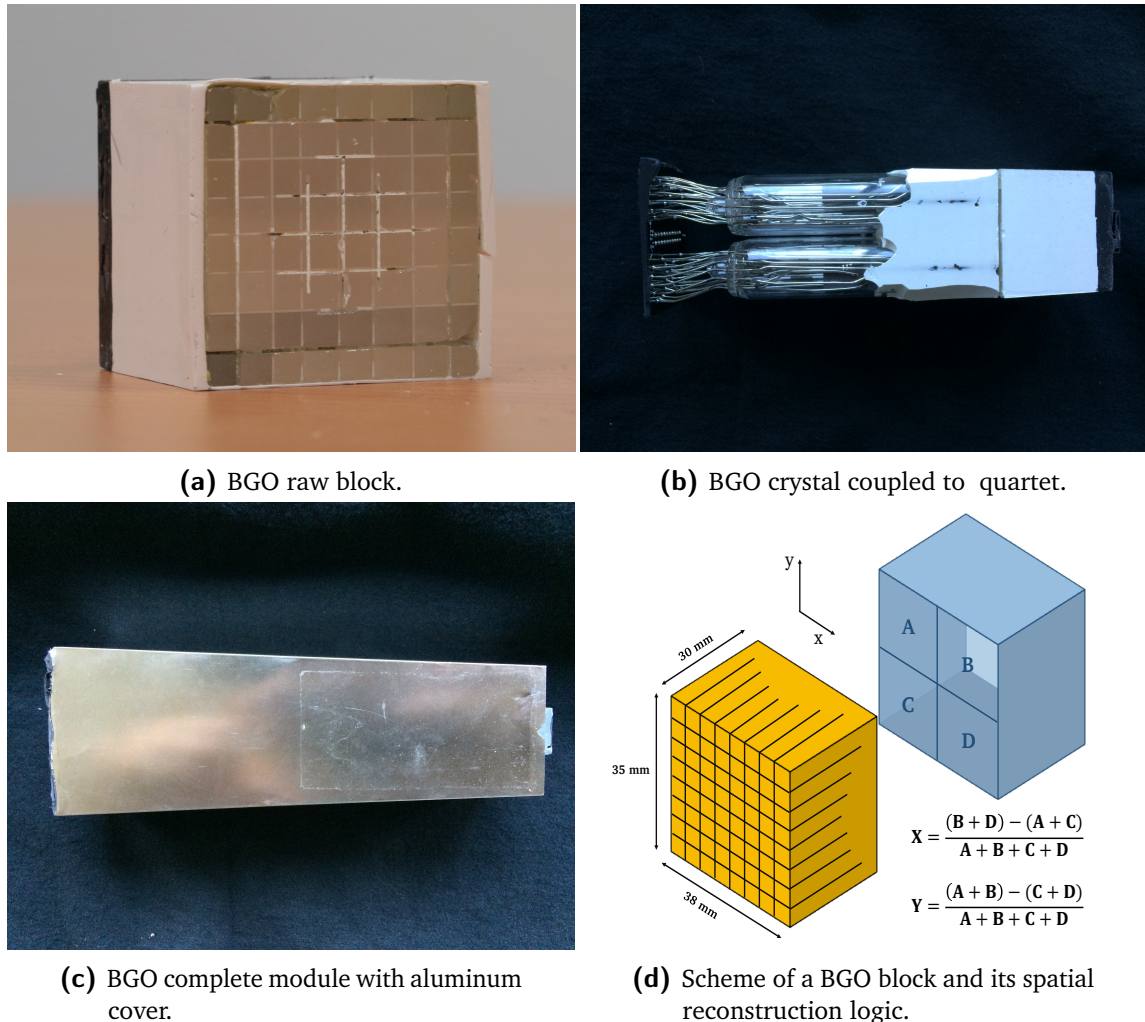


**Figure 3.5:** Absorber modules.

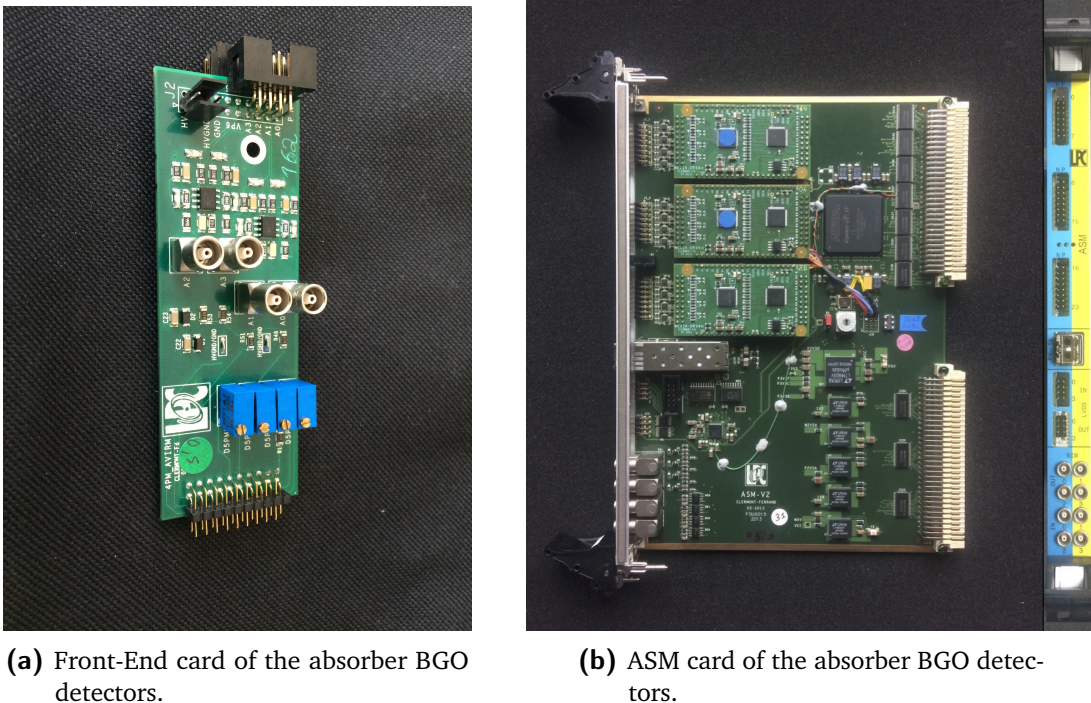


**Figure 3.6**

#### 3.1.3.1 Absorber Front-End and read-out cards

A custom front-end card has been designed and produced by the LPC research group and is used for the read-out of each BGO block. The card is equipped with four voltage modulators which divide the provided high voltage on the 4 photo multiplier tubes. The voltage sent to each can be mechanically tuned via screw-potentiometers on these modules. The card is equipped with differential output channels, through which the PM signals are sent to the read-out card, called ASM card. A picture of the FE card is given in figure ???. To be noticed that 4 analog output channels has been added on some cards in order to allow laboratory tests with a signal treatment based on standard electronics modules, as described in section 3.2.

#### DESCRIPTION OF THE ASM CARD

#### 3.1.3.2 Absorber mechanical support

A first mechanical structure for the absorber detector was initially conceived by the LPC group in order to hold up to 100 modules, foreseen by the original camera design. The reduction of the number of available blocks caused by the “reconditioning” process failure make necessary an adaptation of such a support. The new design has been carried out by the mechanics group of the IPNL in order to be compact and flexible in terms of detection modules setup. Figure 3.7 displays both a picture and a scheme of the absorber configuration with its mechanical support. The two lateral sides are built with Poly Methyl Metacrylate (PMMA) boards connected by metal bars, and the BGO blocks can be arranged in up to 5 rows of variable size, ranging from 3 to 7 blocks. Each block row is supported by a thin metal foil, designed to reduce at minimum

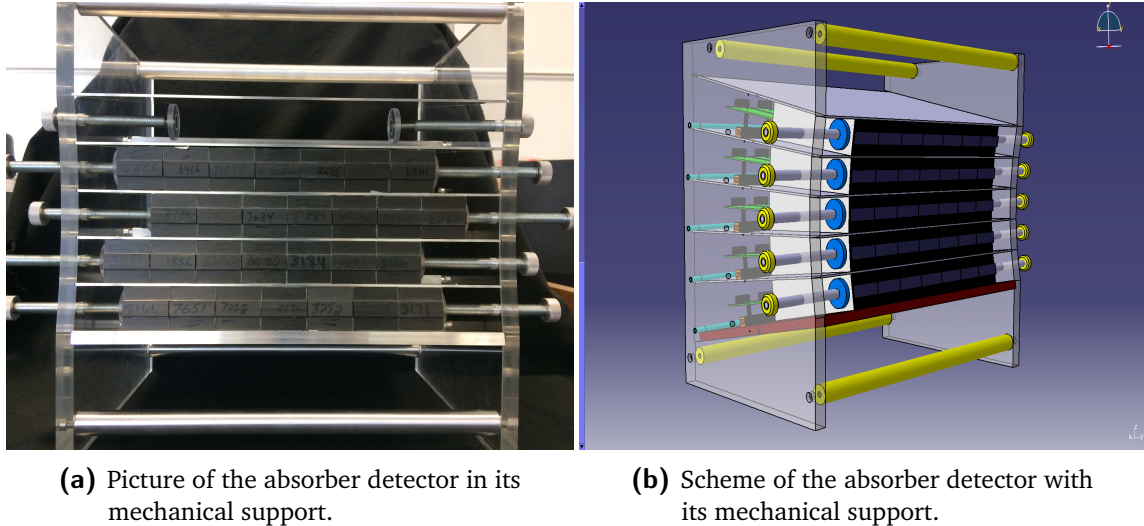


**Figure 3.7:** Absorber front view with the BGO block lines arranged in the mechanical support (left). Scheme of the BGO absorber with its mechanical support (right).

the blocks separation and to respect the original ring geometry deriving from the SIEMENS PET system. The blocks composing a row are then laterally pressed via two screws on the two sides of the structure, which can also be used to adapt the rows relative position horizontally. On the back side, a metal bar is added to avoid undesired movements, and the FE cards are fixed with plastic pillars. The realized support results to be versatile, compact and adapted to the prototype tests for both the Compton camera (where a squared setup is preferred) and the multi-collimated one (where the collimator geometry must be fit by the absorber geometrical configuration).

### 3.1.4 Beam tagging hodoscope

A beam tagging hodoscope is being developed in parallel to the two gamma cameras, mainly for background rejection and reconstruction optimization purposes [CIT]. As already mentioned, the detection of prompt-gammas (with mechanical or “electronic” collimation), is affected by the presence of other secondary particles produced during the ion beam irradiation, mainly neutrons. This background source can be efficiently identified and removed by applying TOF selection windows to the data acquisition. The TOF measurements can be performed using the accelerator radio-frequency signal as reference, but a direct beam detection results to be more accurate. An auxiliary detector is then needed before the beam interaction in the patient.

The CLaRyS hodoscope prototype is designed to provide space and time information about the incoming primary beam, particle by particle or bunch by bunch, depending on the beam intensity and detector efficiency and rate acceptance which must be characterized. In addition to the already explained use of the time information, a space primary particle tagging can be used to improve the reconstruction accuracy and constraint the possible reconstructed emission vertex in case of analytic reconstruction approach for both the multi-collimated and Compton cameras (see chapter 2).

The detector under development is based on squared  $1 \text{ mm}^2$  polystyrene scintillating fibers BCF-12, 140 mm in length, provided by Saint Gobain ([SaintGobain 2017](#)). A picture of the

hodoscope on its mechanical support (detailed in the following) is presented in figure 3.8. The fibers are arranged into two perpendicular planes for a two-dimensional spatial information: each plane is composed of 128 fibers, for a total active area (for 2D measurements in coincidence) of  $128 \times 128 \text{ mm}^2$ . The active detector surface is completely covered with black reflective tape, which shields from external light. The scintillation light produced in the fibers by an ionizing particle depositing energy is transported to the read-out system via FORETEC optical fibers (1.55 cm diameter, 1 m length), which are connected to the scintillating fibers thanks to a custom mechanical support and to a proper gluing process (see figure 3.9a). Each scintillating fiber is read-out on both sides to optimize the detector efficiency and improve the time resolution which is not depending on the interaction position along the fiber with this configuration, so that the total number of read-out channels is 512. The signal read-out is ensured by 8 multi-anode PMs Hamamatsu H8500 ([Hamamatsu 2006](#)) shown in figure 3.9c. The optical fibers are connected to the PM anode surfaces through a plastic custom mask, shown in figure 3.9d. The PMs are equipped with custom black boxes which operate as mechanical support and external light protection (see figure 3.9a). In order to provide further light isolation, the whole PM boxes are covered with black tape.

The optical fibers are connected to the PMs with the aim of increasing the maximum counting rate. 4 PMs are dedicated to the read-out of the horizontal fibers, and 4 to the vertical ones, and the neighboring fibers are connected to different PMs. An active area of  $4 \times 4 \text{ mm}^2$  on the two planes is then read-out by all the 8 PMs. Moreover, the two sides of the same scintillating fiber are connected on the same PM. This fiber connection logic also improves the detector robustness; in case of problem on one PM, only 1 mm of 4 mm is lost on a single plane, so that the detection of the beam is still possible on the whole active area.

Each PM is connected to a single custom FE card. The hodoscope FE cards have been developed by the IPNL electronics group: their design is described in section 3.1.4.1. 8 FE cards are then used for the read-out, and the collected data are sent to the acquisition system described in section 3.1.5.

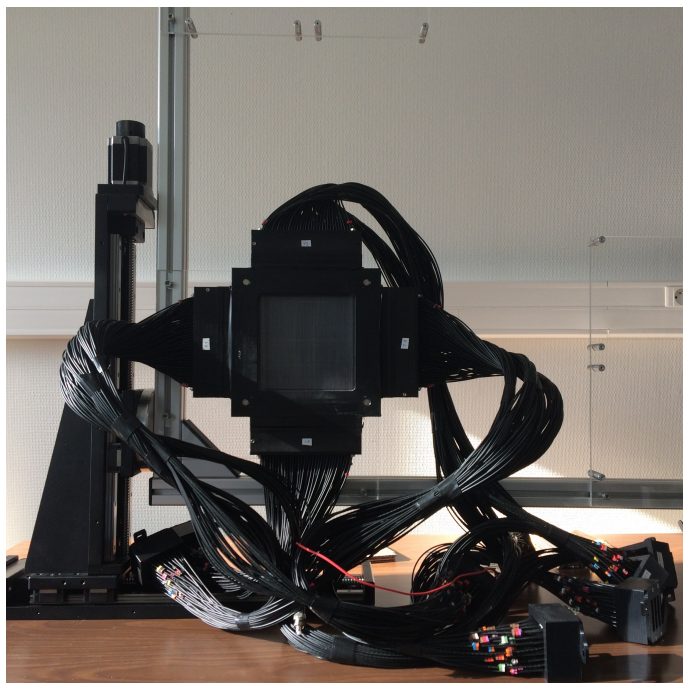
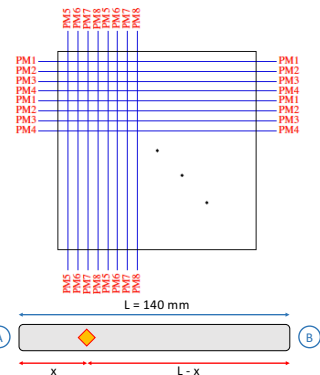


**Figure 3.8:** CLaRyS scintillating fiber hodoscope on its 2-dimensional moving table.



(a) Scintillating fiber hodoscope during mounting process.



(b) Scheme of the scintillating fiber connection to the PMs (top) and of the double-sided fiber read-out (bottom).



(c) Hodoscope read-out PMs Hamamatsu H8500.



(d) PM plastic mask for optical fiber connection.

**Figure 3.9:** Details of the CLaRyS scintillating fiber hodoscope setup.

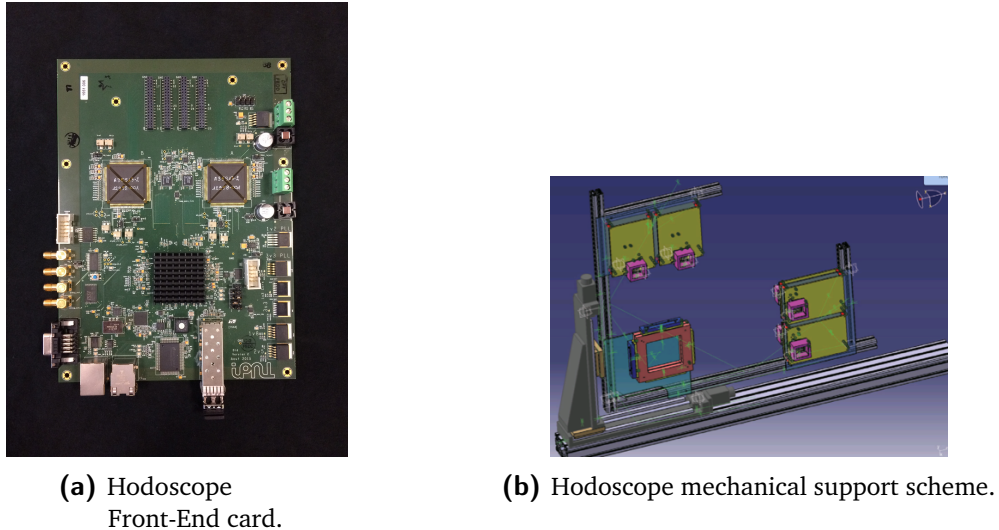


**Figure 3.10:** Hodoscope Front-End card developed at IPNL.

#### 3.1.4.1 Hodoscope Front-End card

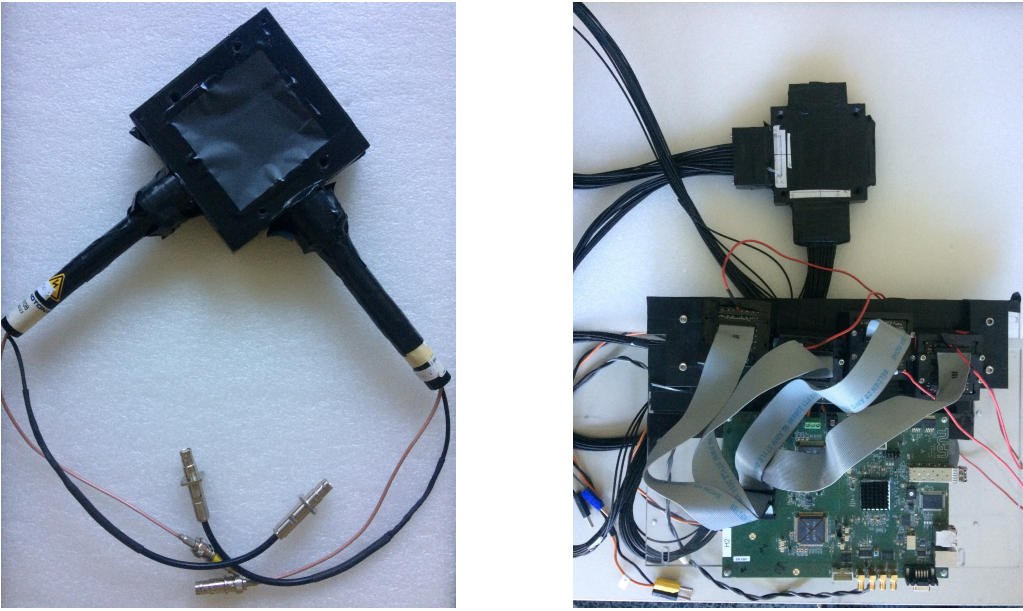
The hodoscope is designed to tag in space and time the incoming beam ions, so that the signal read-out must be optimized to provide accurate time measurements and an high detection rate acceptance, with reduced dead time and detection efficiency close to 100%. In particular, the design requirements include a maximum counting rate acceptance of  $10^8$  Hz per detection plane, with a time resolution of 1 ns ([Krimmer et al. 2014](#)). The hodoscope FE card shown in figure 3.10a has been developed by the IPNL electronics group to fulfill the listed requirements. The Hamamatsu PM is connected to the 64-channel connector (4 connectors of 16 channels each) and two custom ASICs are dedicated to the data first treatment (32 channels each).

CARD DESCRIPTION ([Deng et al. 2012, 2013](#)).

#### 3.1.4.2 Hodoscope mechanical support

The beam tagging hodoscope is set between the beam nozzle and the patient and requires a dedicated mechanical support. In order to profit of the large active area and to be able to remotely control the hodoscope position in the beam transverse plane, the detector is mounted on a 2-dimensional moving table (see the picture in figure 3.8), which also supports the FE cards. Detector and FE cards are then integral and translate together. A scheme of the moving table is given in figure 3.10b.

The 2-axis table is provided by Beijing Winner Optical Instruments; it is composed of two motorized linear stages, connected via a right angle bracket. The two stages have a moving range of 30 cm each and the stepper motors have a step resolution of 20  $\mu\text{m}$ . The employed motor controller is a Newport XPS-Q8 ([Newport 2017](#)), equipped with 8 channels for the simultaneous control of a maximum of 8 motors. The movements are steered with an online interface or with a LabVIEW based program, which will be integrated in the final setup of the slow control software under development with the cameras.



(a) Hodoscope small prototype, 1×1 scintillating fibers.

(b) Hodoscope small prototype, 32×32 scintillating fibers.

**Figure 3.11:** Hodoscope small prototypes.

### 3.1.4.3 Small hodoscope prototypes

Before the production of the large active surface hodoscope prototype described in section 3.1.4, two smaller prototypes have been produced and tested in order to assess the potential of such a kind of detector for the required application. The first and simplest version consisted of one single scintillating fiber per plane, and the readout was performed with two PM tubes directly coupled to the scintillating fibers, without optical fibers. A picture of this prototype is given in figure 3.11a. This simple version of the detector has been used as a demonstrator of the basic detection principle.

A second small size version of the final detector has been produced with almost the same features as the large area prototype but with simplified read-out logic. It is equipped with two perpendicular planes of 32 1 mm<sup>2</sup> scintillating fibers each (Saint Gobain BCF-10 ([SaintGobain 2017](#))), with a length of 4 cm and a total active area for a 2D read-out of 32×32 mm<sup>2</sup>. As in the big hodoscope, the scintillating fibers are coupled to FORETEC optical fibers which transfer the scintillation light to 4 Hamamatsu H8500 PMs. 16 channels per PM are used, so that 2 PMs are dedicated to the horizontal fibers and 2 to the vertical ones, and the signal read-out is performed on a single side of the scintillating fibers. As the total number of read-out channels is 64, a single FE card is enough for the whole detector. In figure 3.11b the 32×32-fiber hodoscope prototype is shown together with its FE card; 4 connection cables (16 channels each) are used to couple the PMs to the FE card.

The 32×32-fiber hodoscope prototype has been tested in 2014 on proton and carbon ion beams (at the Grand Accelerateur National d’Ions Lourds (GANIL) - 75 MeV/u <sup>13</sup>C, Heidelberg Ion Therapy Center (HIT) - protons and carbon ions at various energy, Institut de Physique Nucléaire d’Orsay (IPNO) - 25 MeV protons) with the first version of the FE card (see section 3.1.4.1): an efficiency of more than 90% has been retrieved, with a time resolution of

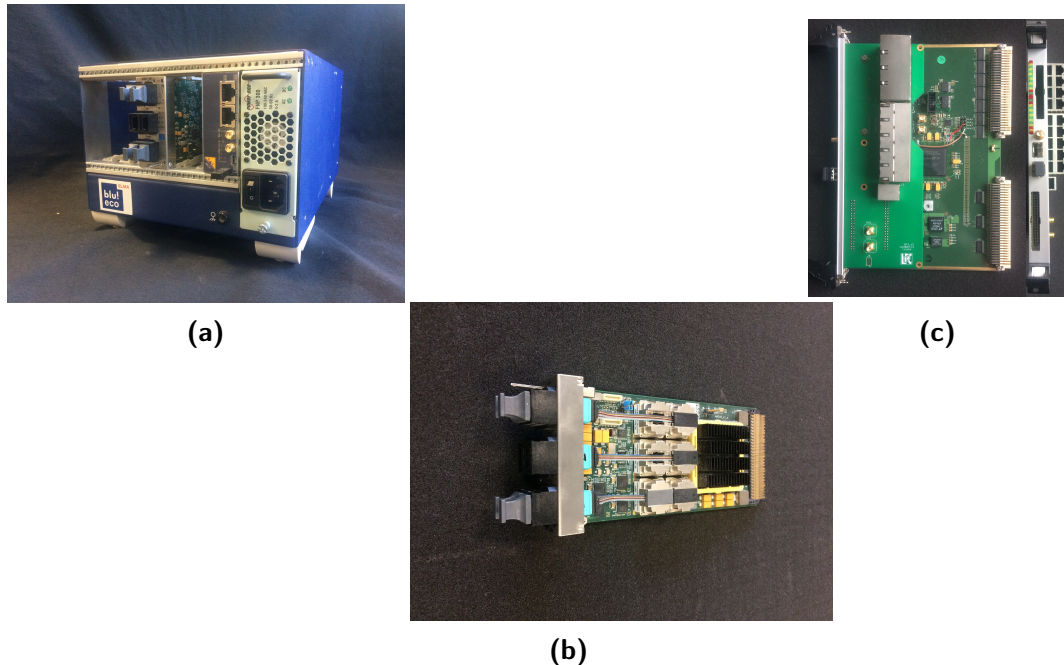


**Figure 3.12**

1 ns FWHM (timing measurements performed with respect to the accelerator high frequency signal). Some more details about this beam tests results are given in chapter 6. The final version of the FE card has been also tested with this detector, and the test description and results are presented in chapter 6.

### 3.1.5 Camera electronics and acquisition system

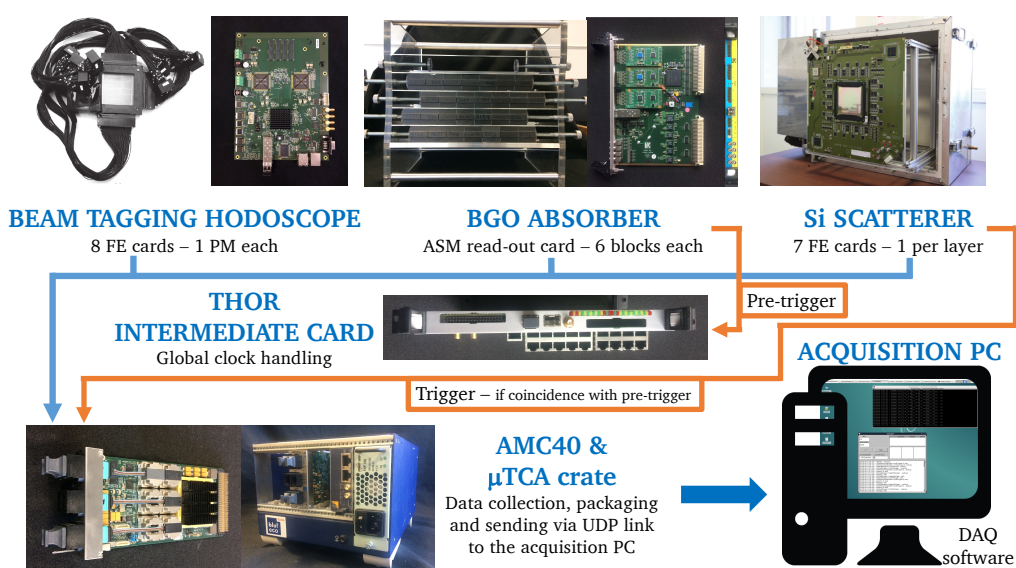


**Figure 3.13:** Schematic view of the Compton camera acquisition system. For the multi-collimated camera, the trigger and pre-trigger signals are the same.

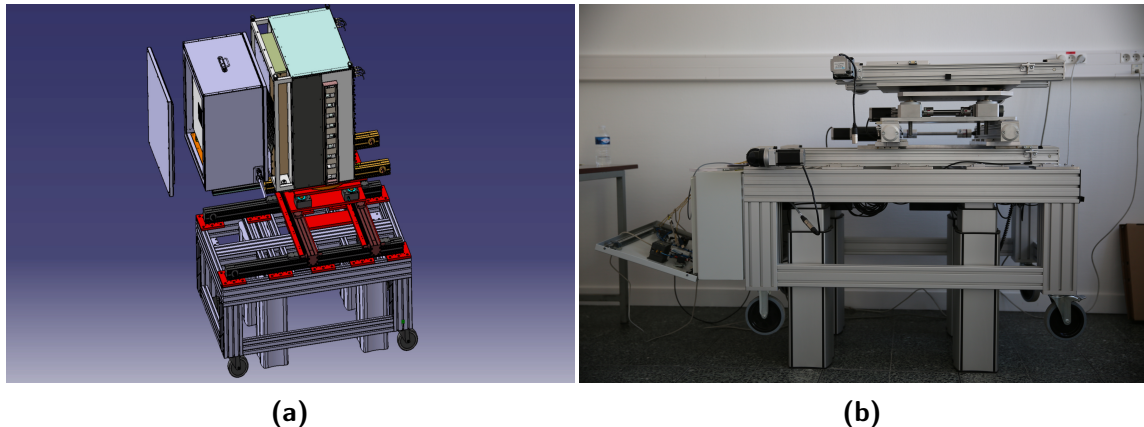


Figure 3.14

### 3.1.6 Camera slow control, acquisition and monitoring software

### 3.1.7 Camera integration and mechanical support

## 3.2 Camera component characterization and development status

As detailed in the previous sections, the CLaRyS TOF gamma cameras are equipped with various detector components with very different features. Each part must be separately studied in order to characterize its behavior and allow the final camera integration and operation.

I mostly worked on the beam tagging hodoscope and on the BGO absorber, and in the next paragraphs the performed measurements are described in details. Concerning the scatterer stack, the results achieved before the beginning of my PhD thesis are briefly described for the sake of completeness.

The results presented in this section also introduce the following one (3.3), where all the development steps still needed for a clinical implementation of the cameras are explained.

### 3.2.1 Hodoscope PMs characterization

The beam tagging hodoscope read-out is performed via 8 multi-anode PMs, Hamamatsu H8500 ([Hamamatsu 2006](#)), shown in figure 3.9c. In order to guarantee a uniform response of the whole detector active area, composed of 256 scintillating fibers, the PMs must be previously characterized in terms of gain with a light source of fixed and known wave-length and intensity. The source selected for the measurements is a blue Light Emitting Diode (LED) (Hewlett-Packard HLMP-CB), installed on the test-bench shown in figure 3.15a and described in the following. The test-bench has been developed by the LPC group (see [Gaglione 2013](#)) and adapted at the IPNL to a different acquisition system.

The goal of the characterization measurements is to trace a gain map of the whole PM surface, with the aim of storing calibration data to be used to both tune the PM working

parameters (supply voltage and threshold) and correct the collected data. This is achieved by scanning the PM photo-cathode surface with the LED. The LED is so mounted on a motorized double-axis table, controlled by two G203V stepper modules provided by GeckoDrive Motor Controls ([GeckoDrive 2010](#)). The two axes have a total range of 20 cm each, and the step resolution achieved by the controllers is 20  $\mu\text{m}$ . A metal support is set on the table in order to fix the LED. It produces light pulses synchronized with a pulse generator, which is also used as trigger signal for the acquisition system, as detailed later. The light pulse produced by the LED is split into two pulses with a 45° mirror: one pulse is sent to the H8500 PM to be tested via optical fiber, in order to obtain a light beam perpendicular to the cathode surface (FWHM beam width estimated in 0.5 mm), the second one is detected by an Hamamatsu R5600 PM ([Hamamatsu 1995](#)), used as reference for the correction of LED temperature fluctuations. The PM under tests if fixed below the optical fiber output with a plastic support, not connected to the moving table. The whole described system is contained in a black box for external light shielding.

The output signals from the H8500 PM are initially amplified by custom pre-amplification cards: 8 cards are available and have been characterized in terms of amplification gain. Once amplified, the signals H8500 PM, together with the output of the reference PM, are sent to the acquisition system composed of a National Instrument PXI Express 1082 ([NationalInstruments 2010](#)) equipped with two 8-channel flash Analog-to-Digital Converter (ADC) modules (NI PXI-5105) and a two-channel ultra-fast digitizer (NI PXI-5154). The flash ADC modules have a maximum sampling rate of 60 MHz and are used for the read-out of the H8500 PM signals, while the ultra-fast digitizer, able to sample at a frequency up to 1 GHz, is used for the reference PM.

The acquisition and control software is developed with LabVIEW (2009) installed on the PXI; a picture of the software user interface is shown in figure 3.15c. The PXI receives the signals form the two PMs and is also connected to the table stepper modules, so that the LabVIEW software can handle and synchronized data acquisition and table movements. The table movements can be automatized via LabVIEW macros, where step size, number and direction are stored and then used for the acquisition. The acquisition trigger, as mentioned, is given by the pulse generator which also control the light pulses of the LED; in this way, a fixed number of pulses per table position can be recorded, and the measurement process is completely automatic. During the acquisition, the LabVIEW software automatically correct the collected data according to the reference PM signal amplitude and to the pre-amplification card gain. Given the limited number of flash ADC channels, only 16 PM pixels can be characterized per acquisition; four acquisitions are needed to scan the complete PM surface.

Each performed acquisition is set to scan a matrix of 4×4 PM pixels, and safety margins are arranged on the PM sides in order to ensure a complete surface irradiation. As shown in the schematic view of the PM in figure 3.16a, the total PM size is 52×52 mm<sup>2</sup>, for an active area of about 49×49 mm<sup>2</sup>. The active area of the pixels on the borders is slightly wider than the central ones. In order to optimize the measurement process, a preliminary analysis has been done for the definition of the needed step length, and the details are reported in [Coudurier 2015](#). A trade-off between measurement accuracy, required time and collected data size has been found with a step of 800  $\mu\text{m}$ , so that each pixel is scanned with approximately 64 measurement points and the transition between neighboring pixels can be appreciated. To be noticed that for each irradiated point, 100 LED pulses are sent to the detector and the average amplitude value is calculated and collected.

The 8 Hamamatsu PMs have been completely scanned with and without the optical fiber

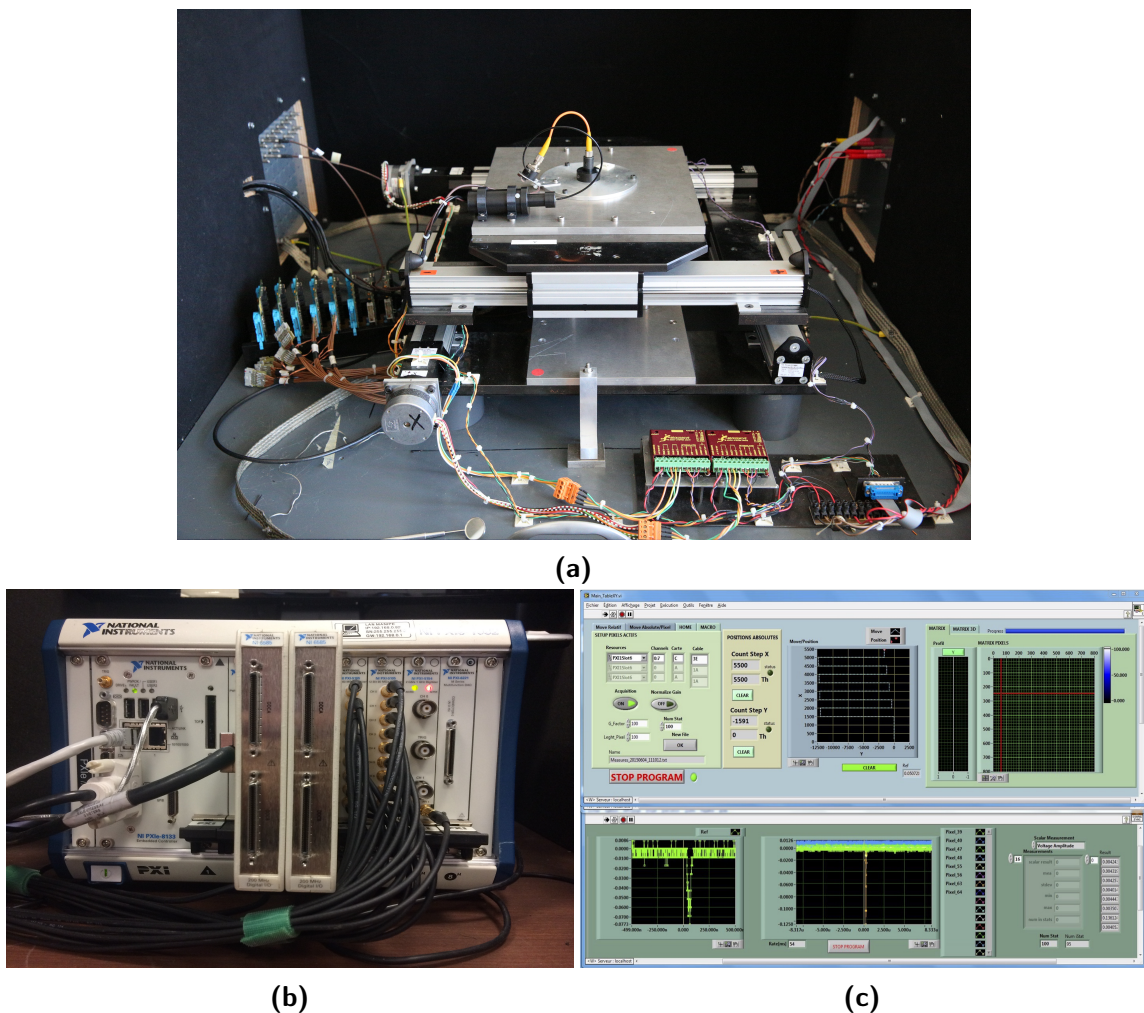


**Figure 3.15**

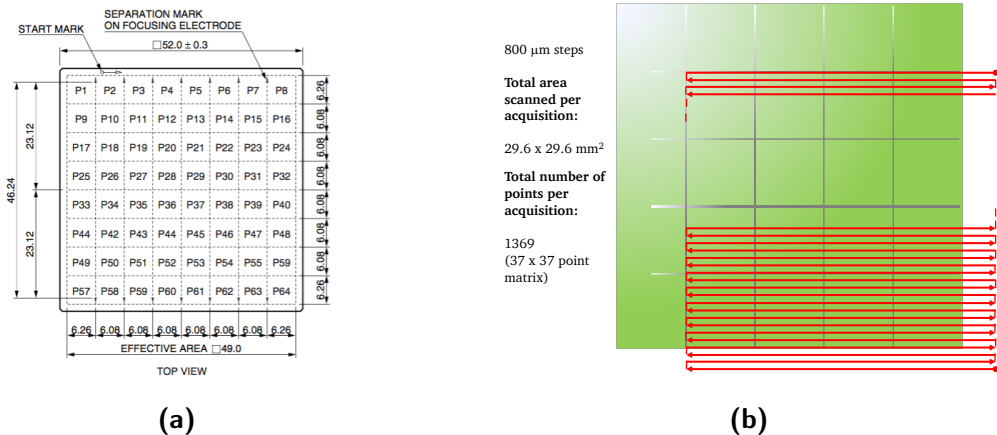


Figure 3.16

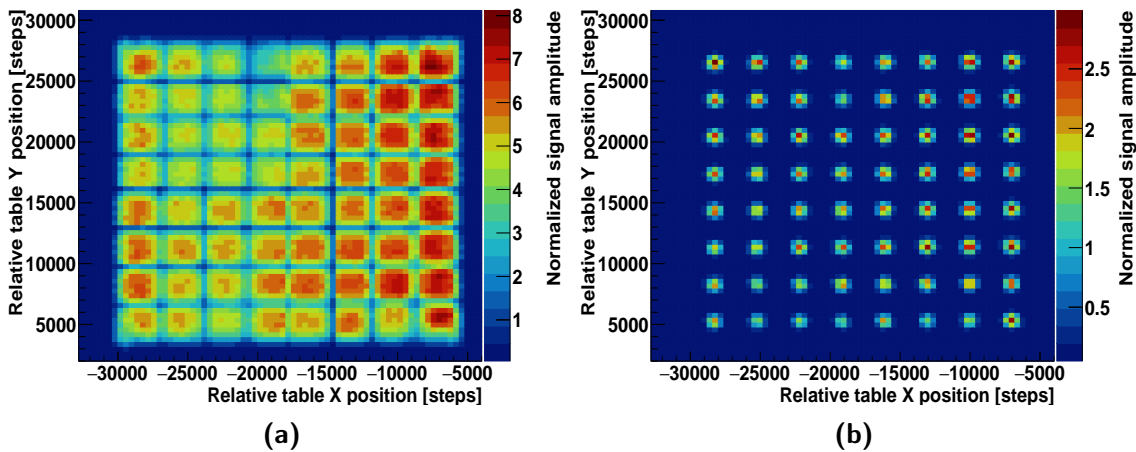


Figure 3.17

mask used in the hodoscope and shown in figure 3.9d, and the results are shown here for one reference PM. A complete result database has been created for calibration purpose.

#### 3.2.2 Hodoscope fiber test with electron source

#### 3.2.3 Absorber BGO blocks characterization

The BGO modules composing the Compton and multi-collimated camera absorber have been recovered form a SIEMENS PET system: they have been originally optimized for the detection of 511 keV photons from positron annihilation, and they have to be tested for the new gamma detection system, which must be able to deal with photons in the prompt-gamma energy range, i.e. from some hundreds of keV to a few MeV.

Each block must be characterized in terms of spatial and energy response, and the read-out PMs have to be calibrated to obtain a uniform response on the whole block surface (see section 3.1.3 for the detector description). The employed method relies on the work presented

in [Rogers et al. 1994](#) and [Tornai et al. 1994](#) and on the calibration process described in [Golnik 2015](#) and [Hueso-González et al. 2015](#), and has been extended with more refined features.

The measurements are performed with the irradiation with gamma sources, emitting photons at defined energies: in particular, we used 511 keV and 1275 keV photons from a  $^{22}\text{Na}$  source, and the two photons emitted by a  $^{60}\text{Co}$  source, at energies of 1173 keV and 1332 keV.

The employed  $^{22}\text{Na}$  source is a cylindrical source with a diameter of 1 cm, and an activity of about 400 kBq: it has been placed at a distance of about 5 cm from the block entrance surface, with the center of the source facing the center of the block transverse surface. The  $^{60}\text{Co}$  source has been installed in a lead cylindrical container (12 cm radius and 35 cm height), equipped with three different apertures: point-like ( $2 \times 2 \text{ mm}^2$ ), linear ( $2 \times 50 \text{ mm}^2$ ) and squared ( $50 \times 50 \text{ mm}^2$ ). The design of the lead container has been studied in simulation to ensure the proper radiation protection, and produced according to the specifications defined by the IPNL mechanics group. The activity of the  $^{60}\text{Co}$  source is about 1.7 MBq, and the square shape has been used to obtain an homogeneous irradiation of the BGO block, with the block set with the center of the entrance surface corresponding to the source position, at a distance of 12 cm.

The signals produced by the four PMs of each block are collected via four analog outputs on the front-end card (see picture 3.6a). The four retrieved signals per event are treated via standard Nuclear Instrumentation Module (NIM) modules in order to be adapted to the acquisition systems and measurement purposes.

Two different acquisition systems have been used for this characterization work. First, the PXIe described in section 3.2.1 with its two flash ADC read-out modules, 8 channels each, is used for the spatial and energy characterization and calibration of the tested blocks. The raw signals coming from the four PMs are amplified and shaped via NIM modules, which were fine tuned via a pulse generator in order to adapt the amplification factor of each channel (an amplification factor of about 50 has been applied to the raw signals). The amplified signals are then split in order to be treated for trigger purpose. The trigger for the acquisition is based on the sum of the four signals, and a fixed threshold is applied for background rejection. The employed discriminator provides the logical trigger signal, which is sent to the trigger input of the ADC modules on the PXI. The four amplified signals, conveniently delayed, are sent as inputs to the ADC modules on the PXI, together with the sum signal which is used for experimental verification of the acquisition setup. A LabVIEW based acquisition software, developed for this particular application by the IPNL group, provides real time event visualization together with a partial, on-line spatial reconstruction of the events, and stores them in text files for further analysis. A second threshold can be set at the software level in case particular selections are needed during the acquisition, otherwise the event selection is performed at the analysis stage.

Concerning the timing characterization measurements, an eight-channel signal digitizer at 3.2 GS/s has been employed for high time resolution acquisitions. The so called WaveCatcher, shown in figure 3.18a, has been developed by the Laboratoire de l'Accélérateur Linéaire (LAL) in Orsay and the Institut de Recherche sur les lois Fondamentales de l'Univers (IRFU) in CEA-Saclay, and its features are detailed in [Breton et al. 2014](#). The digitizer is connected to the acquisition PC via USB cable, and the data read-out and storage is performed thanks to a custom acquisition software. The measurements are based on the coincidence detection of back-to-back 511 keV photons emitted by a  $^{22}\text{Na}$  radioactive source, in order to be able to compare the time response of the tested BGO block to a reference fast timing scintillator. An external trigger is then provided to the WaveCatcher by treating the BGO block and reference scintillator signals with logic coincidence NIM modules, after proper discrimination. Further details are given in section 3.2.3.3.

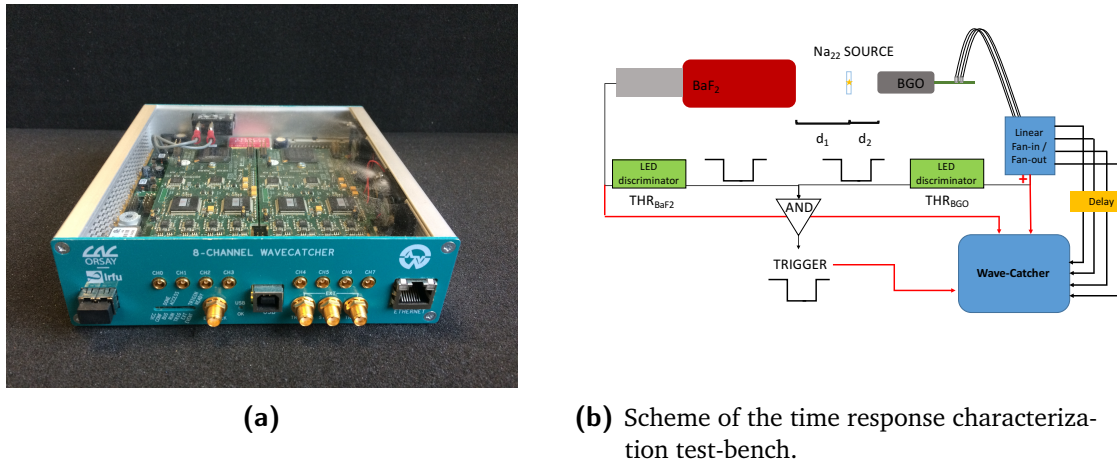


**Figure 3.18**

#### 3.2.3.1 Space and energy calibration and characterization

The space and energy calibration process is mainly divided into four parts:

- $^{22}\text{Na}$  irradiation: the block is irradiated with the sodium source and the raw ADC distributions for the four PMs are retrieved. The highest ADC values are taken as reference to equalize the distributions. Four energy calibration factors are extracted and used to the data correction; this correction corresponds to a PM gain equalization.
- $^{60}\text{Co}$  irradiation: once the calibration factor are extracted thanks to the  $^{22}\text{Na}$  irradiation data, the block is exposed to the  $^{60}\text{Co}$  source. The collected data are analyzed as in the previous step and calibrated according to the already calculated correction factors. The energy spectrum, the mono-dimensional spatial projections and the flood map (two-dimension position map) are produced.
- Pixel identification: the custom algorithm briefly described in paragraph 3.2.3.2 has been developed to identify the pseudo-pixel positions on the flood map. It is applied to the  $^{60}\text{Co}$  irradiation data and the pseudo-pixel position map is stored.
- Pixel energy calibration: the  $^{22}\text{Na}$  irradiation data are re-analyzed in this last calibration step in order to assign each interaction to a single pseudo-pixel according to the pixel position map obtained with the  $^{60}\text{Co}$  data. The energy spectrum of each pixel can be then produced and the two identified peaks (corresponding to the two photon energies emitted by the sodium source - 511 keV and 1275 keV) can be used to equalize the pseudo-pixel response. The sum of all the pixels spectra produces the block energy spectrum. At this stage, the ADC channel values are calibrated to obtain the absorbed energy values in keV.

It is worth to notice that the  $^{60}\text{Co}$  irradiation is useful for the pixel identification given the high energy and narrow energy range of the emitted photons. The equalization factors obtained with the sodium source irradiation have been verified to be consistent with the  $^{60}\text{Co}$  irradiation

data, as expected. In addition to this, the pixel position map obtained with the  $^{60}\text{Co}$  irradiation data has been verified to fit with the  $^{22}\text{Na}$  data, which presents larger distributions around the pseudo-pixel center. The whole method results to be robust.

#### 3.2.3.2 Pixel identification and energy calibration algorithm

An automatic algorithm has been developed to identify the block pseudo-pixel positions starting from the calibrated and reconstructed data. Starting from the integrated mono-dimensional spatial projections along the two axes obtained from the calibrated flood map, the distributions peaks and valleys are derived with the ROOT methods included in the TSpectrum class and simple analytic calculations. With the resulting valley positions, a grid is created on the flood map with a pixel-by-pixel center of gravity calculation: each grid portion should contain a single peak, corresponding to the center of the related pseudo-pixel. Spatial reconstruction artifacts can determine a non complete identification of the 64 pseudo-pixels, and the algorithm is able to check for errors of this kind. In case the identified valleys are less than seven on each axis (corresponding to a  $8 \times 8$  pseudo-pixel array), the projection of each identified region (rows and columns) on the two axis is created and re-analyzed looking for peaks and valleys as before. The values obtained for the rows and columns are compared and a new, fine-tuned grid is produced. This process can be iterated a given number of times if a complete grid is not obtained. Once the pseudo-pixels grid is fixed, the maximum of each region is automatically identified and its position defines the pseudo-pixel center relative position in the map. The event data are then assigned to the pseudo-pixels with the application of two different possible criteria:

- Calculating the distances to the center of all the identified pseudo-pixels and assigned the interaction to the pseudo-pixel with the minimal one;
- Defining a new grid composed by the average points on the borders between pixels and comparing their position to the reconstructed one to assign it to the most likely pseudo-pixel. This is done by calculating the minimal distance between a column and a row average point with respect to the reconstructed event and then calculating two external products, between the vector connecting the reconstructed point and closest column (row) average point and the vector connecting this average point to the previous or next one on the same column (row). The sign of the products defines the column (row) where to assign the interaction. Knowing the relative position of the interaction point with respect to the two minimal distance points on row and column, the correct pseudo-pixel is identified.

The two methods will be detailed in section 3.2.3.6 with the support of the results obtained with the reference block. The results given by the two methods are slightly different and will be detailed and discussed.

#### 3.2.3.3 Time response characterization method

The test-bench for the time response characterization has been set as shown in figure 3.18b. A Barium Fluoride ( $\text{BaF}_2$ ) mono-block scintillator, read-out by a single photo-multiplier tube,

has been used as reference detector. Its excellent time resolution makes it suitable for relative timing measurements in comparison to the BGO blocks. The reference scintillator and the BGO block under test have been set at random distances ( $d_1$  and  $d_2$  on figure 3.18b) from the  $^{22}\text{Na}$  source with the aim of detecting in coincidence the two 511 keV back-to-back photons resulting from the positron annihilation. The four raw signals coming out from the BGO block are summed with a NIM linear fan-in/fan-out module, and the resulting signal is sent to a leading edge discriminator and converted to a logic signal according to a fixed threshold. The single signal emerging from the reference detector passes through a selected threshold and is converted to digital. The two digital signals, 100 ns width, are then sent to a logic coincidence module to create the trigger input for the WaveCatcher acquisition system described in section 3.2.3. The four BGO output raw signals, the reference scintillator raw output signal and the sum of the four raw BGO signals are sent to the WaveCatcher for digitization.

For each coincidence event, the six collected signals are analyzed with focus on the signal rising edge. The time corresponding to the amplitude maximum and to 20%, 30%, 50% and 80% of the maximum is retrieved for constant fraction discrimination tests. In addition to this, a fixed threshold is used for fixed value discrimination.

Different comparison methods have been tested in order to identify the more robust one for the definition of the time resolution of the blocks. The chaotic structure of the single BGO raw signals leads to very variable results depending on the defined threshold, and the more stable results are given by the comparison of the sum of the four BGO signals and the reference scintillator with the arrival time identified by a fixed tuned threshold. With this method, the arrival time of each signal can be defined and the time difference distribution of the two signals can be produced.

The same analysis has been applied to a data set obtained with two identical  $\text{BaF}_2$  detectors exposed to the  $^{22}\text{Na}$  source in coincidence. This data set allowed for the definition of the reference scintillator time resolution.

The resulting BGO time resolution is defined as the FWHM of arrival time difference distribution between BGO block and reference scintillator, with the subtraction of the reference scintillator contribution via uncertainties composition calculation.

#### 3.2.3.4 Results: PM gain equalization

Figures 3.19, 3.20, 3.21, 3.22 show the effect of the PM gain equalization on the data collected with the reference BGO block irradiated with the sodium source. Figures 3.19a and 3.19b show the raw and equalized ADC profiles of the four read-out photo-multipliers (the peaks above 3000 ADC counts in figure 3.19a correspond to the saturation of the NIM linear fan-in/fan-out module used to handle the data read-out; these values are rejected during the equalization stage). Figures 3.20a and 3.20b show the projection on the two axes of the position of interaction reconstructed via Anger logic, before (left) and after (right) the PM gain equalization. Figures 3.21a and 3.21b show the ADC event spectrum, obtained by the sum of the ADC values of the four PMs, before (left) and after (right) the PM gain equalization. Figures 3.22a and 3.22b show the two dimensional event position map (this will be called “flood map” in the following), before (left) and after (right) the PM gain equalization; the interaction position is reconstructed via Anger logic (see figure 3.5d for details).

As shown by figures 3.19 to 3.22, the PM gain equalization performed in this first calibration step is mandatory to optimize the spatial and energy response of the tested block. Figure 3.20b

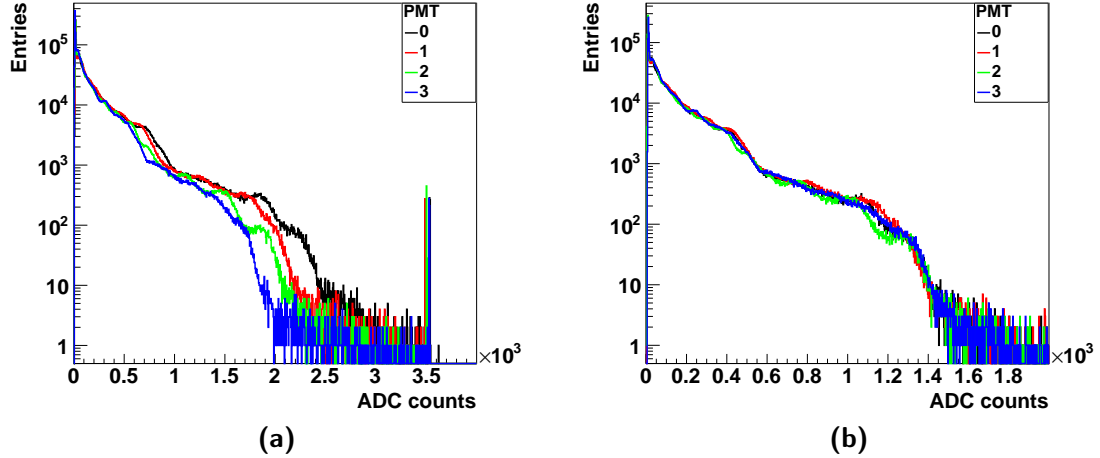


**Figure 3.19:** PM signal amplitude spectra before (a) and after (b) the PM gain equalization.

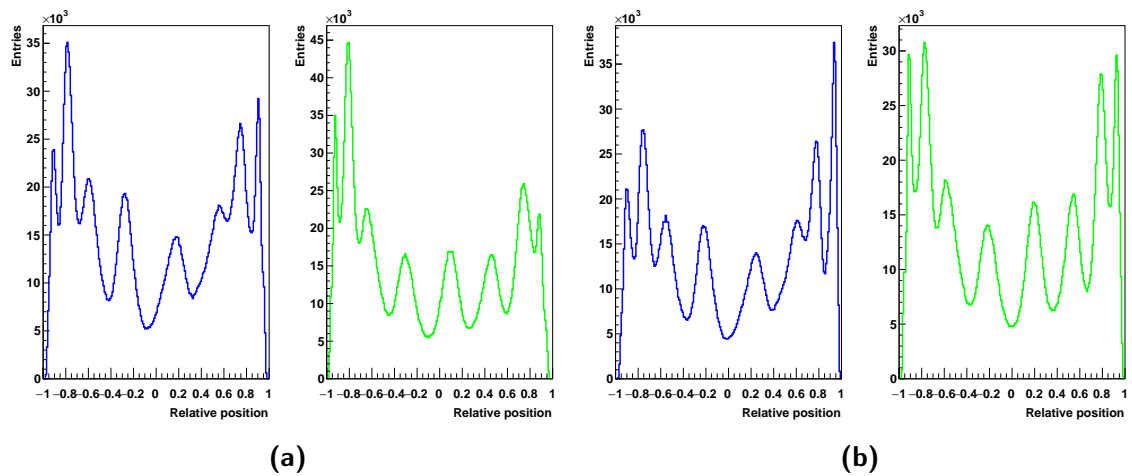


**Figure 3.20:** 1D integrated position distribution on the two transverse dimensions before (a) and after (b) the PM gain equalization. Blue curves: horizontal dimension. Green curves: vertical dimension.

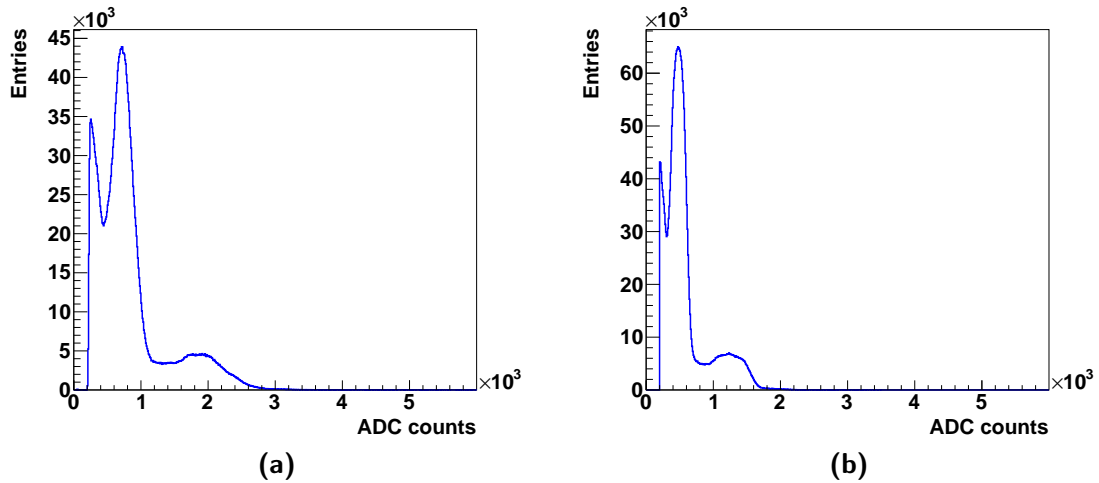


**Figure 3.21:** Block energy spectrum before (a) and after (b) the PM gain equalization.

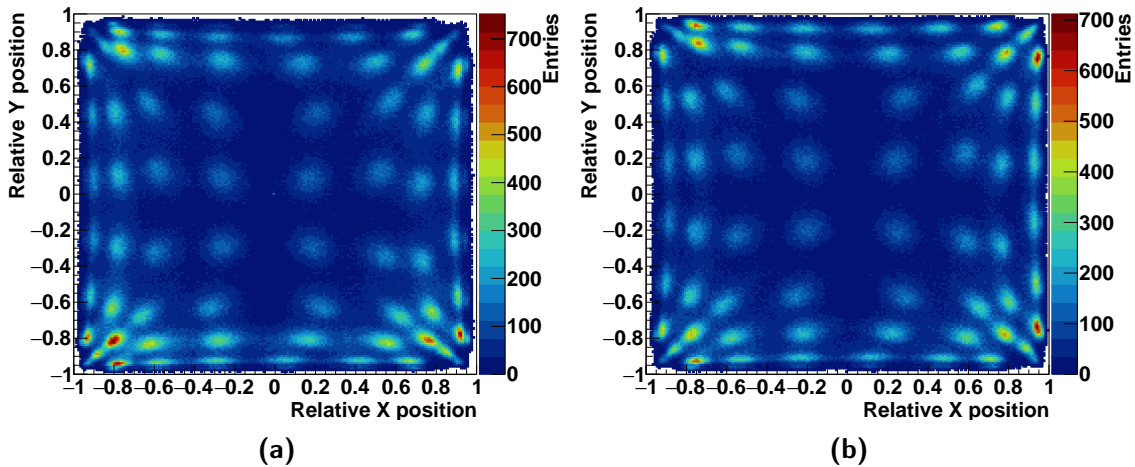


**Figure 3.22:** 2D reconstructed position map before (a) and after (b) the PM gain equalization.

highlights the better definition of the pseudo-pixels ensured by the gain equalization: the peak-to-valley ratio is increased, in particular for the most external pixels. The spatial response improvement is also reflected in a better energy response, as shown in figure 3.21b, where the two energy peaks of the sodium source are more narrow with respect to the ones obtained with the raw data. The obtained energy response is still not satisfactory, and the next steps of the calibration process are dedicated to the improvement of this result. The flood map in figure 3.22b shows how the gain equalization and the offset tuning allow to arrange the position map over the whole block surface; the borders are better defined and the pseudo-pixels on the block limits (especially on the corner) are better separated.

#### 3.2.3.5 Pixel identification

The results of the pixel identification algorithm described in section 3.2.3.2 are shown in figure 3.23. Figure 3.23a shows the identified average values of the pseudo-pixels positions

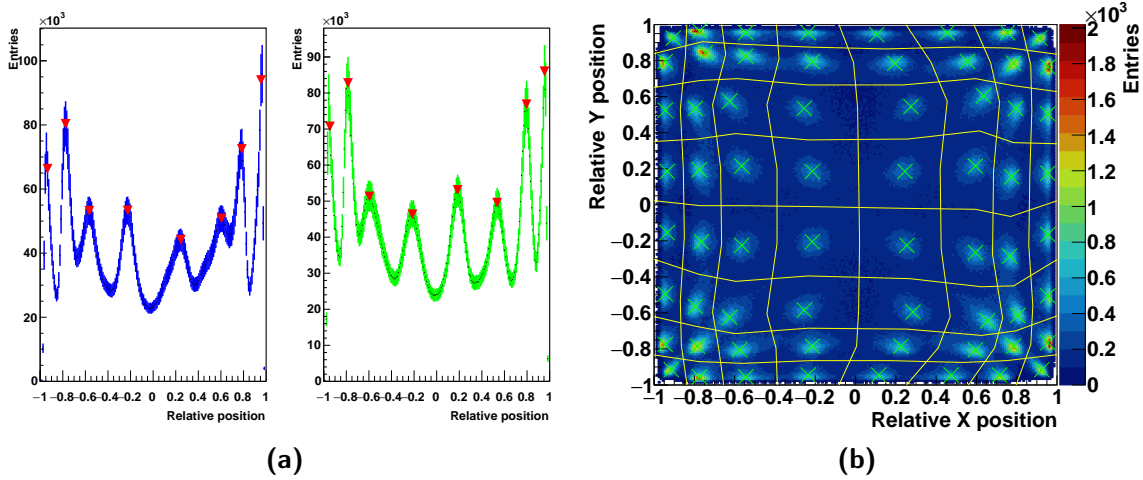


**Figure 3.23:** 1D integrated position distributions on the two transverse dimensions with the retrieved position of the pseudo-pixel average center (a). Reconstructed 2D map with the identified pseudo-pixels positions and surfaces.

on the two transverse dimensions. As already detailed in the description section, starting from these average positions, the single pseudo-pixels positions in rows and columns are extracted and the “valleys” between neighboring pseudo-pixels are used to define the grid shown in figure 3.23b together with the pseudo-pixel center position map.

### 3.2.3.6 Pixel energy calibration

Once the pseudo-pixel positions and the related grid are defined, each interaction can be assigned to a single pixel. The energy spectrum of each pixel is then separately studied in order to equalize the energy response on a pixel basis.

As already mentioned in section 3.2.3.2, two methods have been tested and compared for the interaction spatial assignment. The first method consists in calculating the distances between the interaction position reconstructed via Anger logic and the identified position of the center of each pseudo-pixel. The interaction is then assigned to the pixel at the minimal distance.

The second method exploits the auxiliary position map shown in figure 3.24. The points composing the new map are calculated as the center of gravity between two neighboring pixels in the two directions (horizontal direction for the red points and vertical direction for the white ones). The column and row points at the minimal distance with respect to the reconstructed interaction position are then identified (and so also the interaction relative position with respect to these two points) and used to calculate the two external products explained in section 3.2.3.2; the sign of the two products uniquely define the pseudo-pixel where to assign the collected event. In figure 3.25a an example of the vectors employed for the calculations is presented together with the calculations logic. In figure 3.25b a scheme of the interaction position assignment to the pseudo-pixel is shown: a color has been given to each reconstructed point according to the pseudo-pixel region where it has been assigned by the described method. The method robustness is verified by the comparison of this map to the grid in figure 3.23b and 3.24

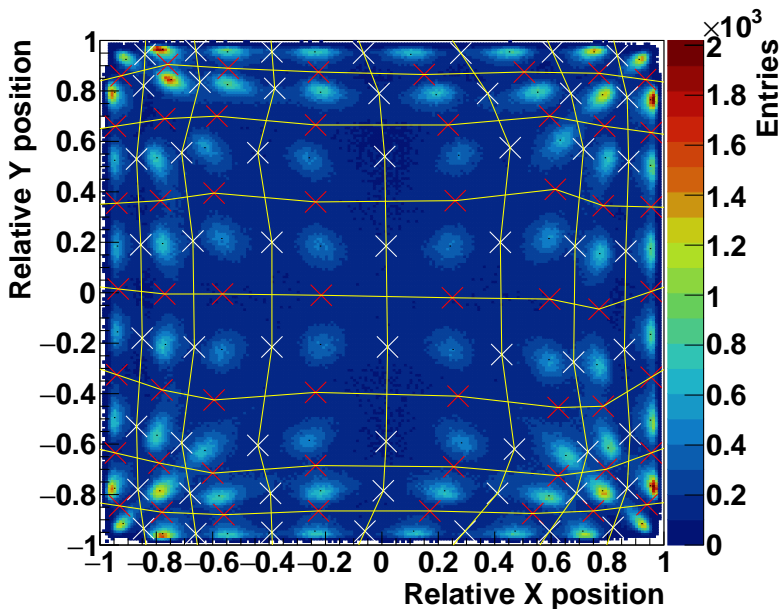


**Figure 3.24:** Auxiliary position map used for the assignment of the reconstructed events to a single pixel. The highlighted points represent the average distances between neighboring pixels on their separation borders.

In figure 3.26 the results of the pseudo-pixel energy calibration are shown. Figure 3.26a (left) shows the overlap of the energy spectra for the 64 pseudo-pixels before the energy calibration and equalization. The different response of each pixel to the two energy peaks is clearly visible. For each spectrum the low energy peak is assigned to 511 keV, while the high energy one to 1275 keV. In this way, the spectra are linearly calibrated and equalized, as shown in figure 3.26a (right).

Once the single pixel energy responses are equalized and calibrated, the whole block energy spectrum can be derived with the sum of the all pixels. In figure 3.26b (left) the ADC spectrum is shown before the equalization process, while in figure 3.26b (right) the calibrated energy spectrum is presented. In figure 3.26b (left) the energy spectra related to three reference position on the block surface are reported: this makes possible to appreciate the different contributions to the non-calibrated spectrum and the behavior of different block sections. The block peripheral pixels show an overall underestimation of the energy deposited, probably caused by a large amount of non completely absorbed events or by a not optimized scintillation light collection. The central pixels are affected by the expected fluctuations given by the streaked structure, but show a more consistent response.

The two spectra are represented in logarithmic scale in order to better appreciate the calibration effect: it allows to optimize the energy response on the two spectroscopic lines of the sodium source. At this stage, the energy resolutions of the block can be defined as the FWHM of the two energy peaks.

These results correspond to the pixel-assignment method based on the external product calculation, and no differences can be appreciated with respect to the one based on the minimal distance at the visual level. The analysis has been performed with the two methods for this reference block and the results are listed in table 3.1. In addition, the FWHM of the two peaks of the ADC spectrum before the calibration process are presented.

The results reported in table 3.1 show the need of the implemented calibration process, which

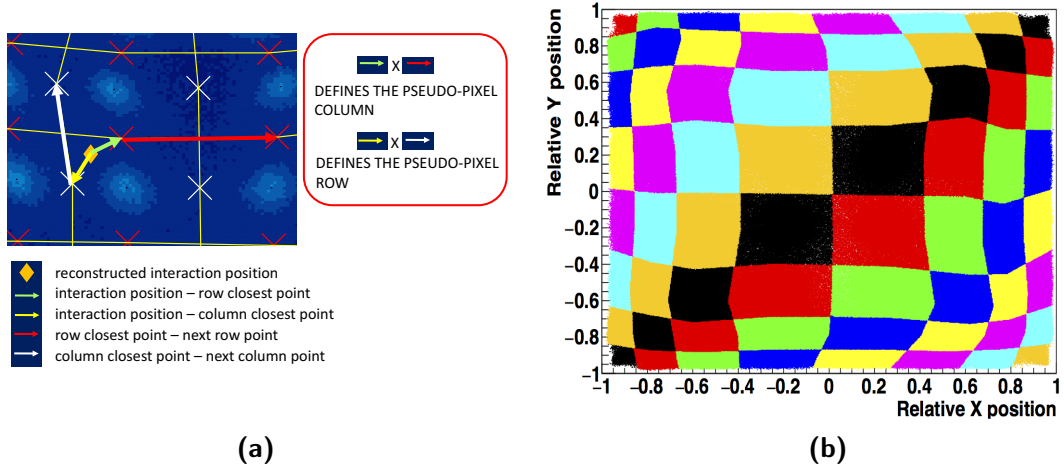


**Figure 3.25:** Logic for the event assignment to a single pixel (left) and 2D map of the resulting interaction assignment (right): each event is colored according to the chosen pseudo-pixel.

**Table 3.1:** Comparison of the results obtained with the two pixel-assignment methods.

Analysis Method	Energy resolution @ 511 keV FWHM [%]	Energy resolution @ 1275 keV FWHM [%]
Before equalization	46.12 [% ADC counts]	39.43 [% ADC counts]
Minimal distance	23.18	18.11
External products	23.03	18.04

allows to optimize the BGO block spatial and energy response. Concerning the two tested methods, the difference is of the order of 0.05 %. In the following the external product method is used because it appears to be more robust with respect to the basic approach implemented with the minimal distance calculation.

Thanks to the assignment of each reconstructed event to a single pseudo-pixel, the relative efficiency can be evaluated on a single pseudo-pixel basis. The two color maps in figure 3.27 show the number of events collected by the 64 pseudo-pixels during the sodium source homogeneous irradiation, with an energy selection performed on the two photons energy emitted by the source (511 keV events in figure 3.27a and 1275 keV events in figure 3.27b). The entries are normalized to the maximum number of entries in a pseudo-pixel, detected for a 511 keV energy selection.

Figures 3.27a and 3.27b show that the expected homogeneous distribution of events over the whole block surface is confirmed for the central pseudo-pixels of central lines (1 to 6), while the block borders present a factor 2-3 lower detection efficiency. In particular, the pseudo-pixels on the 4 corners (line 0 and 7, pseudo-pixels 0 and 7), have an efficiency of a factor between 5 and 6 lower with respect to the center of the block surface. This effect is partially due to geometrical factors, given the fact that the side pseudo-pixels are slightly smaller with respect to the central one (as also shown by the reconstructed 2D map in figure 3.23b). In addition to this, the light sharing mechanics and the light collection are probably less performing in case of photons interacting on the block borders. By comparing the two maps, a reduced efficiency for the detection of photons beyond 1 MeV is verified. This was expected given the previous application of the blocks, which were optimized for a PET system. In order to fully understand the relative and absolute efficiency of each block section, an irradiation with a collimated source scanning the whole active area is foreseen. This will allow one to precisely define the pixel limits and to estimate the detection rate variations on the detector active area.

#### 3.2.3.7 Time characterization

Figure 3.28 shows the distribution of arrival time differences between the reference BaF<sub>2</sub> detector and the tested BGO block. The time resolution is defined as the FWHM of this distribution.

#### 3.2.3.8 Results for the 30 blocks

In table 3.2 the results obtained for the calibration and characterization of a set of 10 blocks are listed. The characterized blocks shows very uniform results, with an average energy resolution of 25% FWHM at 511 keV and 20% FWHM at 1275 keV and an average time resolution of 4.42 ns FWHM tested with coincidences of 511 keV photons. Both the energy and time resolution are expected to be improved for the detection of photons in the prompt-gamma energy range, in particular above 1 MeV.

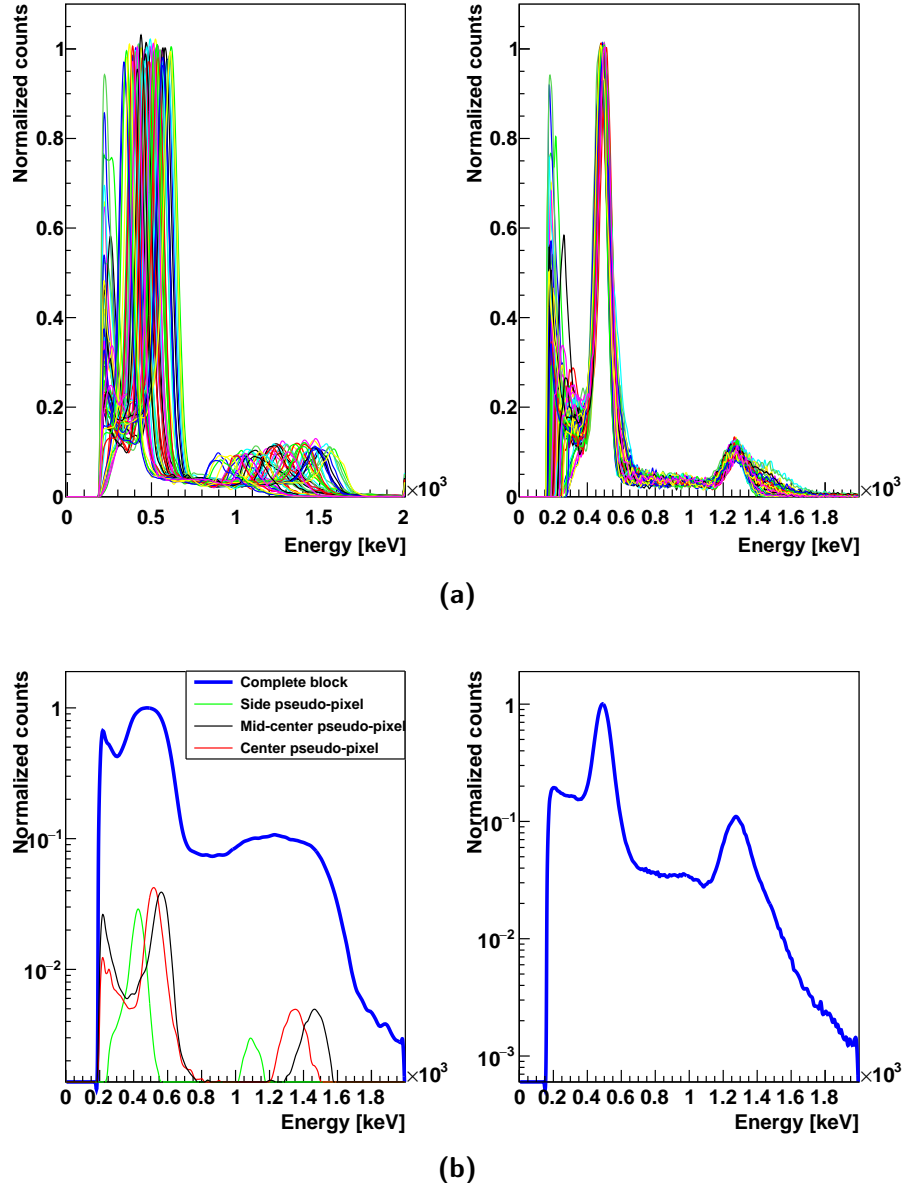


**Figure 3.26:** Single pseudo-pixels (a) and whole block (b) energy spectra before (left) and after (right) the calibration process. The whole block spectra are reported in logarithmic scale. Three non calibrated spectra of pixels in reference positions (border, mid-center and center area) on the block are also reported with the non calibrated spectrum.

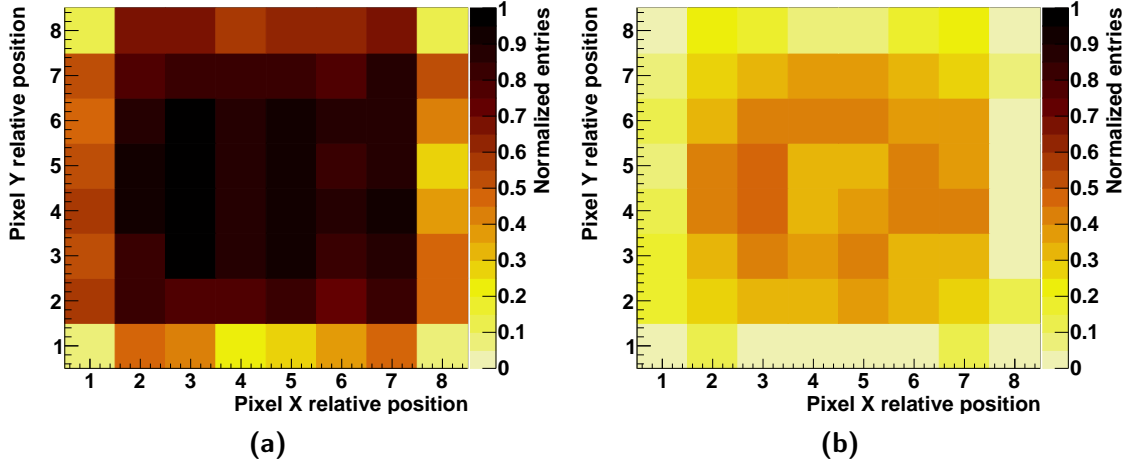


**Figure 3.27:** Relative number of entries for each pseudo-pixel as a function of the pixel relative position, represented by the row and column numbers (0 to 8 from left to right and bottom to top of the block surface). Figure (a) shows the entries in a selected energy window around 511 keV, figure (b) in an energy window around 1275 keV. All the entries are normalized to the maximum collected number of entries, corresponding to 511 keV events in the central section of the block.

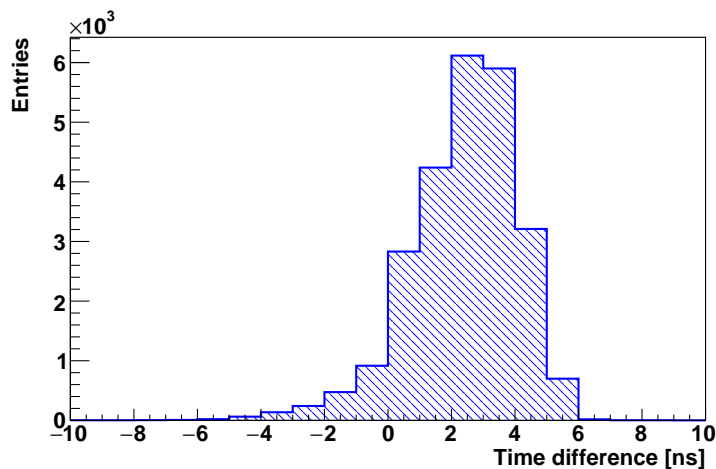


**Figure 3.28:** Distribution of arrival time differences between reference scintillator and BGO block.

**Table 3.2:** Calibration and characterization results for 10 tested BGO blocks.

BGO block ID	Energy resolution @ 511 keV FWHM [%]	Energy resolution @ 1275 keV FWHM [%]	Time resolution FWHM [ns]
<b>Ref. block</b>			
7627	23	18	4.0
3126			
3166	27	24	4.4
3171	23	18	
3184	24	20	4.3
3232	24	20	
3263			
3280	24	19	
3322	25	20	
3972			
4368	25	20	5.3
5243	25	19	
6823			
7130			
7218	25	21	
7240	25	20	
7258	26	19	4.9
7369	23	19	
7424	25	21	
7581	26	23	4.1
7586	26	24	
7601	24	19	4.1
7612	23	19	4.1
7651	24	20	3.9
7657	24	19	
14676	25	19	5.1
31210	25	21	
3375			1 pixel not found
3252			problem PM 0
7244			problem PM 2
21097			problem PM 2
7253			1 pixel not found
<b>Complete set</b>	$25 \pm 1$	$20 \pm 2$	$4.4 \pm 0.5$

### **3.3 Next steps and perspectives**

# 4

## Compton camera application for ion beam therapy monitoring



# 5

## Compton camera application in nuclear medicine

The results presented in this chapter have been published in (Fontana et al. 2017a) and (Fontana et al. 2017b).

### Contents

<b>5.1 Material and methods . . . . .</b>	<b>45</b>
5.1.1 Radioactive sources . . . . .	45
5.1.2 Compton camera simulation and data analysis . . . . .	45
5.1.3 Anger camera simulation and data analysis . . . . .	49
5.1.4 Figures of merit for the comparison study . . . . .	53
<b>5.2 Results: Compton camera study for SPECT application . . . . .</b>	<b>55</b>
5.2.1 Influence of Compton camera scatterer detector energy resolution . .	55
5.2.2 Compton camera coincidence study . . . . .	56
<b>5.3 Results: Benchmark of Compton camera and Anger camera performance . . . . .</b>	<b>57</b>
<b>5.4 Discussion . . . . .</b>	<b>59</b>

Single Photon Emission Computed Tomography (SPECT) is one of the most widespread techniques for nuclear medicine diagnostics examinations. In most of the clinical cases, a radiotracer is injected in the patient and the emitted  $\gamma$ -rays are collected by scintillating detectors coupled to physical collimation systems. This process leads to the reconstruction of a planar transmission image. Such a kind of imaging tool relies on the first idea proposed by Hal Anger ([Anger 1958, 1964](#)), and it is now commercially available in different variants with peculiar features and applications. A complete system is often composed of at least two rotating detection heads, allowing a tomographic data acquisition and the reconstruction of a three-dimensional image of the radiotracer distribution (see chapter 1 for further details).

The main consequence of the collimation system is a forced trade-off between sensitivity and spatial resolution: The spatial resolution is completely determined by the collimator geometry, and it can only be increased by reducing the collimator hole size, at the expense of a reduction in the detector sensitivity since fewer photons survive the mechanical selection. Moreover, the collimator thickness and septa limit the primary energy acceptance, and the performance of Anger cameras generally downgrades as energy increases.

In order to overcome this mechanical collimator limitation, it is natural to move towards an “electronic collimation”, where the emitted photons are tracked and the emission point is reconstructed via Compton kinematics, and so to the application of Compton cameras in this field ([Everett et al. 1977; Singh 1983](#)).

L. Han and colleagues ([Han et al. 2008](#)) have performed a simulation work comparing a standard Anger camera and a Compton camera prototype for a fixed source energy of 364 keV (iodine-131 gamma ray emission). The expected enhanced detection efficiency associated to the Compton camera with respect to the Anger system was estimated to a factor 20 at the tested energy, while the spatial resolution was compared for equal imaging time.

Starting from the results of Han and colleagues, we tested in simulation the performance of the CLaRyS Compton camera prototype (see chapter 3) for the application in SPECT. The aim of this simulation work consists in extending the aforementioned study to a wide energy range, with simplified analysis methods. The CLaRyS prototype is compared to the Infinia Anger camera delivered by General Electrics Healthcare ([GE Healthcare 2006](#)). The detector performances are compared in terms of efficiency and spatial response with the exposure to mono-energetic point-like radioactive sources at different energies, ranging from 245 keV to 2.614 MeV. The noise components related to the target (patient), such as photon attenuation, photon diffusion, patient movements, are common for both detectors and not considered in this context.

It should be noticed that the Compton detection principle requires coincidences between the two detector sections (scatterer and absorber), so that the random coincidence rate plays a fundamental role in the complete system performance, like in Positron Emission Tomography (PET) machines. The effect of these random coincidences will therefore be investigated. Moreover, a reliable Compton scattering cone reconstruction requires a precise energy resolution for the scatterer section of the detector. The influence of this parameter will be studied. Finally, the Doppler broadening effect will be quantified to give the physical limits of the Compton imaging technique knowing that silicon corresponds to the lowest  $Z$  material available for gamma detection with precise energy resolution. A comparison with a different possible scatterer material is also performed for verification.

All the obtained results are discussed with direct reference to (Han et al. 2008), focusing on the possible advantages offered by the use of a Compton camera (in particular the CLaRyS prototype), which intrinsically introduce the possibility to update the clinical standards in terms of source kinds, energies and activities, examination duration, patient dose, imaging techniques.

## **5.1 Material and methods**

In this section, the sources of gamma rays simulated for the study are presented and discussed and the two simulated systems are described in detail, as well as the proposed analysis techniques. In addition to this, some comments are given about the criteria chosen to represent a relevant comparison between the two investigated detectors.

### **5.1.1 Radioactive sources**

Both simulated systems have been exposed to monochromatic point-like gamma sources in air. The performance of the two cameras has been studied in terms of spatial resolution and detection efficiency as a function of the gamma source energy, related to actual radioemitters, already used in clinical practice or suggested for this kind of application in previous works (Nurdan et al. 2015). The explored energy range was chosen having in mind the possible clinical usage of Compton systems like the one developed by the CLaRyS collaboration, to extend the present field of application of SPECT imaging.

In table 5.1, the characteristics of the considered radioactive sources are given. Most of the sources do not emit gamma rays at a single energy, but only the ones selected for this study are presented in the table, together with the related branching ratio.

### **5.1.2 Compton camera simulation and data analysis**

#### **5.1.2.1 Simulation settings**

The simulation code for the Compton camera was developed with GEometry And Tracking 4 (GEANT4) v.9.6 and the camera design is based on the specifications of the prototype at present under development by the CLaRyS collaboration, detailed in chapter 3. It should be noticed that the real size of the detector components slightly differs from the ones reproduced in simulation, which have been used in the code for simplicity. The geometric setting of the camera has initially been optimized for the application in ion therapy monitoring via prompt-gamma emission and has been adapted for SPECT for this study in order to maximize the similarities between the two systems (Compton and Anger camera) in terms of detector acceptance, as detailed in the following. A SPECT specific optimization would depend on the choice of the particular gamma energy and it has not been studied yet.

**Table 5.1:** Radioactive sources used in the comparison study. Decay mode list: EC for electron capture,  $\beta-$  for electron emission,  $\beta+$  for positron emission, IT for isomeric transition. Half-life expressed in days (d), hours (h) or minutes (m). Data extracted using the National Nuclear Data Center On-Line Data Service from the Evaluated Nuclear Structure Data File database, file revised as of (2017-05-17) (Bhat 1992).

Isotope	Gamma energy [keV]	Branching ratio [%]	Decay mode	Half-life
Indium 111	245	94.1	EC	2.8 d
Iodine 131	364	81.5	$\beta-$	8 d
Yttrium 91m	555	95.0	IT	50 m
Bismuth 212	727	6.7	$\beta-$	60 m
Iodine 132	773	75.6	$\beta-$	2.3 h
Iron 59	1099 - 1292	56.5 - 43.2	$\beta-$	45 d
Zinc 65	1116	50.0	EC / $\beta+$	244 d
Calcium 47	1297	67.0	$\beta-$	4.5 d
Magnesium 28	1342	54.0	$\beta-$	21 h
Sodium 24	1368	100.0	$\beta-$	25 h
Potassium 42	1524	18.1	$\beta-$	12 h
Thallium 208	2614	99.8	$\beta-$	3 m

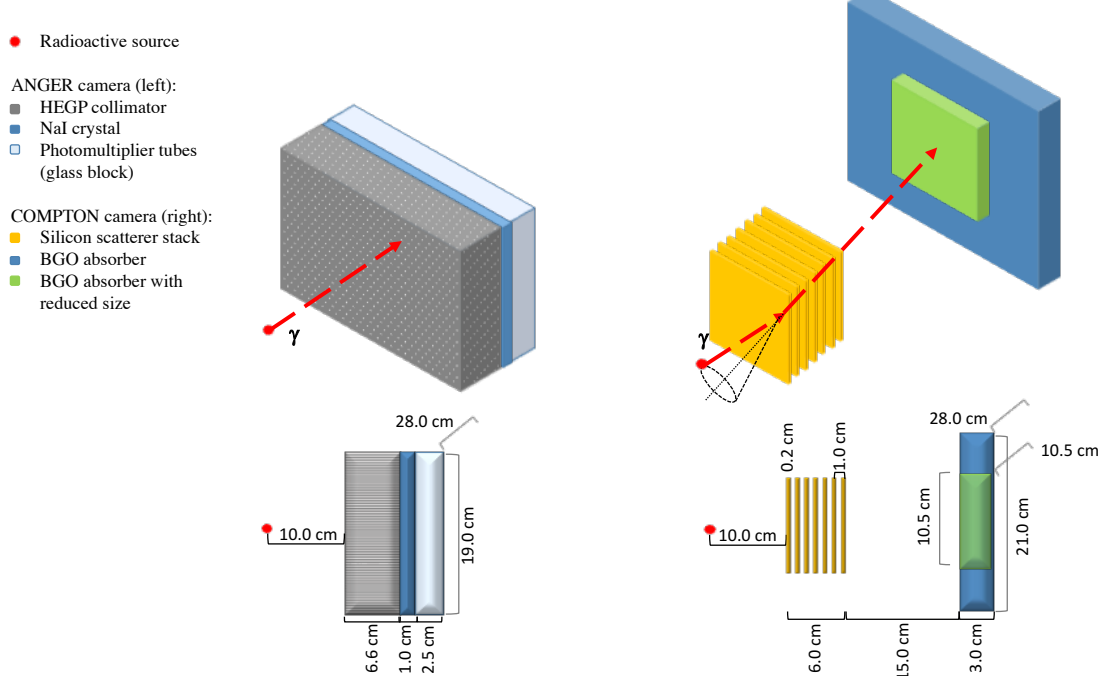


**Figure 5.1:** Sketch of the simulated geometry of the two systems: Anger camera (left) and Compton camera (right), in 3 dimensions (top line) and side projection (bottom line).

The distance between the last silicon plane (center) and the center of the absorber is set to 15 cm (see Figure ??). Moreover, the absorber size has been adapted to be as close as possible to the Anger camera detector, maintaining the real Bismuth Germanium Oxide - Bi<sub>12</sub>GeO<sub>20</sub> (BGO) block size. As a result, a matrix of 8×6 blocks has been arranged, for a total surface of 28×21 cm<sup>2</sup>. In the work of Han and colleagues ([Han et al. 2008](#)) a Philips camera was described in GATE as Anger system and the same NaI absorber detector was adapted for the simulation of the Compton system with the introduction of silicon pad detectors as scatterer part. The two geometries compared in this study are slightly different but the common absorber size strategy has been maintained.

The values for energy and spatial resolution of the silicon and BGO detectors used in the simulation were derived from the first tests performed on the detector prototypes (see chapter 3). For the silicon planes, the energy resolution is obtained from the Equivalent Noise Charge (ENC):

$$\sigma_E = W_{Si} \sqrt{ENC^2 + F_{Si} \frac{E_{dep}}{W_{Si}}}, \quad (5.1)$$

where  $F_{Si} = 0.115$  is the silicon Fano factor,  $E_{dep}$  is the energy released in the detector (in eV) and  $W_{Si}$  is the energy required to create an electron-hole pair in silicon (3.6 eV). The ENC strongly affects the detector performance and it will be analyzed in the following.

The spatial resolution was set according to the geometric parameters considering that the employed double-sided silicon strip detectors have a total of 64 strips per side, with a pitch of 1.4 mm. The position of each interaction is set in the center of the strip where it is recorded in both detection planes. Charge sharing on neighbor strips can in principle allow for sub-pitch resolution, but according to preliminary characterization measurements the probability of such a kind of events is less than 10%. The interaction depth is set as the center of the involved detector slab. The time resolution has been set to 20.0 ns Full Width at Half Maximum (FWHM) based on characterization measurements performed at the Grand Accelerateur National d'Ions Lourds (GANIL) accelerator in France.

The energy and timing resolution in the BGO blocks are set to 21% FWHM and 3.0 ns FWHM respectively, also based on characterization measurements performed with a cesium-137 source (662 keV gamma ray emission) and at the GANIL with prototype blocks. The spatial resolution, as for the silicon planes, is not experimentally measured yet and it is therefore fixed to the size of a single pixel. Each block surface is streaked with an 8×8 pixel matrix, 4.4 mm side, not reproduced in the simulation code. Each interaction is assigned to the center of the pixel where it is localized at the analysis stage, while the interaction depth is set at the center of the involved block.

### 5.1.2.2 Data collection and analysis

The radioactive source is placed at 10 cm from the first silicon detector, in the center of the scatterer stack transverse surface, and the number of simulated primaries is set to 10<sup>7</sup> gammas per energy step. To speed up the simulation, the primary gammas are emitted in a direction

within the acceptance cone defined by the first Compton camera silicon plane. All results are then normalized to the full solid angle.

All the events with at least one interaction in a silicon plane or at least one interaction in a BGO block are stored during the simulation process in two data sets, one per detector section. A small fraction of events presents interactions in more than one scatterer plane (< 1% at 245 keV) and/or in more than one BGO block (~8% at 245 keV). This kind of events leads to ambiguities in the cone reconstruction, because the cone vertex and axis are not univocally defined, and it is not treatable via List Mode-Maximum Likelihood Expectation Maximization (LM-MLEM) reconstruction. Alternative reconstruction algorithms (such as the one included in the Medium-Energy Gamma-ray Astronomy library (MEGAlib) ([Zoglauer et al. 2006](#))) are able to estimate the most likely scenario for multiple interactions, at the expense of larger uncertainties and longer calculation time. The multiple interactions events, representing approximately 8% of the total at 245 keV, are then refused in this study for simplicity. This choice reduces the detection efficiency, so that the value obtained in this work could be seen as the lower limit for this kind of detection system. Once the two lists of events are built, the time coincidences are defined according to the source activity, the detector geometry and the single detection section time resolution. Finally, the emission points are reconstructed with a LM-MLEM algorithm developed by the Centre de Recherche en Acquisition et Traitement de l'Image pour la Santé (CREATIS) institute in Lyon ([Lojacono et al. 2013](#)). The iterative algorithm reconstructs the Compton cones from the position and energy deposited in the scatterer stack and in the absorber blocks. A reconstruction volume must be defined, as well as a voxel 3 dimensional matrix in this volume. For this study the reconstruction volume has been fixed to  $5 \times 5 \times 5 \text{ cm}^3$  around the source, with a matrix of  $51 \times 51 \times 51$  voxels, and 15 algorithm iterations: this number is a compromise between reconstruction performance and calculation time.

### 5.1.2.3 Compton camera study for SPECT application

As already mentioned in the introduction, a critical parameter in the Compton camera performances is the scatterer detector energy resolution. The goal of the instrumental development is to obtain an energy resolution as close to 1 keV ( $\sigma_E$ ) as possible. The silicon detectors composing the stack have been tested at various temperatures in order to understand the behavior of the electronic noise and of the leakage current, and the read-out electronics is being developed with the aim to reduce the electronic noise. The first laboratory tests showed an energy resolution at 25C of approximately 10-15 keV FWHM with a first read-out card prototype. The new card has been tested with simulated signals and gives a noise level closer to the expectations. No data are yet available to determine the detector energy resolution at different temperatures and with the final card version. In the simulation two different resolutions have been considered in order to verify the influence of this parameter on the final reconstructed image. The two chosen values are  $\sigma_E = 2 \text{ keV}$  and  $\sigma_E = 4 \text{ keV}$ , corresponding to about 5 keV and 9.5 keV FWHM, respectively, both calculated at 200 keV of released energy using equation 5.1. The influence of Doppler broadening has also been studied by disabling the Doppler effect in the simulation with the energy resolution set to  $\sigma_E = 2 \text{ keV}$ . Finally, a different possible scatterer material, Cadmium Telluride (CdTe), has been tested at the same resolution in order to verify the expected advantage given by the choice of silicon.

A coincidence study is mandatory to define the source activity to be used in the simulations

dedicated to the benchmark with the Anger camera. Timing information is not included in the simulation code and a time structure must be assigned to the simulated primaries in the data analysis stage. A reference time is chosen randomly from an uniform distribution between 0 s and the data acquisition time and assigned to a primary photon. The data acquisition time ( $T_{DAQ}$ ) is calculated as the expected time needed for the emission of the desired number of primaries ( $N_{primaries}$ ) according to the source activity  $A_{source}$ :

$$T_{DAQ} = \frac{N_{primaries}}{A_{source}}. \quad (5.2)$$

The source activity is not fixed at the simulation stage but only during data analysis afterwards. It can therefore be easily modified to perform a study of the camera performance with different kinds of sources. The scatterer and absorber interaction times are calculated with respect to the reference primary emission and included in the related data sets for the analysis.

Two sets of data are produced as output of this analysis, one for the scatterer and one for the absorber: Each element in the two sets corresponds to an interaction in the detector and includes the interaction 3 dimensional position, energy released, time with respect to the total data acquisition time and primary reference index provided by the simulation. The elements in the two data lists are ordered for increasing time. The detectors time resolution specified in section 5.1.2 and a time window set to 20 ns, corresponding to a  $3\sigma$  acceptance are then used for the coincidence definition for different source activities. The time of each element in the absorber data set is compared to the time of the elements in the scatterer data set. A coincidence is defined when the scatterer event time is within the time window centered in the absorber event time. Each element is used one time only, and the analysis continues until the end of the absorber data list. If the two elements (one from the scatterer data set and one from the absorber one) forming a coincidence have the same reference index, they correspond to interactions of the same primary photons and the coincidence is then a true one. If the reference index is different for the two elements, the coincidence is random. The number of true and random coincidences has been studied as a function of the source activity in a range of clinical interest between 1 MBq and 500 MBq, for a fixed energy value of 555 keV. The variation of the influence of random coincidences as a function of the energy was also investigated at a fixed source activity of 200 MBq.

The scatterer energy resolution and the source activity have been fixed for the benchmark study. The choice of their values is discussed in section 5.2.

### 5.1.3 Anger camera simulation and data analysis

#### 5.1.3.1 Simulation settings

The Anger camera system is simulated with GEANT4 Application for Tomographic Emission (GATE) v.7.1 and it is based on the General Electrics Healthcare Infinia SPECT system ([GE Healthcare 2006](#)), a commercial clinical camera with parallel hole collimator and Sodium Iodide doped with Thallium (NaI(Tl)) scintillator. A single detection head is simulated in order to obtain a direct performance comparison to the Compton system.

The chosen configuration includes a High Energy General Purpose (HEGP) lead collimator, 6.6 cm thick, with a surface of  $28 \times 19 \text{ cm}^2$  (see Figure 5.1). The parallel hole grid is composed of hexagonal shaped holes, 0.2 cm radius, arranged in a quincunx structure, with a septal thickness of 1.8 mm. This collimator is optimized for energies below 364 keV, corresponding to the main gamma emission energy of iodine-131. The NaI(Tl) crystal is simulated as a single block of  $28 \times 19 \times 1 \text{ cm}^3$ , in contact with the collimator back surface and read out by photo-multiplier tubes. The photo-multiplier grid is represented with a glass block of 2.5 cm thickness behind the crystal, with the same transverse surface (see Figure 5.1). The spatial and energy resolutions have been set according to the manufacturer specifications. Unless otherwise stated, their values correspond to one standard deviation. A lower detected energy threshold has been set to 80 keV.

The source is placed at 10 cm distance from the collimator surface (the distance chosen in the Infinia data sheet), and its transverse position corresponds to the center of the central collimator hole. For each source energy,  $10^8$  primary photons are simulated in  $4\pi$ . An event corresponds to single or multiple interaction of a photon (or secondary particle produced by the photon interaction in the collimator) in the NaI(Tl) crystal. All the detected interactions are computed and the gamma interaction position is calculated during the simulation as the center of gravity of the positions of all the hits (energy transfers of secondary electrons), with the deposited energy as weight for the calculation. The deposited energy corresponds to the sum of the energies released during each hit. A set of interaction points and energy deposited is then stored.

### 5.1.3.2 Data analysis

Four source primary energies have been chosen as references of the studied energy range and are used in the following to show the analysis method and the study results. The low energy range is represented by the indium-111 emission at 245 keV, the first energy above the Anger camera construction limit has been set to 555 keV (yttrium-91m), while iron-59 at 1099 keV and potassium-42 at 1524 keV have been chosen to represent the medium and high energy range respectively.

Figure 5.2 presents the raw radial event distributions for the four reference energies. Each distribution bin content is normalized according to the surface of the circular region corresponding to each radius. The first distribution bin always corresponds to the radius of the central collimator hole, with the partial inclusion of the surrounding septa. This choice is determined by the detector and collimator geometry and by the source position. It is possible to list three different kinds of events contributing to the radial distributions:

1. photons passing through the collimators holes without interactions,
2. photons traversing the collimator septa without interactions,
3. photons interacting in the collimator septa.

Only the first listed contribution transports true spatial information about the source location, and these photons generate the signal. All other kinds of events contribute to the background, which rapidly increases with the primary photon energy.

A background rejection is performed in order to extract the distribution corresponding to the signal. The complex background contribution cannot be determined analytically, we therefore approximated the background profile as a linear fit to the tail of the radial distribution. The fit limits have been defined as follows:

- the lower limit is calculated as the radial distance where the photon flux on the NaI(Tl) detector is reduced to a fraction  $\frac{1}{e}$  by absorption effect in the collimator septa;
- the upper limit has been fixed to the half of the collimator smaller lateral side (95 mm), in order to avoid any kind of geometric effect due the binning choice or the normalization surface selection. The bin size creates artifacts in the radial distribution corresponding to the collimator limits, because three different geometries are involved: the circular surface covered by each distribution bin, the hexagonal shape of the collimator holes and the rectangular collimator geometry.

The estimated background profile is subtracted from the raw distribution and the result is used as reference of the image signal (figure 5.2).

Two validation tests have been performed in order to check this analysis method. First, according to the geometry of the collimator and to the mass attenuation coefficient of NaI(Tl) ([Hubbell et al. 1987](#)), we evaluated the expected number of entries in the first distribution bin (before normalization), corresponding to the central collimator hole in front of the source. The calculation is performed with the attenuation law of photons in 1 cm of NaI(Tl). A dedicated set of simulations has been performed equivalent to the ones for the Anger camera described in section 5.1.3.1, but using an ideal detector and a reduced number of photons of  $10^7$ . No uncertainties are applied on the position of photon interactions to avoid resolution effects and the background is estimated via a linear fit as described above. The obtained entries in the first distribution bin after the fit selection are compared to the ones obtained with the theoretical calculation. In figure 5.3 the results are shown as a function of the source energy.

There is a good agreement between the values calculated with the attenuation law and the simulation data selected with the fit-based background subtraction, and the detected variations from the ideal trend are within the statistical fluctuations. A slight overall effect of under-detection is observed (about 10% on average), while the single value at 245 keV shows an opposite behavior (with a difference of less than 20%). This is related to the chosen fit function.

As a second validation, an additional set of simulations has been performed with the same settings as defined in section 5.1.3.1 but with an infinitely dense collimator. The raw radial distributions obtained with this set of simulation is compared to the radial distribution 'derived' by the simulations with nominal settings after the application of the fit-based background subtraction. The results are shown in figure 5.4.

It can be noticed that the distribution overall trend is reproduced by the fit-based background rejection method, the main source of difference being probably the contribution of the scattering in the hole grid surrounding the central one.

The linear fit appears to be a robust way to select the signal transporting spatial information

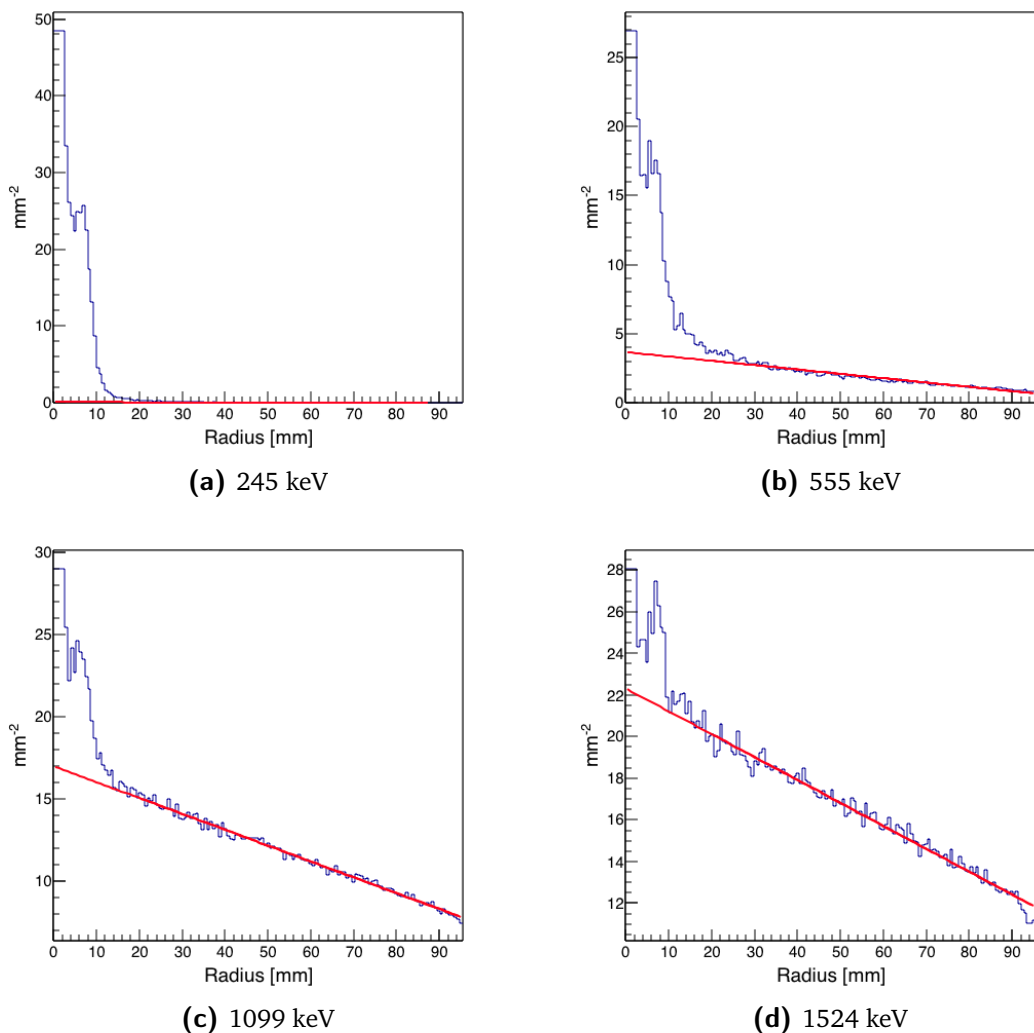


**Figure 5.2:** Radial event distribution normalized by the circular surface corresponding to each bin for 4 representative source energies, with the linear fit performed for background rejection. The total number of simulated primaries for each data set is  $10^8$ .

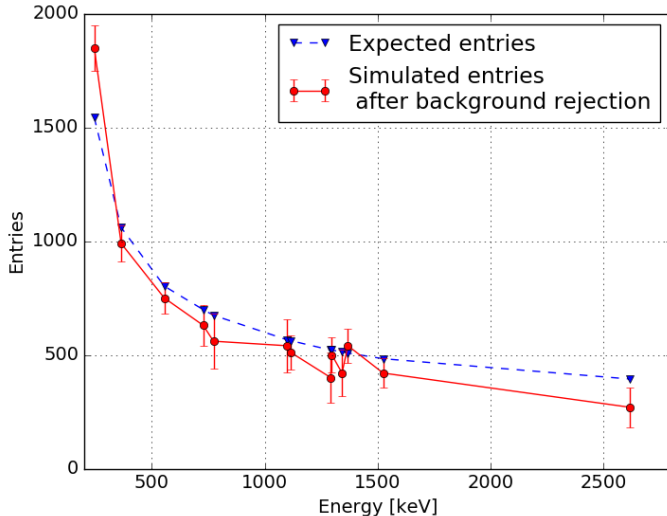


**Figure 5.3:** Comparison between expected entries in the central collimator hole (blue dashed curve) calculated according to pure geometrical factors and detector interaction cross section and simulated detected entries after background rejection (red solid curve) with null spatial resolution (ideal detector) to avoid resolution effects and lower energy threshold set to 80 keV.

from the source and is applied with no modification for the entire energy range, giving to the analysis method the desired consistency.

#### 5.1.4 Figures of merit for the comparison study

The two cameras are studied and compared according to three figures of merit which refer to their main detection parameters: spatial resolution, detection efficiency, and signal-to-background ratio. The definition of these three values must be adapted to the two detectors, keeping in mind their differences: on one side the Anger camera provides a transmission image through a mechanical collimator, with no need for a reconstruction process and with a single detector component; on the other side, the Compton camera relies on event time-coincidences and needs a reconstruction algorithm to obtain the final spatial distribution.

In this study, the imaging process of a point source was simulated. The three figures of merit are therefore evaluated based on the radial event distribution, in order to profit of the radial symmetry of the simulated system.

For the Compton camera, the standard deviation of the radial distribution is used to express the detector spatial resolution, the detection efficiency is defined as the ratio between MLEM reconstructed events and total simulated primaries, and the signal-to-background ratio corresponds to the ratio between the number of reconstructed events and the total number of coincidences selected before the reconstruction with the coincidence analysis.

For the Anger camera, it is difficult to define the spatial resolution, as shown in (Cecchin et al. 2015). Here, we use the standard deviation of the signal radial distribution in order to be consistent with the Compton camera definition already proposed (the “signal” substantive

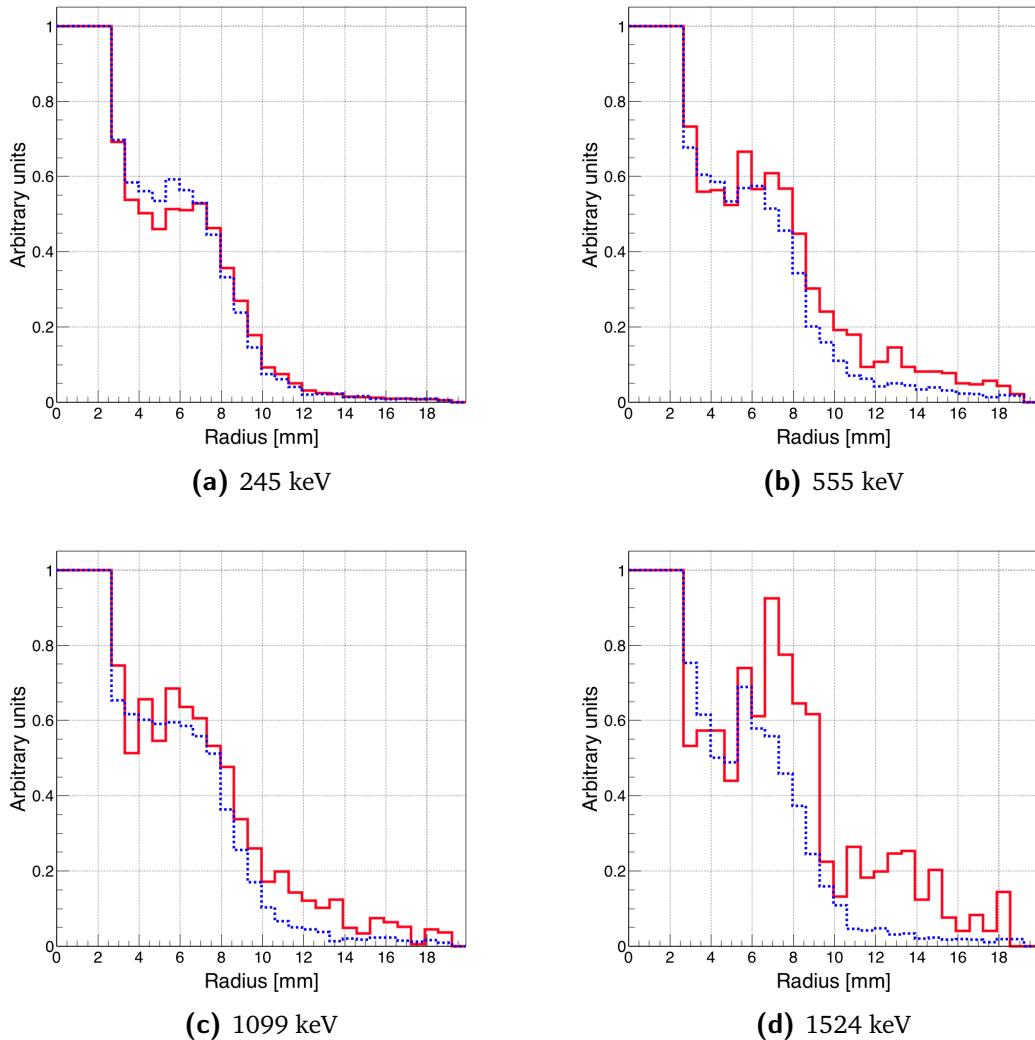


**Figure 5.4:** Normalized radial distribution with background rejection (red solid lines) compared to normalized radial distribution for infinite density collimator (blue dashed lines).



**Figure 5.5:** Reconstructed radial distribution standard deviation as a function of the source energy. Two energy resolution values are set to the silicon detectors ( $\sigma_E = 2$  keV - red dots solid line - and  $\sigma_E = 4$  keV - blue dots dashed line), the Doppler broadening effect has been removed (green horizontal triangles dashed line) and the scatterer material has been changed with CdTe solid state detectors (black vertical triangles dashed line), for a fixed energy resolution of  $\sigma_E = 2$  keV.

means entries after background rejection). The detection efficiency is defined as the ratio between the number of signal events and the total number of simulated primaries. Finally, the signal-to-background ratio is evaluated as the ratio between the signal events (the entries in the radial distribution after the fit-based background rejection) and the total number of events recorded by the detector (the entries in the raw radial distribution).

## 5.2 Results: Compton camera study for SPECT application

The results of the characterization of the CLaRyS Compton camera prototype for the application in SPECT are presented in the following sections, dedicated to the study of the scatterer detector energy resolution and of the Doppler broadening effect, and to the analysis of the rate of random coincidences, respectively.

### 5.2.1 Influence of Compton camera scatterer detector energy resolution

Figure 5.5 shows the standard deviation of the radial distribution obtained after the MLEM reconstruction (see section 5.1.2.2) as a function of the source energy for the two different analyzed noise levels (Electron Noise Charge - ENC = 500 e<sup>-</sup>, corresponding to  $\sigma_E = 2$  keV, and ENC = 1100 e<sup>-</sup>, corresponding to  $\sigma_E = 4$  keV). The maximum detected difference is about 35%, but the influence of the silicon detectors' energy resolution rapidly reduces at increasing energy. In the same figure, the results for the simulation without the Doppler broadening for the lowest energy resolution are shown. It is clear that this parameter has a strong influence for the Compton camera spatial resolution, at least for energies below 2.5 MeV. This result justifies the choice of silicon as scatterer material, because it is the lowest Z available detector and therefore minimizes the Doppler contribution. This is underlined by the black curve corresponding to a Cadmium Telluride (CdTe) detector, i.e. a higher Z material than silicon. For this last study, the electronic noise level has been set for CdTe in order to have the same intrinsic resolution as for silicon ( $\sigma_E = 2$  keV obtained with equation 5.1).

For the benchmark with the Anger camera, the ENC value of the Compton camera scatterer

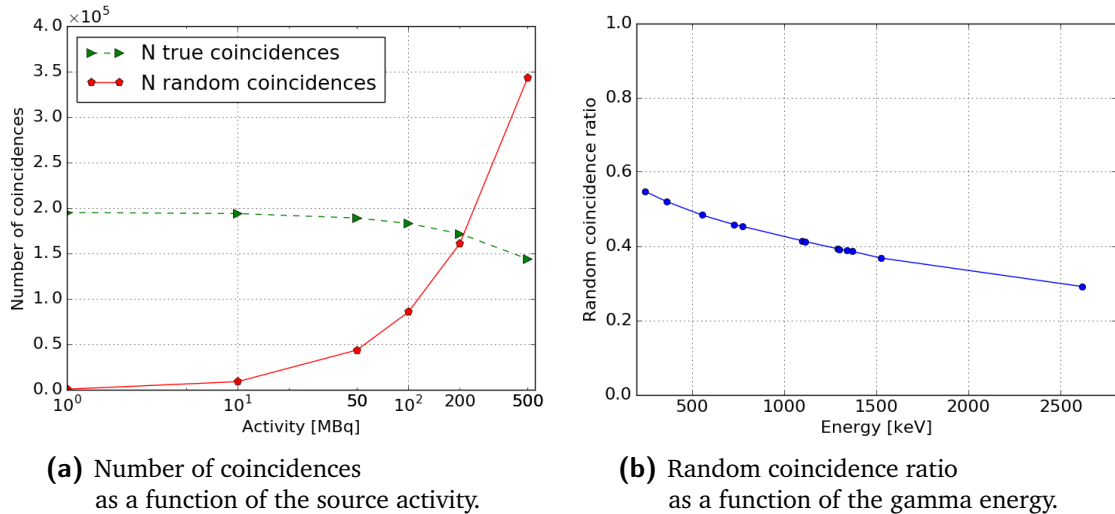


**Figure 5.6:** (a): number of true (green) and random (red) coincidences as a function of the source activity in the range 1-500 MBq, for the reference energy of 555 keV. (b): Percentage of random coincidences as a function of the source energy, with a fixed source activity of 200 MBq. Compton camera parameters: time resolution FWHM of 20 ns for silicon detectors, 3 ns for BGO and a coincidence window of 40 ns. The source branching ratio has been set to 100% for all sources for simplicity in the comparison of results.

components has been fixed to  $500 \text{ e}^-$ , which corresponds to the expected level of noise affecting the silicon detectors at about 0C (the silicon detectors are cooled down with a thermal-controlled box) and with the final acquisition card (about  $2 \text{ keV } \sigma_E$ ). This value has to be experimentally verified.

### 5.2.2 Compton camera coincidence study

Figure 5.6 (left) shows the numbers of true and random coincidences as a function of the source activity, ranging between 1 and 500 MBq in order to explore the whole range potentially employed in real examinations. The energy is set to 555 keV.

At 200 MBq source activity, the same amount of true and random coincidences is observed at 555 keV gamma energy. With activities above this value, the ratio between true and random coincidences is less than one. In principle the reconstruction LM-MLEM program can partially reject this kind of events and if we consider the expected important increase in detection efficiency guaranteed by the “electronic collimation”, it results clearly that it is not worth to employ high activity sources (or that a smaller camera can be considered at the expense of the examination time).

For the further analysis and the final detector comparison, the source activity has been then set to 200 MBq, and the number of random coincidences is studied as a function of the source energy. Figure 5.6 (right) shows the ratio of detected random coincidences over the total number of reconstructed coincidences (see Section 5.1.2.2) as a function of energy for a fixed activity of 200 MBq. The ratio decreases for increasing energies, because the product of independent interaction probabilities in two detectors decreases faster than the true coincidence one. Therefore, an increasing reconstruction efficiency with MLEM is verified (see Section 5.3).

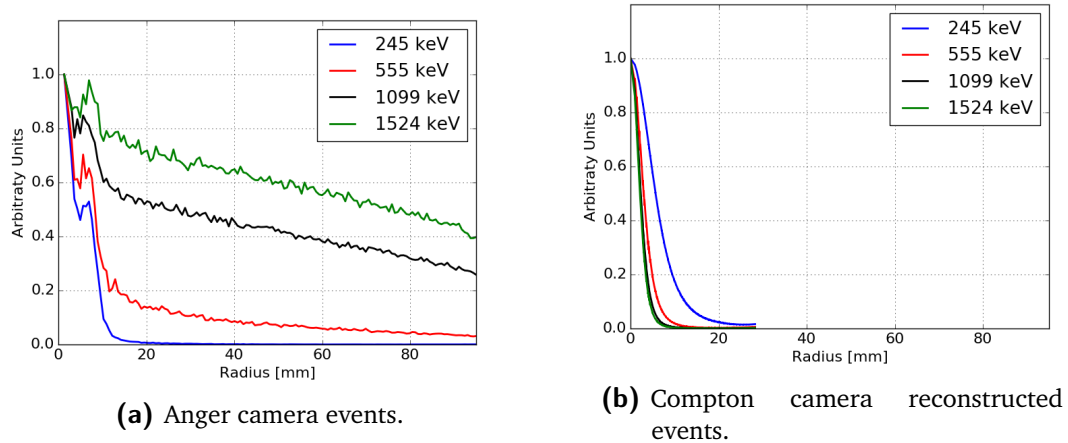


**Figure 5.7:** Overlap of the normalized radial distributions for 4 selected source energies.

### 5.3 Results: Benchmark of Compton camera and Anger camera performance

The analysis methods presented in section 5.1.2.2 and section 5.1.3.2 for the Compton and Anger camera, respectively, have been applied to the simulated data sets of the two cameras at all energies.

The radial distributions for Anger and Compton camera at the different reference source energies and a source activity of 200 MBq are shown in figure 5.7. The same reference energies selected in section 5.1.3.2 are included here. The radial range is limited to the smaller collimator lateral size (95 mm), according to the fit limits imposed on the Anger camera data (see Section 5.1.3.2). The curves are normalized to 1 for an easier visual comparison.

In figures 5.8, 5.9, and 5.10, the detection efficiency, the radial distribution standard deviation and the signal-over-noise ratio are respectively shown as a function of the source energy for the two sets of data. Uncertainties (1 standard deviation) are reported for all the values and included in the data points when not visible.

From figure 5.8 one can point out the advantage provided by the absence of a physical collimation system in terms of detector efficiency. It should be noticed that two different scales are applied to figure 5.8 in order to show the two plots on the same figure and appreciate the variations with respect to the energy. The detection efficiency of the Compton camera is always more than a factor 20 higher than the one of the Anger camera. Although the images of the Anger and Compton cameras are based on different kinds of spatial information (a line and a cone, respectively), the Compton camera efficiency should allow a substantial reduction of the injected source activity and/or of the acquisition time. The efficiency of both cameras constantly decreases with increasing energy, because of the decreasing photon interaction probability. The only exception is found at the lowest considered energy of 245 keV in the Compton camera, due to an increased probability of photon absorption in the scatterer and, in parallel, a larger fraction of events with wide Compton scattering angles at low gamma energy.

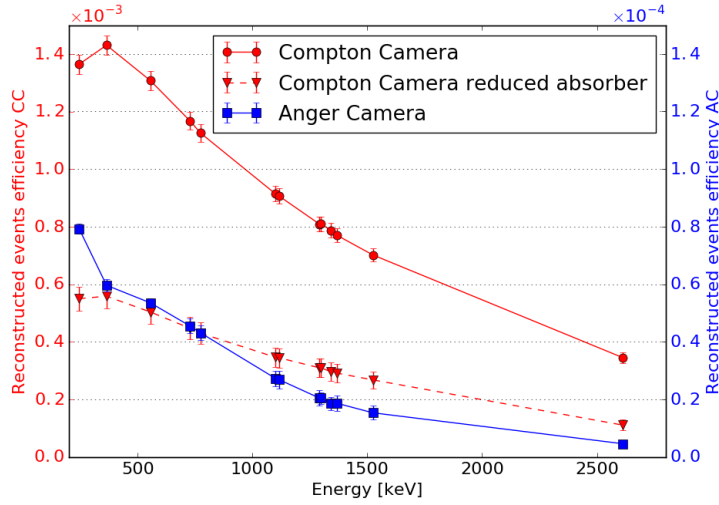


**Figure 5.8:** Detection efficiency as a function of the source energy. Source activity = 200 MBq, Compton camera silicon detector  $\sigma_E = 2\text{ keV}$ .

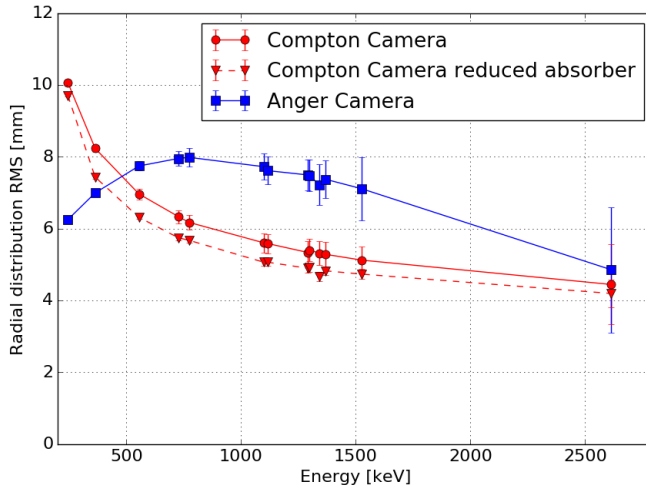


**Figure 5.9:** Standard deviation of the radial event distributions as a function of the source energy. Source activity = 200 MBq, Compton camera silicon detector  $\sigma_E = 2\text{ keV}$ .

The standard deviation of the radial distribution, shown in figure 5.9, confirms the optimization of the chosen collimator for the Anger camera for low energies (below 364 keV). With the ad-hoc background subtraction operated here, which is not realistic for an extended source, the Anger camera outperforms the Compton one in terms of spatial resolution at low energies (by  $> 3\text{ mm}$  at 245 keV and about  $1.3\text{ mm}$  at 364 keV). However, above 500 keV, the Compton camera can provide a better spatial resolution with a difference ranging between a fraction of millimeter up to about 2 mm. For energies above 1.5 MeV, the two curves of standard deviation for the two cameras reach similar values ( $< 0.5\text{ mm}$  difference at 2614 keV), but figure 5.10 shows how the background rejection for the Anger camera and the MLEM reconstruction for the Compton system (see Sections 5.1.3.2 and 5.1.2.2) affect this result. Above 364 keV, the selection for the background rejection of the Anger camera data drastically reduces the number of events contributing to the final image (the ratio between selected and detected events approaches zero). With an extreme selection, at very high energy the only events contributing

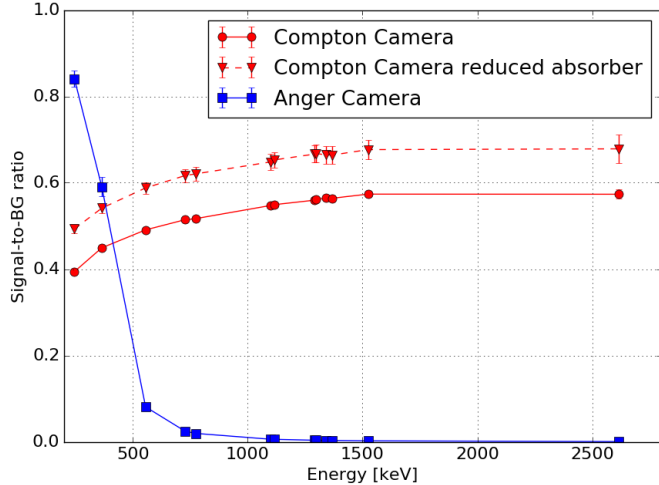


**Figure 5.10:** Signal-to-background ratio as a function of the source energy. Source activity = 200 MBq, Compton camera silicon detector  $\sigma_E = 2\text{ keV}$ .

to the final image are the events traversing the central hole of the collimator, resulting in an enhanced spatial resolution (see Figure 5.4d). The signal-to-background ratio of the Compton camera confirms the expectations concerning the reconstruction algorithm performance: if compared to Figure 5.6 (right), the curve in Figure 5.10 shows how the rejected events correspond approximately to the amount of random coincidences.

## 5.4 Discussion

The Compton camera under development by the CLaRyS collaboration is now at the characterization stage. Originally designed and optimized for the application in ion beam therapy monitoring for the detection of prompt-gamma rays in a wide energy range (between some hundreds of keV until about 10 MeV), it is here studied as SPECT detector in comparison to a commercial system based on the Anger gamma camera design.

The expected significant enhancement in terms of detection efficiency, for comparable imaging performance in terms of spatial accuracy, has been already proven in simulation in (Han et al. 2008) with a silicon-sodium iodide based Compton camera prototype at a single primary energy of 364 keV. A factor 20 efficiency gain has been reported.

First of all, the present work aimed to extend these results by testing the two detectors at increasing primary gamma energies, ranging from 245 keV to 2614 keV. A common analysis method has been defined in order to obtain comparable results, always keeping as reference the final image. The results were directly compared in terms of detection efficiency, spatial resolution (standard deviation of the radial event distribution) and event selection (background rejection for the Anger camera and Maximum Likelihood Expectation Maximization - MLEM - algorithm selection for the Compton camera) via the definition of three figures of merit.

A preliminary study has been performed on the simulated Compton camera data in order to fix

the main parameters of the camera simulations, namely the energy resolution of the silicon scatterer detectors and the source activity determining the coincidence rate. Two Electron Noise Charge values have been studied, resulting in a maximum difference in spatial resolution of 35% at the lowest energies, rapidly decreasing at increasing primary energy. A value of  $\text{ENC} = 500 \text{ e}^-$  has been chosen as the closest to the instrumental development expectations and first tests. The influence of the Doppler broadening on the spatial resolution has been also estimated in a factor  $\sim 1/3$  at 500 keV, then reduced up to  $\sim 0$  at 2.5 MeV of primary gamma energy, with fixed energy resolution ( $\sigma_E = 2 \text{ keV}$  -  $\text{ENC} = 500 \text{ e}^-$ ) in the silicon detectors. Moving to the coincidence rate analysis, at the reference energy of 555 keV and with detector time resolution set according to first characterization results, the simulated data have been analyzed by reproducing a source activity in the range 1-500 MBq. The result shows the expected increase in the random coincidence rate at increasing source activity, with a ratio between true and random coincidences close to one at 200 MBq. This value has been chosen as clinical reference for the comparison analysis.

The results discussed in section 5.3 confirm the conclusion of Han et al. about the advantage given by the usage of a Compton system and show how the gain factor in the detector efficiency is maintained at increasing energy. Concerning the detector spatial resolution, the Compton camera outperforms the Anger system at energies above about 500 keV. The Anger camera spatial resolution can be boosted by aggressive background subtraction in the considered case (point-like source image), at the expense of a drastic signal suppression. However, this approach is not reproducible and exploitable in actual clinical conditions and the obtained results are not comparable to the Compton camera performance at the same energy.

The results of this work clearly show the potential of the Compton camera for the application in nuclear medicine examination, opening new possibilities for the clinical implementation. The studied detector has originally been designed and optimized for another application, and it has only been adapted for SPECT here, but not yet optimized in terms of detector geometry (size, position, and inter-detector distances). For an optimized detector, performance is therefore expected to be improved with respect to the presented results. In future development, the reconstruction MLEM algorithm should be adapted to this application and the reconstruction parameters should be studied to further enhance the final performance, in particular for what concerns random coincidence rejection.

Anyway, these first evidences already allow one to investigate the possible modifications introduced by the clinical set of Compton detection systems. The enhanced detection efficiency in parallel with comparable spatial performances paves the way to the diffused usage of less active sources, or alternatively allows a substantial reduction of examination time: as a result, the dose delivered to the patient would be reduced. On the other side, the possible introduction of sources with higher primary emission energy will reduce the effect of photon attenuation in the patient (not studied in this simulation work), improving by definition the spatial information and further reducing the effective dose delivered to the patient. Simple analytic calculations can show how a photon attenuation of about 66% is foreseen for 364 keV photons in 10 cm of water, while the effect is reduced, for example, to 49 % at photon energy of 1099 keV (Hubbell et al. 1987). Higher energies can be employed also with Anger cameras, at the expense of introducing thicker collimators with reduced holes size, with the result of a reduced efficiency with respect to the analyzed High Energy General Purpose collimator. Furthermore, a possible implementation of Compton cameras is also foreseen for targeted radionuclide therapy, where the radionuclides used in clinics often have gamma radi-

ation emission at relatively high energy. This signal is difficult to be detected and treated with conventional SPECT cameras, while the Compton detection technique could make it quantitatively exploitable in clinical practice, for both pre- and per- treatment images.

Even though Compton cameras intrinsically lead to 3 dimensional images with a single detector head, the spatial resolution associated to the direction normal to the detector planes has to be more deeply studied, but this feature is an additional point in favor of the introduction of Compton systems in the clinical environment, moving beyond the tomographic concept and towards more compact detector solutions. Several studies are ongoing in order to improve the image reconstruction algorithms and, so, the 3 dimensional imaging performance (Kuchment et al. 2016). Different detection approaches can also, in principle, lead to improved image quality in 3 dimensions, such as the Compton electron tracking (Kabuki et al. 2007; Sonoda et al. 2015). Moreover, a further enhancement in image reconstruction should be given by the measurement of the photon depth of interaction: the photon is assumed to interact in the center of the detector components for our prototype, while perpendicularly segmented detectors can ensure an improved resolution in the third dimension and a resulting enhanced reconstruction accuracy, also involving better 3 dimensional imaging capabilities.

The advantages of the Compton detection principle are here shown thanks to a first detector prototype, but there is still wide room for improvement.

Once the CLaRyS Compton camera will be completed and characterized, tests in clinical environment are foreseen in the field of medical imaging. The actual potential of such a kind of detector will be then quantified with experimental data.



# 6

## Beam tests

### Contents

6.1	Hodoscope: december 2017	64
6.2	Hodoscope: may 2018	64
6.3	Collimated camera: august 2018	64
6.4	Collimated camera: september 2018	64

**6.1 Hodoscope: december 2017**

**6.2 Hodoscope: may 2018**

**6.3 Collimated camera: august 2018**

**6.4 Collimated camera: september 2018**

# 7

## Conclusions and discussion



# A

## Compton camera data format

### A.1 Introduction

This document aims to formalize and fix the Compton camera data format. The structure of the data sent by each detector section (scatterer, absorber and beam hodoscope) to the acquisition card is detailed, as well as the structure of the events sent to the acquisition PC.

### A.2 General features

#### A.2.1 Common information

The detector Front End cards are connected to the  $\mu$ -TCA via optical links, with a speed of 3.0 Gbit/s. The transfer frequency is 150 MHz.

All the Front End card TDCs share the same synchronized clock, at a 40 MHz frequency, which is sent to the cards through an external link.

Every data packet sent to the  $\mu$ -TCA by the Front End cards starts with the following information:

- N° Front End (8 bits);
- N° Trigger (24 bits);
- N° Mode (8 bits);
- N° of element in the packet (8 bits).

##### A.2.1.1 Front End number

The Front End number is the identification code of each Front End card. A mechanical switch on the card defines the ID which is sent in the data packet header.

In Table ?? the Front End number IDs are listed with the corresponding cards.

**Table A.1:** Front End number associated to each Front End card.

FE number	FE card
0	All detectors
1	Silicon 1
2	Silicon 2
3	Silicon 3
4	Silicon 4
5	Silicon 5
6	Silicon 6
7	Silicon 7
8	Silicon 8
9	Silicon 9
10	Silicon 10
11	ASM 1
12	ASM 2
13	ASM 3
14	ASM 4
15	ASM 5
16	ASM 6
17	ASM 7
18	ASM 8
19	ASM 9
20	ASM 10
21	ASM 11
22	ASM 12
23	ASM 13
24	ASM 14
25	ASM 15
26	ASM 16
27	Hodoscope 1
28	Hodoscope 2
29	Hodoscope 3
30	Hodoscope 4
31	Hodoscope 5
32	Hodoscope 6
33	Hodoscope 7
34	Hodoscope 8
99	$\mu$ -TCA

### A.2.1.2 Pre-trigger and trigger

The trigger number identifies each event, where an event is generated every time a coincidence is detected between a BGO block and a silicon layer. Once an interaction is detected in a BGO block, the associated ASM card generates a pre-trigger signal which is sent to the THOR card. This intermediate card shares the pre-trigger signal with the silicon FE cards; if an interaction with a compatible time stamp is found in one of the silicon layer, a trigger signal is generated and sent to all the silicon FE card, as well as to the ASM and hodoscope cards via the THOR card. The trigger signal validates the event, and each FE card sends the collected data to the  $\mu$ -TCA system. The trigger number allows for a complete event reconstruction by the event builder on the acquisition PC. In Figure ?? the trigger generation process is sketched.

To be noticed that each FE cards sends the collected data independently from the others.

#### Trigger and pre-trigger encoding

Pre-trigger and trigger signals are used by all the detectors to select the collected data to be sent to the acquisition system. The data selection and transfer must be as fast as possible in order to minimize the trigger latency and camera dead time. In order to reduce the transmission time, pre-trigger and trigger signals have been encoded on 24 bits.

This same trigger number is sent at the beginning of each data packet and is used by the event builder to associate the interactions collected by the three detector sections. With a 24-bit encoding, the trigger number is reset every  $1 \text{ ns} \times 2^{24} = 16,78 \text{ ms}$ . This time window is short for the event builder, so that for the physical data it is extended to 32 bits for all the FE cards in order to have a reset every  $1 \text{ ns} \times 2^{32} = 4,2 \text{ s}$ , which is enough for the reconstruction of the events.

### A.2.1.3 Mode number

The Compton camera detector components can work in different mode, according to the application requirements. At least two working modes are possible for every detector section: an “optimal” mode, corresponding to the final camera configuration; a “test” mode, allowing for the collection of more raw information. Every operating mode presents a peculiar data format, so that the data packets size is not fixed. In order to fix the acquisition tuning, the mode number is defined before its beginning.

The operating mode are identified as following:

- N° Mode = 1 : 1<sup>st</sup> mode for silicon
- N° Mode = 2 : 2<sup>nd</sup> mode for silicon
- N° Mode = 3 : 3<sup>rd</sup> mode for silicon
- N° Mode = 4 : 4<sup>th</sup> mode for silicon

## A Compton camera data format

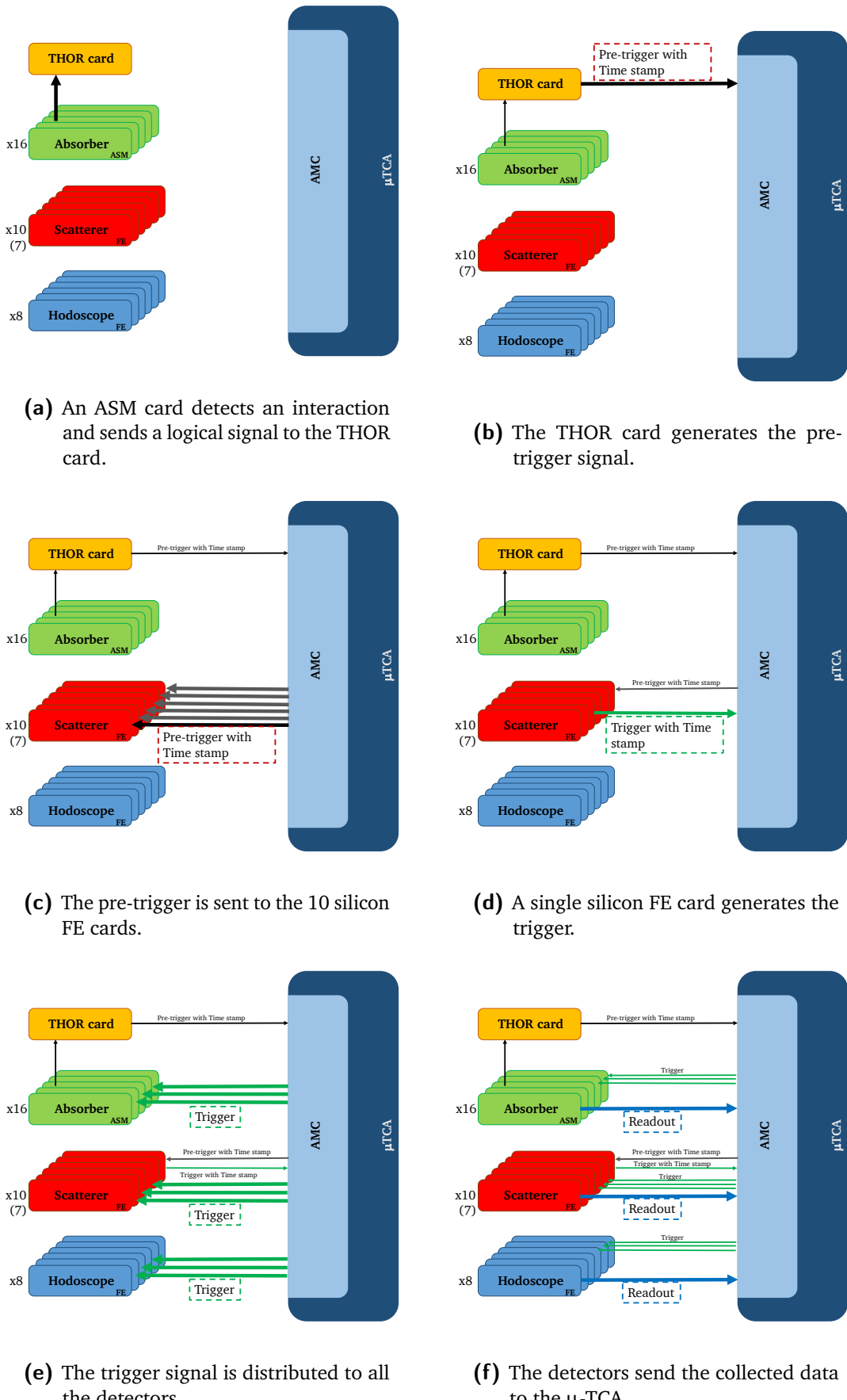


**Figure A.1:** Data acquisition logic: pre-trigger and trigger generation and readout process.

- N° Mode = 5 : 1<sup>st</sup> mode for BGO
- N° Mode = 6 : 2<sup>nd</sup> mode for BGO
- N° Mode = 7 : 1<sup>st</sup> mode for hodoscope
- N° Mode = 8 : 2<sup>nd</sup> mode for hodoscope.

## A.3 Physical data format

### A.3.1 Scatterer detector data format

Four different data formats, corresponding to four working modes, have been defined for the silicon scatterer operation (figure 2). For mode 1 and 2, the collected total charge is directly evaluated on the FE card via the slow shaper output and one ASIC, while for mode 3 and 4 the ASIC pre-amplifier output directly sends a sampling of the raw signal. In this last case, the number of samples can be tuned and each sample corresponds to 10 ns. The complete sampling is stored in a dedicated buffer (see table 9).

#### Modes 1 and 3

In mode 1 and 3, for each detector strip involved in the interaction, the strip ID, total collected charge and time are stored. The interaction position will be calculated via a center of gravity algorithm at the analysis stage. The raw information about the number of involved strips is useful for the evaluation of the signal dispersion in the detector.

#### Modes 2 and 4

In mode 2 and 4, the interaction is calculated on the FE card and the number of involved strip is then not stored.

### A.3.2 Absorber detector data format

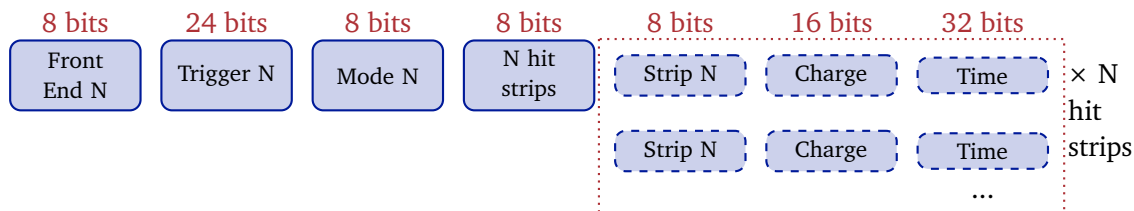
The BGO block readout is performed via the ASM cards. Each card is equipped with 24 input ports (signal PM), corresponding to 6 BGO blocks. Two possible working modes have been defined for the BGO absorber: the collected total charge and time are evaluated on the card, or the PM raw signals are sampled and the sampling is sent to the acquisition (figure 3). Charge and time are then calculated at the analysis stage. This second operating mode can be useful in the test phase but it determines a low acquisition rate, so that it can be used only at low beam intensity.

The complete sampling is stored in a dedicated buffer (see table 9).

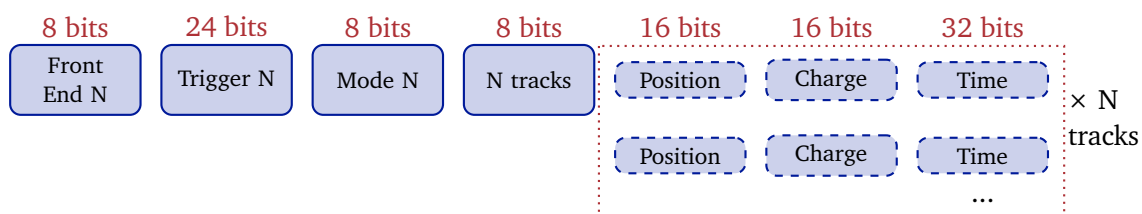
## A Compton camera data format

---

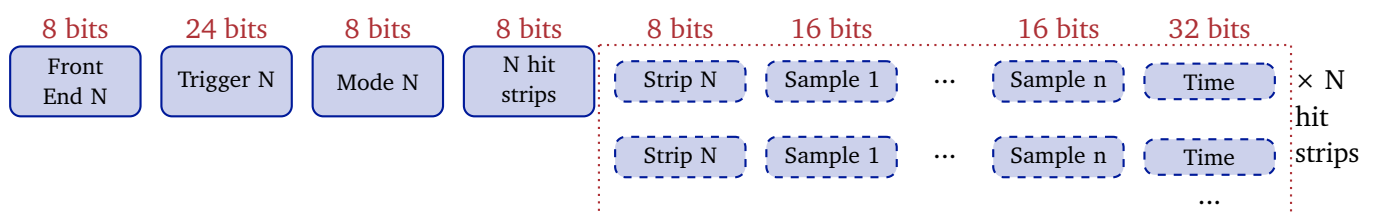
### Mode 1



### Mode 2



### Mode 3



### Mode 4

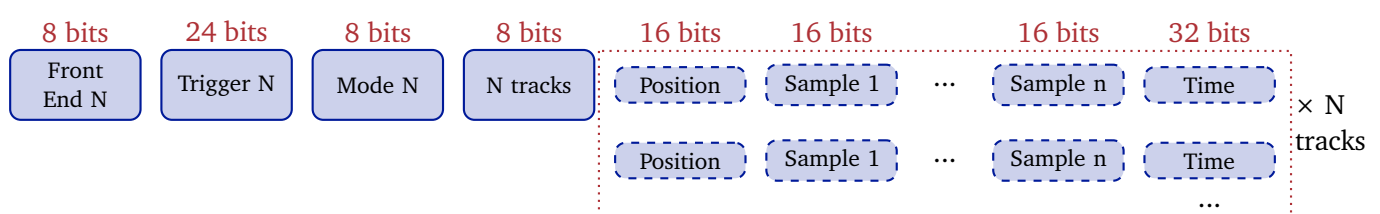
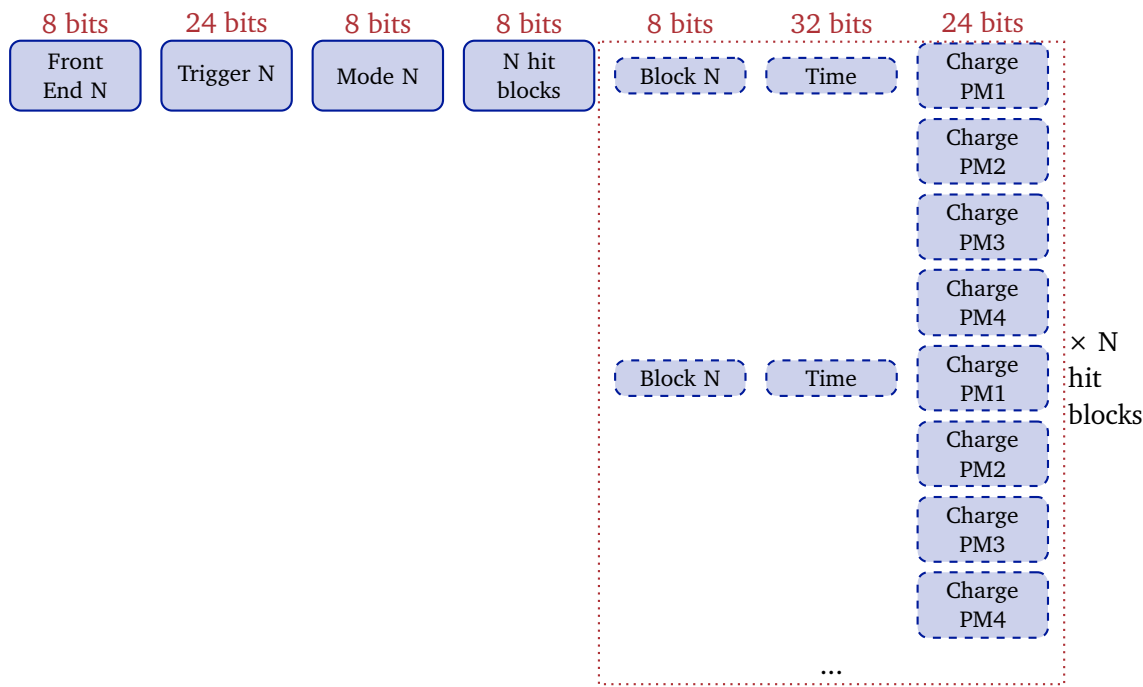


**Figure A.2:** Scatterer detector data format.

## Mode 1



## Mode 2

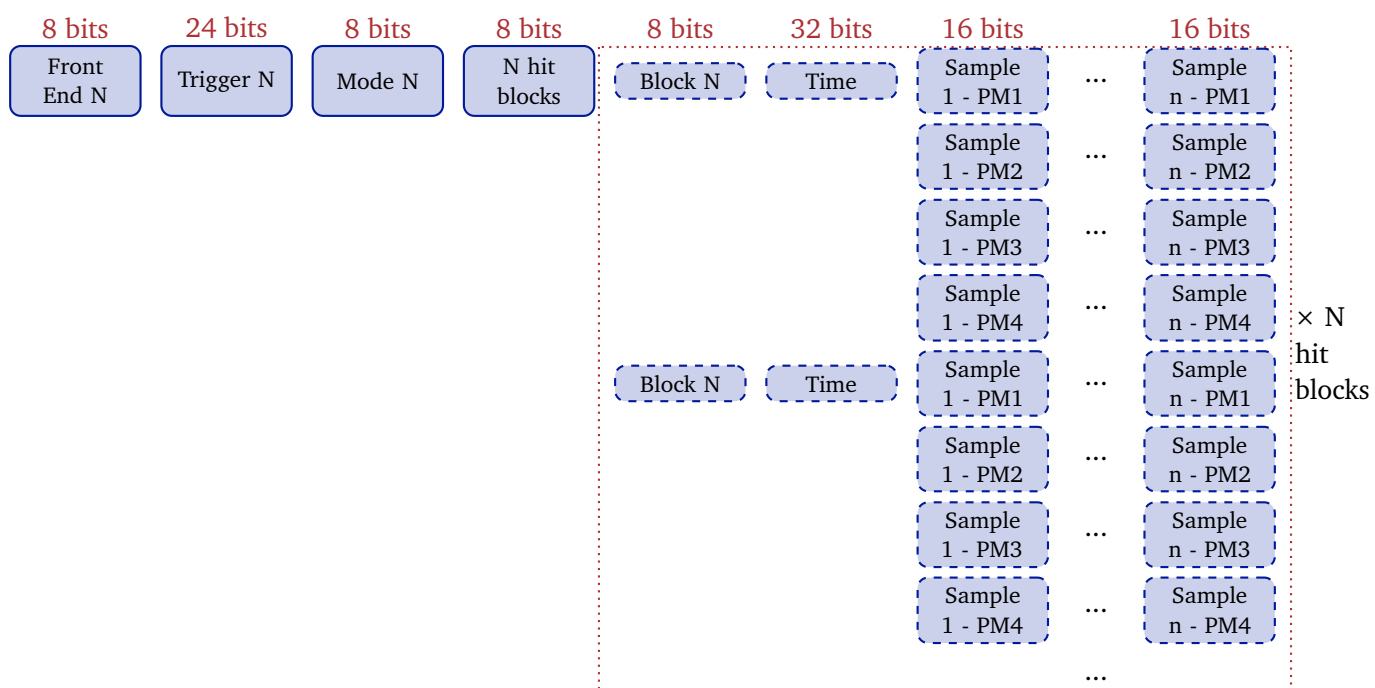


**Figure A.3:** Absorber detector data format.

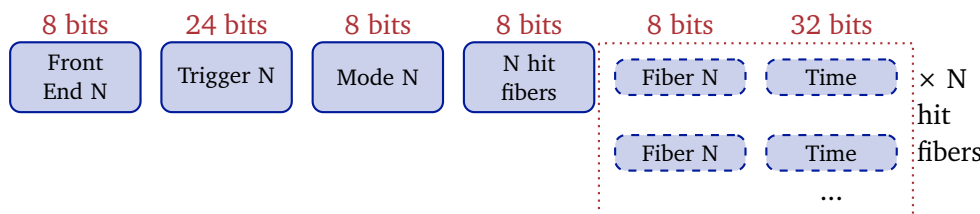
### A.3.3 Beam hodoscope data format

The beam tagging hodoscope is composed of two perpendicular planes of 128 scintillating fibers each. Each fiber is read-out on the two sides, for a total of 512 read-out channels. The output signals are send via optical fibers to 8 64-channel PM H8500 by Hamamatsu. 8 FE cards have been developed for the signal collection, one per PM, and are equipped with two custom ASICs (32 channels each) and one FPGA.

Concerning the “optimal” mode (1<sup>st</sup> operating mode for the hodoscope), the only collected information are the ID of the involved fibers and the interaction time. The ASICs allow for a minimum time resolution of 10 ns; this means that if two particles interacts in the hodoscope within a 10 ns window, they will be considered as part of a single event.

In test mode, the total collected charge can be calculated. This feature is useful to evaluate the detector aging effect due to radiation exposure. The charge measurement is anyway limited to a single channel per ASIC, so to two channels per PM. The ASIC channel able to measure the charge is identified as “N° Fiber charge 1” and “N° Fiber charge 2”.

#### Mode 1



#### Mode 2

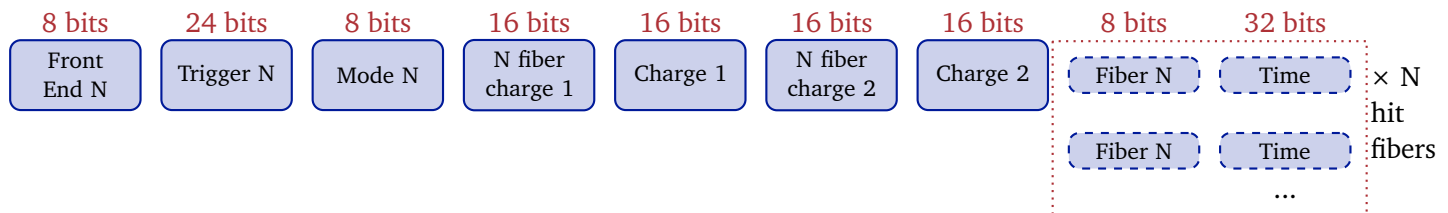


**Figure A.4:** Beam hodoscope data format.

## A.4 Slow control, trigger and monitoring data format

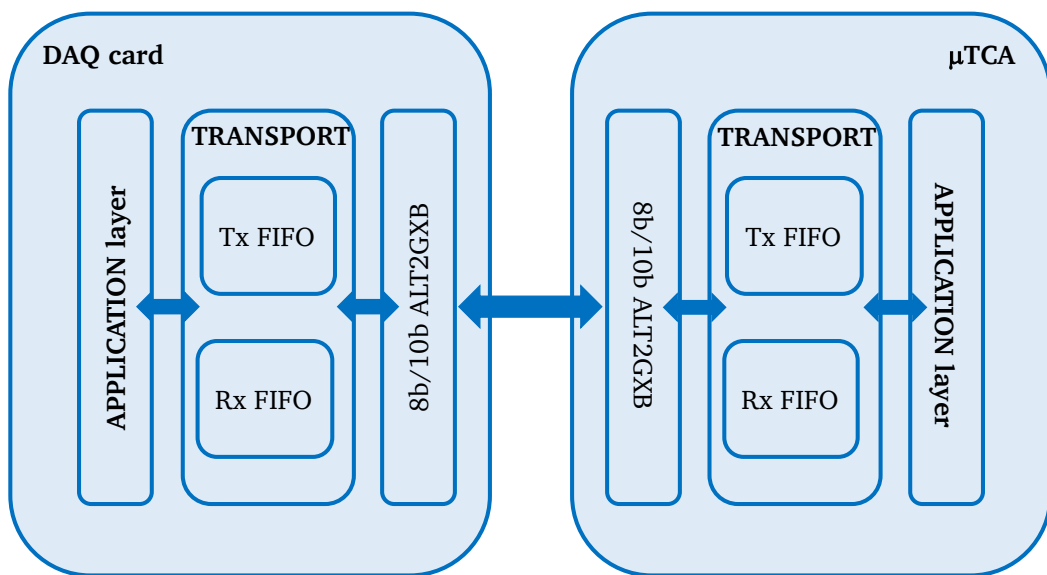
### A.4.1 Communication architecture

The Endpoint architecture is composed of three layers:

- application layer

- mac (or transport) layer/processor packet
- physical layer

**Figure A.5:** Architecture of communication between DAQ cards and μ-TCA.



## A.4.2 Transport protocol and processor packets

### A.4.2.1 Definitions

It is worth to define some useful terms for the following part of the document:

- byte : 8 bits
- word : 16 bits
- K : control byte
- D : data byte
- cargo : data group
- terminator : packet end

- CRC : cyclic redundancy code

The CRC allows one to detect the transmission errors and the data transfer issues. A specific algorithm must be used, as CRC-16 :  $X^{16} + X^{15} + X^2 + 1$ . In the present protocol, a “parity pattern of 16 bits” have been used.

The transport layer ensures a proper packets exchange between two terminals via the data encapsulation. The data come from the application layer and are then sent to the physical layer.

### A.4.2.2 Data encoding

For the transport layer, the data structure is created via the addition of a packet header, corresponding to a parity bit, of a 16 bit parity pattern and a bit for the end of the packet. The data are 8 bits/10 bits encoded. This standard 8 bits/10 bits encoding ensures sufficient data transitions for clock recovery.

### A.4.2.3 Packets format

All the data packets have the same structure. A K byte (control symbol) is followed by the cargo to be sent. The end of the packets changes according to the cargo parity.  
If the cargo contains an even number of bytes, the packet ends with K.28.6.

**Table A.2:** Packet with an even byte number cargo.

Item	Packet beginning	Cargo	Packet end
1	One K byte	0 - N D-bytes	K.28.6

If the cargo contains an odd number of bytes, the packet ends without any control symbol.

**Table A.3:** Packet with an odd byte number cargo.

Item	Packet beginning	Cargo	Packet end
1	One K byte	0 - N D-bytes	Beginning of a new packet

Remark :

- SYN packet is a special kind of packet starting with K.28.6 and ending with K.28.5. It is only composed of these two bytes (16 bits). It allows the receiver to find the beginning

and the end of the transmitted bytes with the aim to reconstruct the events in parallel. The synchronization speed is 44 Hz (defined by Carlos Abellan).

- In order to optimize the throughput, the control symbol at the beginning of the packet can probably be removed (further study needed).

#### A.4.2.4 Possible control symbols

In the following table, all the possible control symbols are listed (defined by Carlos Abellan).

**Table A.4:** Control symbol definition.

Item	Name	Control code	Comment
1	K.28.0	0x1C	Acknowledgement
2	K.28.1	0x3C	Ask for writing registers
3	K.28.2	0x5C	Ask for reading registers
4	K.28.3	0x7C	Special command
5	K.28.4	0x9C	Monitoring
6	K.28.5	0xBC	Default synchronization
7	K.28.6	0xDC	IDLE (default) and packet end
8	K.28.7	0xFC	Pre-trigger
9	K.23.7	0xF7	Trigger
10	K.27.7	0xFB	
11	K.29.7	0xFD	
12	K.30.7	0xFE	Physical data

### A.4.3 Transport layer

#### A.4.3.1 Control packet

This kind of packet is used to check the link and for the control/command operations.

- For the link check, two kinds of packets are used: synchronization packet and IDLE packet.
- For the control/command operations, here are some examples: register configuration, FPGA dynamical programming, monitoring, etc.

Control symbol for control :

Acknowledgement packet (Front End cards → μ-TCA)

**Table A.5:** Control symbol definition.

Item	Name	Control code	Comment
1	K.28.0	0x1C	Acknowledgement
2	K.28.1	0x3C	Ask for writing registers
3	K.28.2	0x5C	Ask for reading registers
4	K.28.3	0x7C	Special command
5	K.28.4	0x9C	Monitoring
6	K.28.5	0xBC	Synchronization
7	K.28.6	0xDC	IDLE (default) and end of packet

This packet is sent by the FE cards and interpreted as an acknowledgement by the  $\mu$ -TCA. If a part is missing, it is set to zero.

- If 0 = validation
- If 1 = problem detected

**Table A.6:** Definition of the acknowledgement packet.

Word	1 <sup>st</sup> byte	2 <sup>nd</sup> byte							
		7b	6b	5b	4b	3b	2b	1b	0b
1	K.28.0	0	Pb Front End num- ber	Pb with packet begin- ning	Pb with packet end	Pb with CRC	Pb with number of re- ceived words	Pb with parity bit of the ac- knowl- edge- ment words	parity bit of the ac- knowl- edge- ment packet
2	Front End number								

#### A.4.3.2 Configuration packets

##### Writing register process ( $\mu$ -TCA → Front End cards)

The process starts with a packet sent by the  $\mu$ -TCA asking for the register writing. The receiver (FE card) sends back an acknowledgement packet to finish the process. In the following table the format of this writing register packet is reported.

##### Reading register process ( $\mu$ -TCA → Front End cards)

The process starts with a packet sent by the  $\mu$ -TCA asking for the register reading. The re-

**Table A.7:** Writing register packet.

Word	1 <sup>st</sup> byte	2 <sup>nd</sup> byte	Comment
1	K.28.1	Front End number + 1 parity bit	N/A
2	2 bytes with the number of words to be written		The length is word-based: max $2^{16} - 1 = 65535$ words
3	Register address		Address where the writing process starts
4..N+3	Data to be written		0000 0000
N+4	CRC composed of the “xor” of all bits in the same position, from word 2 to word (N+3)		

ceiver (FE card) sends back the “measure packet” (Table 10) if the command is correct, an acknowledgement packet if it is not.

At the beginning of the slow control, the physical addresses on the FE cards are read at the address 0 (Table 9).

In the following table the format of this reading register packet is reported.

**Table A.8:** Reading register packet.

Word	1 <sup>st</sup> byte	2 <sup>nd</sup> byte	Comment
1	K.28.2	Front End number + 1 parity bit	N/A
2	2 bytes with the number of words to be read		The length is word-based: max $2^{16} - 1 = 65535$ words
3	Address of 1 <sup>st</sup> data to be read		Address where the reading process starts
4	CRC composed of the “xor” of all bits in the same position, from word 2 to word 3		/

#### A.4.3.3 Monitoring process (Front End cards → μ-TCA)

In case of issues, for example when the temperature of a card go beyond a fixed threshold, the DAQ card sends a “monitoring” packet to the μ-TCA. There is not a corresponding acknowledgement from the μ-TCA.

## A Compton camera data format

---

**Table A.9:** Two special registers( $\mu$ -TCA → Front End cards)

Register address	Details	Comment
0	Front End number	No writing rights: register in read-only mode. Hard coded on DAQ card.
1	It defines the working modes (Table 1)	Optimal mode, test mode, collimated camera mode, Compton camera mode, individual detector section test. It is possible to write in the register.
2	It defines the detector to test (in single detector test mode)	Scatterer, absorber, hodoscope.
3	BGO number of sampling	For test mode with the BGO blocks signal sampling.
4	Silicon number of sampling	For test mode with the silicon layers signal sampling.

**Table A.10:** Measurement packet (Front End cards →  $\mu$ -TCA)

Word	1 <sup>st</sup> byte	2 <sup>nd</sup> byte	Comment
1	K.28.1	Front End number + 1 parity bit	
2	2 bytes for the number of data words to send		The length is word-based: max $2^{16} - 1 = 65535$ words
3	Register address		Address where the writing process starts
4..N+3	Read data		0000 0000
N+4	CRC composed of the “xor” of all bits in the same position, from word 2 to word (N+3)		/

**Table A.11:** Monitoring packet.

Word	1 <sup>st</sup> byte	2 <sup>nd</sup> byte	Comment
1	K.28.4.	Front End number + 1 parity bit	Message in Table ??.
2	15 bits for the message + 1 parity bit		Message in Table ??.

**Table A.12:** Monitoring messages.

Item	Message	Bit[15]	...	Bit[7]	Bit[6]	Bit[5]	Bit[4]	Bit[3]	Bit[2]	Bit[1]	Comment
		Message type						Further information			
1	FPGA recon-figura-tion error	0	0	0	0	0	1	0	0	0	N/A
2	Tempe- rature alarm	0	0	0	0	1	0	x	x	x	Bit “x” is 1 if the corresponding detector goes beyond the threshold (0 elsewhere)
3	Busy	0	0	0	1	0	0	0	0	0	Front End is not able to send data
...											

#### A.4.3.4 Special command process ( $\mu$ -TCA $\rightarrow$ Front End cards)

This process is designed to allow the  $\mu$ -TCA to send special commands to the FE cards.

**Table A.13:** Special command packets

Word	1 <sup>st</sup> byte	2 <sup>nd</sup> byte
1	K.28.3	Front End number + 1 parity bit
2	15 bits for the special command + 1 parity bit	

A register database (containing the operating mode identification) must be fixed and shared between all the detectors.

#### A.4.4 Data packets (Front End card $\rightarrow$ $\mu$ -TCA)

In the section the packets concerning trigger, pre-trigger and physical data are described. No acknowledgement is demanded for this kind of packets.

##### Pre-trigger format

This packet is sent to the  $\mu$ -TCA by the THOR card. The  $\mu$ -TCA then shares it with all the

**Table A.14:** Special commands examples

Item	Command name	Bit[15..1] of 2 <sup>nd</sup> word	Comment
1	System reset	"0000 0000 0001 001"	Acknowledgement packet missing
2	Counter reset	"0000 0000 0001 000"	Acknowledgement packet needed
3	Start run	"0000 0000 0000 100"	Acknowledgement packet needed
4	Stop run	"0000 0000 0000 101"	Acknowledgement packet needed
5	Dynamical FPGA configuration	"0000 0000 0000 010"	Acknowledgement packet needed
6	Veto	"0000 0000 0000 011"	Example: $\mu$ -TCA cannot receive the data. Acknowledgement packet needed

**Table A.15:** Control symbol for pre-trigger, trigger and physical data.

Item	Name	Control code	Comment
1	K.28.7	0xFC	The pre-trigger is generated by the THOR card and sent to the $\mu$ -TCA who shares it with the silicon layers cards.
2	K.23.7	0xF7	The trigger is generated by a single silicon layer card and sent to the $\mu$ -TCA who shares it with all the FE cards.
5	K.30.7	0xFE	The FE cards send the data.

silicon FE cards.

**Table A.16:** Pre-trigger packet

Item	1 <sup>st</sup> byte	2 <sup>nd</sup> - 4 <sup>th</sup> bytes
1	K.28.7	24 bits for the trigger number

#### Trigger format

This packet is sent back to the  $\mu$ -TCA if a silicon FE card finds an interaction in coincidence after the reception of the pre-trigger packet. The trigger is always sent before the physical data packets. The  $\mu$ -TCA then sends the trigger packet to all the FE cards (scatterer, absorber, hodoscope).

**Table A.17:** Trigger packet

Item	1 <sup>st</sup> byte	2 <sup>nd</sup> - 4 <sup>th</sup> bytes
1	K.23.7	24 bits for the trigger number

#### Physical data packet format

This packet sends the “useful” data to the  $\mu$ -TCA. The data format (cargo) is defined in chapter 3.

**Table A.18:** Physical data packet

Item	1 <sup>st</sup> byte	Cargo	End of packet
1	K.30.7.	From 0 to Nbr-1 words of D characters	K.28.6 or the beginning of a new packet.

## A.5 UDP packets format

Once the  $\mu$ -TCA receives the data from the FE cards, a physical event is generated and stored in dedicated buffers. The buffers are then sent to the acquisition PC via UDP packets. Each detector section has its own UDP socket, and three receiving ports are used for the three data fluxes: 60001 for the hodoscope, 60002 for the absorber, 60003 for the scatterer. The content of the data buffers are sent in order to avoid to divide events in different packets, so that each UDP packet is completely independent from the others and contains complete events. The maximum size of a packet is set to 1500 (UDP data = 1472), or to 9000 for the so called “jumbo frames”, used for high speed acquisitions.

Each UDP packet has a custom defined header, composed of:

- 32 bits: packet number, starting from 0;

- 16 bits: number of data structures in the packet;

The data structures are then in a list one after the other with the already described format.

## A.6 Data throughput expected in clinical conditions

### A.6.1 Clinical intensities

In clinical standards, the beam maximum intensity is:

- protons :  $10^{10}$  protons/s
- carbon ions :  $5 \times 10^7$  C ions/s

The Compton camera must be designed in order to be able to handle the whole range of clinical intensities. The design reference is then the maximum intensity, about  $3.2 \text{ nA}$  ( $2 \times 10^{10}$  protons/s) delivered by the cyclotron C230 by IBA. The number of proton delivered per second is higher than the maximum considered rate ( $10^{10}$  protons/s).

As shown by the simulation results, the Compton camera can not be used for an online monitoring at the maximum beam intensity for both proton and carbon ion beams. The main limitation comes from the amount of random coincidences detected by the camera for high intensity beams. One possible solution is to deliver a lower intensity beam for the range monitoring before the beginning of the treatment. The results shown here relates to a reduced intensity, corresponding to the one selected via the simulation studies.

#### A.6.1.1 Review: detector and target sizes

Detectors sizes:

- Silicon scatterer : 7 silicon layers,  $9.6 \times 9.6 \times 0.2 \text{ cm}^3$  (first layer 20 cm far from the beam line)
- BGO absorber: BGO block  $3.5 \times 3.8 \times 3.0 \text{ cm}^3$  (67.5 cm far from the beam line - center of the block)

PMMA target size: cylindrical shape, diameter 15 cm, 20 cm length along the beam direction.

### A.6.2 Coincidence rate

In the following table the coincidence and single (pre-trigger) rates expected for the different detector section are listed according to the beam kind and intensity. These values correspond to the Compton camera, while for the collimated camera a reduced rate is expected for the absorber due to the presence of the physical collimator.

**Table A.19:** Coincidence and single rate as a function of the beam intensity. The BGO single rate corresponds to the pre-trigger rate.

	Clinical intensity		Reduced intensity		Collimated camera	
	Protons	Carbon ions	Protons	Carbon ions	Protons	Carbon ions
Intensity(ions/s)	$2 \times 10^{10}$	$5 \times 10^7$	$1 \times 10^8$	$5 \times 10^6$	$2 \times 10^{10}$	$5 \times 10^7$
Coincidence rate per incident ion	$9 \times 10^{-4}$	$8 \times 10^{-4}$	$9 \times 10^{-4}$	$8 \times 10^{-4}$	/	/
Coincidence rate (Hz)	$1,8 \times 10^7$	$4 \times 10^4$	$9 \times 10^4$	$4 \times 10^3$	/	/
Single rate BGO (Hz) - 96 blocks	$7,8 \times 10^7$	$1,4 \times 10^6$	$3,9 \times 10^5$	$1,4 \times 10^5$	/	/
Single rate BGO (Hz) - 1 block	$8,1 \times 10^5$	$1,5 \times 10^4$	$4 \times 10^3$	$1,5 \times 10^3$	/	/
Single rate BGO (Hz) - 1 ASM card (6 blocks)	$6,5 \times 10^6$	$1,2 \times 10^5$	$3,2 \times 10^4$	$1,2 \times 10^4$	/	/

The application of the Compton camera at clinical intensity seems not feasible. The camera distance with respect to the beam line should be increased to lower the rate to  $1 \times 10^5$  Hz (which means to put the 1

### A.6.3 Data flow (Front End cards → μ-TCA)

The data format previously described has been used to evaluate the data flow between each FE card and the μ-TCA. The calculation is performed according to the “optimal” mode of each detector. For the BGO, we only consider events where the 4 PMs are involved. For the silicon layers, two cases are considered:

- Case 1 : one single layer with 6 involved strips;
- Case 2 : all the 7 layers involved with 6 hit strips per layer.

Concerning the hodoscope, we considered an event with one hit fiber readout on the two sides.

The 8bits/10bits encoding is included in the calculation.

**Table A.20:** Data flux between FE cards and  $\mu$ -TCA.

	Clinical intensity	Reduced intensity		
	<u>Protons</u>	<u>Carbon ions</u>	<u>Protons</u>	<u>Carbon ions</u>
<b>Intensity (ions/s)</b>	$2 \times 10^{10}$	$5 \times 10^7$	$1 \times 10^8$	$5 \times 10^6$
<b>Pre-trigger flux (Mbits/s)</b>	$2,5 \times 10^3$	47,6	13,3	4,76
<b>Trigger flux (Mbits/s)</b>	612	1,4	3,1	0,1
<b>BGO data flux (Mbits/s) - 96 blocks</b>	$1,7 \times 10^5$	373	873	37,3
<b>BGO data flux (Mbits/s)- 1 block</b>	$1,7 \times 10^3$	3,88	8,73	0,3
<b>BGO data flux (Mbits/s) - 1 carte</b>	$1,4 \times 10^4$	31,1	69,9	3,1
<b>ASM</b>				
<b>Silicon data flux (Mbits/s) - case 1</b>	$2,3 \times 10^5$	522	$1,2 \times 10^3$	52,2
<b>Silicon data flux (Mbits/s) - case 2</b>	$1,6 \times 10^6$	$3,7 \times 10^3$	$8,2 \times 10^3$	366
<b>Hodoscope data flux (Mbits/s)</b>	$8,1 \times 10^4$	180	404	18

#### A.6.4 Acquisition data flow ( $\mu$ -TCA $\rightarrow$ Acquisition PC)

The data flow from the  $\mu$ -TCA to the acquisition PC is detailed here. The UDP encoding is included in the calculation.

**Table A.21:** Data flow between  $\mu$ -TCA and acquisition PC.

	Clinical intensity	Reduced intensity		
	<u>Protons</u>	<u>Carbon ions</u>	<u>Protons</u>	<u>Carbon ions</u>
<b>Intensity (ions/s)</b>	$2 \times 10^{10}$	$5 \times 10^7$	$1 \times 10^8$	$5 \times 10^6$
<b>Coincidence rate per incident ion</b>	$9 \times 10^{-4}$	$8 \times 10^{-4}$	$9 \times 10^{-4}$	$8 \times 10^{-4}$
<b>Coincidence rate (Hz)</b>	$1,8 \times 10^7$	$4 \times 10^4$	$9 \times 10^4$	$4 \times 10^3$
<b>Data flow (Mbits/s) - case 1</b>	$2,2 \times 10^4$	46,7	112	5,0
<b>Data flow (Mbits/s) - case 2</b>	$6 \times 10^4$	133	300	13,3

### A.6.5 Conclusions

As already mentioned, the Compton camera application is not feasible at clinical beam intensities.

In order to have an online monitoring of the beam range, a reduced intensity must be foreseen. The main limitation is the rate of random coincidences detected at high intensity, while from the technological point of view no limitations are highlighted by this study. In the collimated camera configuration, where no coincidences are required and the random coincidences limitation is removed, we can then expect to be able to work at real clinical intensity.



# B

## Electronics specifications







# Acronyms

**ADC** Analog-to-Digital Converter. 24, 27, 28, 30, 34, 35

**ASIC** Application-Specific Integrated Circuit. 12, 20

**BaF<sub>2</sub>** Barium Fluoride. 29, 30, 36

**BGO** Bismuth Germanium Oxide - Bi<sub>12</sub>GeO<sub>20</sub>. iv, vii, viii, xi, 7, 13–17, 23, 26, 27, 30, 36, 38, 39, 47, 48, 56

**CdTe** Cadmium Telluride. 48

**CLaRyS** Contrôle en Ligne de lâhadronthérapie par Rayonnements Secondaires - Online monitoring of ion beam therapy through secondary particles. vii, 8, 10, 17–19, 23, 44, 45, 55, 59, 61

**CPPM** Centre de Physique des Particules de Marseille. 8

**CREATIS** Centre de Recherche en Acquisition et Traitement de l’Image pour la Santé. 8, 48

**DSSD** Double-sided Silicon Strip Detector. 10, 11

**ENC** Equivalent Noise Charge. 12, 47

**FE** Front-End. 10–12, 16–18, 20–22

**FWHM** Full Width at Half Maximum. 11, 22, 24, 30, 34–36, 39, 47, 48

**GANIL** Grand Accelerateur National d’Ions Lourds. 21, 47

**GATE** GEANT4 Application for Tomographic Emission. 49

**GEANT4** GEometry And Tracking 4. 45

**HEGP** High Energy General Purpose. 50

**HIT** Heidelberg Ion Therapy Center. 21

**IPNL** Institut de Physique Nucléaire de Lyon. vii, 8, 10–12, 16, 18, 20, 23, 27

**IPNO** Institut de Physique Nucléaire d’Orsay. 21

## Acronyms

---

- IRFU** Institut de Recherche sur les lois Fondamentales de l'Univers. 27
- LAL** Laboratoire de l'Accélérateur Linéaire. 27
- LED** Light Emitting Diode. 23, 24
- LM-MLEM** List Mode-Maximum Likelihood Expectation Maximization. 48, 56
- LPC** Laboratoire de Physique de Clermont. 8, 16, 23
- LPSC** Laboratoire de Physique Subatomique et Corpusculaire. 8
- LYSO** Lutetium-Yttrium OxyorthoSilicate -  $\text{Lu}_{2(1-x)}\text{Y}_{2x}\text{SiO}_5$ . 14
- MEGAlib** Medium-Energy Gamma-ray Astronomy library. 48
- NaI(Tl)** Sodium Iodide doped with Thallium. 49–51
- NIM** Nuclear Instrumentation Module. 27, 30
- PET** Positron Emission Tomography. 8, 13, 17, 26, 36, 44
- PM** Photo-Multiplier. iii, iv, vii, 7, 14, 16, 18–21, 23, 24, 26–28, 30–32
- PMMA** Poly Methyl Metacrylate. 16
- RMS** Root Mean Square. 12
- SPECT** Single Photon Emission Computed Tomography. 44, 45, 49, 59
- TOF** Time-Of-Flight. 8, 10, 17, 23

# Bibliography

- Adam, L. E.**, J. Zaers, H. Ostertag, H. Trojan, M. E. Bellemann, and G. Brix (June 1997). “Performance evaluation of the whole-body PET scanner ECAT EXACT HR + following the IEC standard”. In: *IEEE Transactions on Nuclear Science* 44.3, pp. 1172–1179. ISSN: 0018-9499. DOI: 10.1109/23.596983 (cit. on p. 13).
- Anger, H. O.** (1958). “Scintillation Camera”. In: *Review of Scientific Instruments* 29.1, pp. 27–33. DOI: 10.1063/1.1715998. eprint: <http://dx.doi.org/10.1063/1.1715998>. URL: <http://dx.doi.org/10.1063/1.1715998> (cit. on p. 44).
- Anger, H. O.** (1964). “Scintillation Camera with Multichannel Collimators”. In: *Journal of Nuclear Medicine* 5.7, pp. 515–531. eprint: <http://jnm.snmjournals.org/content/5/7/515.full.pdf+html>. URL: <http://jnm.snmjournals.org/content/5/7/515.short> (cit. on p. 44).
- AspenAerogels** (2011). *Spaceloft® - High performance Insulation for building envelopes. Data Sheet*. Aspen Aerogels Inc. (cit. on p. 12).
- Bhat, M. R.** (1992). *Evaluated Nuclear Structure Data File (ENSDF), Nuclear Data for Science and Technology, page 817*, edited by S. M. Qaim (SpringerVerlag, Berlin, Germany, 1992). URL: <https://www.nndc.bnl.gov/> (visited on 03/27/2017) (cit. on p. 46).
- Breton, D.**, E. Delagnes, J. Maalmi, and P. Rusquart (May 2014). “The WaveCatcher family of SCA-based 12-bit 3.2-GS/s fast digitizers”. In: *2014 19th IEEE-NPSS Real Time Conference*, pp. 1–8. DOI: 10.1109/RTC.2014.7097545 (cit. on p. 27).
- Brix, G.**, J. Zaers, L.-E. Adam, M. E. Bellemann, H. Ostertag, H. Trojan, U. Haberkorn, J. Doll, F. Oberdorfer, and W. Lorenz (1997). “Performance Evaluation of a Whole-Body PET Scanner Using the NEMA Protocol”. In: *Journal of Nuclear Medicine* 38.10, pp. 1614–1623. eprint: <http://jnm.snmjournals.org/content/38/10/1614.full.pdf+html>. URL: <http://jnm.snmjournals.org/content/38/10/1614.short> (cit. on p. 13).
- Cecchin, D.**, D. Poggiali, L. Riccardin, P. Turco, F. Bui, and S. De Marchi (2015). “Analytical and experimental FWHM of a gamma camera: theoretical and practical issues.” In: *PeerJ* 3:e722 (cit. on p. 53).
- Coudurier, V.** (2015). “Caractérisation d’un hodoscope de faisceau pour l’hadronthérapie”. Master internship report (cit. on p. 24).
- Dahoumane, M.**, D. Dauvergne, J. Krimmer, J. L. Ley, E. Testa, and Y. Zoccarato (Nov. 2014). “A low noise and high dynamic range CMOS integrated Electronics associated with double sided Silicon Strip Detectors for a Compton camera gamma-ray detecting system”. In: *2014 IEEE Nuclear Science Symposium and Medical Imaging Conference (NSS/MIC)*, pp. 1–6. DOI: 10.1109/NSSMIC.2014.7431122 (cit. on p. 12).
- Deng, S.**, H. Mathez, D. Dauvergne, Y. Zoccarato, and G.-N. Lu (2012). “Front-end multi-channel PMT-associated readout chip for hodoscope application”. In: *Nuclear Instruments and Methods*

- in Physics Research Section A: Accelerators, Spectrometers, Detectors and Associated Equipment* 695. New Developments in Photodetection NDIP11, pp. 390–393. ISSN: 0168-9002. DOI: <https://doi.org/10.1016/j.nima.2011.11.042>. URL: <http://www.sciencedirect.com/science/article/pii/S0168900211020845> (cit. on p. 20).
- Deng, S., H. Mathez, D. Dauvergne, Y. Zoccarato, and G.-N. Lu (Jan. 2013). “Very fast front end ASIC associated with multi-anode PMTs for a scintillating-fibre beam hodoscope”. In: *Journal of Instrumentation* 8, p. C01047. DOI: 10.1088/1748-0221/8/01/C01047. URL: <https://hal.archives-ouvertes.fr/hal-00990850> (cit. on p. 20).
- Everett, D. B., J. S. Fleming, R. W. Todd, and J. M. Nightingale (1977). “Gamma-radiation imaging system based on the Compton effect”. In: *Proceedings of the Institution of Electrical Engineers* 124.11, pp. 995–. ISSN: 0020-3270. DOI: 10.1049/piee.1977.0203 (cit. on p. 44).
- Fontana, M., D. Dauvergne, J. M. Létang, J.-L. Ley, and É. Testa (2017a). “Compton camera study for high efficiency SPECT and benchmark with Anger system”. In: *Physics in Medicine and Biology* 62.23, p. 8794. URL: <http://stacks.iop.org/0031-9155/62/i=23/a=8794> (cit. on p. 43).
- Fontana, M., D. Dauvergne, J.-L. Ley, J. M. Létang, V. Maxim, and É. Testa (2017b). “Versatile Compton camera for high energy gamma rays: Monte Carlo comparison with Anger camera for medical imaging”. In: *2nd Jagiellonian Symposium on Fundamental and Applied Subatomic Physics*. Vol. 48. Krakow, Poland, pp. 1639–1645. DOI: 10.5506/APhysPolB.48.1639. URL: <https://hal.archives-ouvertes.fr/hal-01609541> (cit. on p. 43).
- Gaglione, R. (2013). “Electronique d’acquisition d’une gamma-caméra.” PhD thesis. École Doctorale Sciences pour l’ingénieur de Clermont-Ferrand (cit. on p. 23).
- GE Healthcare (June 2006). “Infinia”. In: Release 2.5 (cit. on pp. 44, 49).
- GeckoDrive (2010). *G203V stepper drive - data sheet*. REV7. GeckoDrive Motor Controls Inc. (cit. on p. 24).
- Golnik, C. (2015). “Treatment verification in proton therapy based on the detection of prompt gamma-rays.” PhD thesis. TU Dresden and Oncoray (cit. on p. 27).
- Hamamatsu (1995). *Metal Package Photomultiplier Tube R5600 Series*. TPMH1066E08. Hamamatsu Photonics K. K. (cit. on p. 24).
- Hamamatsu (2006). *Flat Panel Type Multianode Photomultiplier Tube Assembly H8500, H8500B*. TPMH1282E09. Hamamatsu Photonics K. K. (cit. on pp. 18, 23).
- Han, L., W. L. Rogers, S. S. Huh, and N. Clinthorne (2008). “Statistical performance evaluation and comparison of a Compton medical imaging system and a collimated Anger camera for higher energy photon imaging”. In: *Physics in Medicine and Biology* 53.24, p. 7029. URL: <http://stacks.iop.org/0031-9155/53/i=24/a=002> (cit. on pp. 44, 45, 47, 59).
- Hubbell, J. H. and M. J. Berger (1987). *XCOM: Photon Cross Sections on a Personal Computer, Report NBSIR 87-3597* (1987), National Institute for Standards and Technology, U.S.A. URL:

---

<http://physics.nist.gov/PhysRefData/XrayMassCoef/> (visited on 02/21/2017) (cit. on pp. 51, 60).

**Hueso-González, F.**, A. Biegun, P. Dendooven, W. Enghardt, F. Fiedler, C. Golnik, K. Heidel, T. Kormoll, J. Petzoldt, K. RÄ¶mer, R. Schwengner, A. Wagner, and G. Pausch (2015). “Comparison of LSO and BGO block detectors for prompt gamma imaging in ion beam therapy”. In: *Journal of Instrumentation* 10.09, P09015. URL: <http://stacks.iop.org/1748-0221/10/i=09/a=P09015> (cit. on pp. 14, 27).

**Kabuki, S.**, K. Hattori, R. Kohara, E. Kunieda, A. Kubo, H. Kubo, K. Miuchi, T. Nakahara, T. Nagayoshi, H. Nishimura, Y. Okada, R. Orito, H. Sekiya, T. Shirahata, A. Takada, T. Tanimori, and K. Ueno (2007). “Development of Electron Tracking Compton Camera using micro pixel gas chamber for medical imaging”. In: *Nuclear Instruments and Methods in Physics Research Section A: Accelerators, Spectrometers, Detectors and Associated Equipment* 580.2. Imaging 2006, pp. 1031–1035. ISSN: 0168-9002. DOI: <https://doi.org/10.1016/j.nima.2007.06.098>. URL: <http://www.sciencedirect.com/science/article/pii/S0168900207013186> (cit. on p. 61).

**Knoll, G. F.** (2000). *Radiation Detection and Measurement*. Third Edition. John Wiley & Sons Inc. (cit. on p. 9).

**Krimmer, J.**, L. Caponetto, X. Chen, M. Chevallier, D. Dauvergne, M. De Rydt, S. M. Deng, J.-L. Ley, H. Mathez, C. Ray, V. Reithinger, E. Testa, and Y. Zoccarato (2018/05/24 2014). “111: Real-time monitoring of the ion range during hadrontherapy: An update on the beam tagging hodoscope”. In: *Radiotherapy and Oncology* 110, S54–S55. DOI: [10.1016/S0167-8140\(15\)34132-3](10.1016/S0167-8140(15)34132-3). URL: [http://dx.doi.org/10.1016/S0167-8140\(15\)34132-3](http://dx.doi.org/10.1016/S0167-8140(15)34132-3) (cit. on p. 20).

**Kuchment, P** and F. Terzioglu (2016). “3D Image Reconstruction from Compton camera data”. In: arXiv: 1604.03805 [physics.data-an] (cit. on p. 61).

**Ley, J.-L.** (2015). “Mise en oeuvre d'un démonstrateur de caméra Compton pour l'imagerie en médecine nucléaire et pour le contrôle en temps réel de la thérapie par hadronthérapie à l'aide des rayonnements gamma prompts.” PhD thesis. École Doctorale de Physique et d'Astrophysique de Lyon (cit. on pp. 11, 12).

**Lojacono, X.**, M.-H. Richard, J.-L. Ley, É. Testa, C. Ray, N. Freud, J. M. Létang, D. Dauvergne, V. Maxim, and R. Prost (2013). “Low Statistics Reconstruction of the Compton Camera Point Spread Function in 3D Prompt-gamma Imaging of Ion Beam Therapy”. In: *IEEE Transactions on Nuclear Science* 60.5, pp. 3355–3363. ISSN: 0018-9499. DOI: <10.1109/TNS.2013.2275200> (cit. on p. 48).

**NationalInstruments** (2010). *PXI Express - NI PXIe-1082 User Manual*. 372752B-01. National Instruments (cit. on p. 24).

**Newport** (2017). *XPS-Q8 Universal High-Performance Motion Controller/Driver*. v.1.4.x. Newport Corporation (cit. on p. 20).

- Nurdan, T. C., K. Nurdan, A. B. Brill, and A. H. Walenta (2015). “Design criteria for a high energy Compton Camera and possible application to targeted cancer therapy”. In: *Journal of Instrumentation* 10.07, p. C07018. URL: <http://stacks.iop.org/1748-0221/10/i=07/a=C07018> (cit. on p. 45).
- Ortega, P. G., I. Torres-Espallardo, F. Cerutti, A. Ferrari, J. E. Gillam, C. Lacasta, G. Llosa, J. F. Oliver, P. R. Sala, P. Solevi, and M. Rafecas (Mar. 2015). “Noise evaluation of Compton camera imaging for proton therapy”. eng. In: *Phys Med Biol* 60.5, pp. 1845–1863. ISSN: 1361-6560 (Electronic); 0031-9155 (Linking). doi: 10.1088/0031-9155/60/5/1845 (cit. on p. 14).
- Pinto, M., D. Dauvergne, N. Freud, J. Krimmer, J. M. Letang, C. Ray, F. Roellinghoff, and E. Testa (2014). “Design optimisation of a TOF-based collimated camera prototype for online hadrontherapy monitoring”. In: *Physics in Medicine and Biology* 59.24, p. 7653. URL: <http://stacks.iop.org/0031-9155/59/i=24/a=7653> (cit. on p. 12).
- Richard, M.-H. (2012). “Design study of a Compton camera for prompt-gamma imaging during ion beam therapy”. PhD thesis. UniversitÃ© Claude Bernard - Lyon I (cit. on p. 10).
- Rogers, J. G., R. Nutt, M. Andreaco, and C. W. Williams (Aug. 1994). “Testing 144- and 256-crystal BGO block detectors”. In: *IEEE Transactions on Nuclear Science* 41.4, pp. 1423–1429. ISSN: 0018-9499. doi: 10.1109/23.322926 (cit. on p. 27).
- SaintGobain (2017). *Plastic Scintillating Fibers - Product brochure*. Saint Gobain Ceramics & Plastics (cit. on pp. 17, 21).
- Sandjong, S., M. Fontana, and É. Testa (2017). “Compton camera prototype for ion beam therapy monitoring: characterization of the BGO scintillators and simulation of the scintillating fiber beam hodoscope”. Master internship report (cit. on p. 14).
- Singh, M. (1983). “An electronically collimated gamma camera for single photon emission computed tomography. Part I: theoretical considerations and design criteria”. In: *Medical Physics* 10.4, pp. 421–427. ISSN: 2473-4209. doi: 10.1118/1.595313. URL: <http://dx.doi.org/10.1118/1.595313> (cit. on p. 44).
- Sonoda, S., Y. Ichimura, H. Kimura, S. Kabuki, A. Takada, T. Mizmoto, H. Kubo, S. Miyamoto, S. Komura, T. Takemura, T. Sawano, T. Kishimoto, Y. Matsuoka, Y. Mizumura, and T. Tanimori (2015). “Application of Electron Tracking Compton Camera (ETCC) in medical imaging”. In: *2015 IEEE Nuclear Science Symposium and Medical Imaging Conference (NSS/MIC)*, pp. 1–3. doi: 10.1109/NSSMIC.2015.7582015 (cit. on p. 61).
- Takeda, S., T. Takahashi, S. Watanabe, H. Tajima, T. Tanaka, K. Nakazawa, and Y. Fukazawa (Jan. 2008). “Double-sided silicon strip detector for x-ray imaging”. In: (cit. on p. 11).
- Tornai, M. P., G. Germano, and E. J. Hoffman (Aug. 1994). “Positioning and energy response of PET block detectors with different light sharing schemes”. In: *IEEE Transactions on Nuclear Science* 41.4, pp. 1458–1463. ISSN: 0018-9499. doi: 10.1109/23.322931 (cit. on p. 27).

---

Zoglauer, A., R. Andritschke, and F. Schopper (2006). “MEGAlib The Medium Energy Gamma-ray Astronomy Library”. In: *New Astronomy Reviews* 50, pp. 629–632. doi: 10.1016/j.newar.2006.06.049 (cit. on p. 48).



# Index

- Adam, L. E., 13, 95  
Adam, Lars-Eric, 95  
Andreaco, M., 98  
Andritschke, R, 99  
Anger, H O, 44, 95  
AspenAerogels, 12, 95
- Bellemann, M. E., 95  
Bellemann, Matthias E., 95  
Berger, M J, 96  
Bhat, M R, xi, 46, 95  
Biegun, A.K., 97  
Breton, D., 27, 95  
Brill, A B, 98  
Brix, G., 95  
Brix, Gunnar, 13, 95  
Bui, F, 95
- Caponetto, L., 97  
Cecchin, D, 53, 95  
Cerutti, F, 98  
Chen, X., 97  
Chevallier, M., 97  
Clinthorne, N, 96  
Coudurier, V, 24, 95
- Dahoumane, M., 12, 95  
Dauvergne, D, 96–98  
Dauvergne, D., 95, 97  
Dauvergne, Denis, 95, 96  
De Marchi, S, 95  
De Rydt, M., 97  
Delagnes, E., 95  
Dendooven, P, 97  
Deng, S. M., 97  
Deng, Shiming, 20, 95, 96  
Doll, Josef, 95
- Enghardt, W., 97  
Everett, D B, 44, 96
- Ferrari, A, 98  
Fiedler, F, 97  
Fleming, J S, 96  
Fontana, M, 43, 96  
Fontana, M., 98  
Freud, N, 97, 98  
Fukazawa, Yasushi, 98
- Gaglione, R., 23, 96  
GE Healthcare, 44, 49, 96  
GeckoDrive, 24, 96  
Germano, G., 98  
Gillam, J E, 98  
Golnik, C., 27, 96, 97
- Haberkorn, Uwe, 95  
Hamamatsu, 18, 23, 24, 96  
Han, L, 44, 45, 47, 59, 96  
Hattori, K, 97  
Heidel, K., 97  
Hoffman, E. J., 98  
Hubbell, J H, 51, 60, 96  
Hueso-González, F, 14, 27, 97  
Huh, S S, 96
- Ichimura, Y, 98
- Kabuki, S, 61, 97, 98  
Kimura, H, 98  
Kishimoto, T, 98  
Knoll, G. F, 9, 97  
Kohara, R, 97  
Komura, S, 98  
Kormoll, T, 97  
Krimmer, J, 98  
Krimmer, J., 20, 95, 97  
Kubo, A, 97  
Kubo, H, 97, 98  
Kuchment, P, 61, 97  
Kunieda, E, 97
- Létang, J M, 96, 97  
Lacasta, C, 98  
Letang, J M, 98  
Ley, J-L, 96, 97  
Ley, J. L., 95  
Ley, J.-L., 11, 12, 97  
Llosa, G, 98  
Lojacono, X, 48, 97  
Lorenz, Walter, 95  
Lu, Guo-Neng, 95, 96
- Maalmi, J., 95  
Mathez, H., 97  
Mathez, HervÃ©, 95, 96  
Matsuoka, Y, 98  
Maxim, V, 96, 97

- Miuchi, K, 97  
Miyamoto, S, 98  
Mizmoto, T, 98  
Mizumura, Y, 98  
  
Nagayoshi, T, 97  
Nakahara, T, 97  
Nakazawa, Kazuhiro, 98  
NationalInstruments, 24, 97  
Newport, 20, 97  
Nightingale, J M, 96  
Nishimura, H, 97  
Nurdan, K, 98  
Nurdan, T C, 45, 98  
Nutt, R., 98  
  
Oberdorfer, Franz, 95  
Okada, Y, 97  
Oliver, J F, 98  
Orito, R, 97  
Ortega, P G, 14, 98  
Ostertag, H., 95  
Ostertag, Hermann, 95  
  
Pausch, G., 97  
Petzoldt, J., 97  
Pinto, M, 12, 98  
Poggiali, D, 95  
Prost, R, 97  
  
RÄmer, K.E., 97  
Rafecas, M, 98  
Ray, C, 97, 98  
Ray, C., 97  
Reithinger, V, 97  
Riccardin, L, 95  
Richard, M-H, 10, 97, 98  
Roellinghoff, F, 98  
Rogers, J. G., 27, 98  
Rogers, W L, 96  
Rusquart, P, 95  
  
SaintGobain, 17, 21, 98  
Sala, P R, 98  
Sandjong, S., 14, 98  
Sawano, T, 98  
Schopper, F, 99  
Schwengner, R., 97  
Sekiya, H, 97  
Shirahata, T, 97  
Singh, M, 44, 98  
  
Solevi, P, 98  
Sonoda, S, 61, 98  
  
Tajima, Hideyuki, 98  
Takada, A, 97, 98  
Takahashi, Tadayuki, 98  
Takeda, Shinichiro, 11, 98  
Takemura, T, 98  
Tanaka, Takaaki, 98  
Tanimori, T, 97, 98  
Terzioglu, F, 97  
Testa, É, 96–98  
Testa, E, 98  
Testa, E., 95, 97  
Todd, R W, 96  
Tornai, M. P, 27, 98  
Torres-Espallardo, I, 98  
Trojan, H., 95  
Trojan, Herbert, 95  
Turco, P, 95  
  
Ueno, K, 97  
  
Wagner, A., 97  
Walenta, A H, 98  
Watanabe, Shin, 98  
Williams, C. W, 98  
  
Zaers, J., 95  
Zaers, Joachim, 95  
Zoccarato, Y, 95, 97  
Zoccarato, Yannick, 95, 96  
Zoglauer, A, 48, 99

# Acknowledgements